IOWA STATE UNIVERSITY
Digital Repository

2008

Experimental investigation of biomimetic wing configurations for Micro Air Vehicle applications

Jeffery T. Murphy
Iowa State University

Experimental investigation of biomimetic wing configurations for Micro Air Vehicle applications

by

Jeffery T. Murphy

A thesis submitted to the graduate faculty

in partial fulfillment of the requirements for the degree of

MASTER OF SCIENCE

Major: Aerospace Engineering

Program of Study Committee:
Hui Hu, Major Professor
Frederick Haan Jr.
Thomas Rudolphi

Iowa State University

Ames, Iowa

2008

UMI Number: 1454599

INFORMATION TO USERS

The quality of this reproduction is dependent upon the quality of the copy submitted. Broken or indistinct print, colored or poor quality illustrations and photographs, print bleed-through, substandard margins, and improper alignment can adversely affect reproduction.

In the unlikely event that the author did not send a complete manuscript and there are missing pages, these will be noted. Also, if unauthorized copyright material had to be removed, a note will indicate the deletion.

UMI®

Table of Contents

List of Figures

List of Tables

Nomenclature

MAV	Micro Air Vehicle
AOA	Angle of Attack
PIV	Particle Image Velocimetry
c	Airfoil Chord Length
μ_{air}	Viscosity of Air
Re_c	Chord Reynolds number,
N	Total Number of Instantaneous PIV Measurement Frames
V_∞	Freestream Velocity
ω_z	Spanwise Vorticity
TKE	Normalized Turbulent Kinetic Energy
u_i, v_i	Instantaneous Velocity Components in x, and y Directions
U, V	Mean Velocity Components in x, and y Directions
u', v'	Turbulent Velocity Fluctuations
S	Surface Area of an Airfoil/Wing
L	Lift Force
D	Drag Force
C_l, Cl	Coefficient of Lift
C_d, Cd	Coefficient of Drag
L/D	Lift-to-Drag Ratio
θ	Wing flap angle
φ	Wing beat frequency

Acknowledgement

I would like to thank my committee members; Dr. Thomas Rudolphi, Dr. Frederick Haan Jr., and particular my advisor Dr. Hui Hu who has been very patient, understanding and supporting during my studies. I would also like to thank my family for supporting me in all of my years of higher learning. Furthermore, I would like to thank my wife Heather and daughter Karlie for being so understanding while I spent so many hours apart from them and working on this degree; they are my motivation and inspiration for any success I experience and I could not do it without them.

Abstract

The purpose of this study was to verify, explore, and better understand low Reynolds number flows associated with wing configurations/designs for potential Micro Air Vehicle (MAV) applications. Chapter 2 discusses and details the results from an experimental study entailing force measurements and Particle Image Velocimetry (PIV) of an airfoil design inspired from the wing of a dragonfly. The comparison airfoils for this experiment are a flat plate, and the 'envelope' shape formed by the streamlines of the flow passing over the corrugated airfoil. In order to achieve this streamline shape as a boundary, the corrugated airfoil was tightly wrapped with paper. Tests were then conducted in the chord Reynolds number range of 5.8×10^4 to 1.23×10^5; corresponding to the Reynolds number regime for MAVs. The results show that the corrugated airfoil out performs the 'smooth' airfoil and flat plate in low Reynolds number flows. However, as the Reynolds number increases, the performance of the smooth airfoil also increases and the advantage of the corrugation diminishes.

Chapter 3 details a very preliminary study of the phenomena employed by most all natural flyers; flapping wings. Although flapping flight has remained quite elusive through our short 100 year history in aviation, the small scale of MAV's may be able to exploit this natural technique. Results are discussed for the variation of several parameters including changing angle of attack from -5 to 15 degrees, wing beat (flapping) frequency from 3.5 to 10.0 beats per second, and chord Reynolds number from approximately 5.4×10^4, 7.7×10^4 and 9.8×10^4. The results of the study show that the main force generated is in the direction of the x-axis of the body, thus in order to create lift for the vehicle to climb, it is necessary to have a positive angle of attack.

Chapter 1. Introduction to Bio-Mimetic MAV Design

Flight has long consumed some of the brightest minds throughout history. Perhaps one of the most well known of these aviation pioneers was Leonardo da Vinci who designed and built a prototype flying machine in 1496 but was unsuccessful at making it fly. The first recorded attempt at human flight is accredited to Archytas, an ancient Greek from the time period 400 B.C.; however, through many centuries of efforts man would not claim mastery of the skies until 1905 with the advent of the Wright Flyer III [1]. Through the last century, the study of flight has taken on a much more scientific approach. Great study, man power, and even human lives have rapidly made the construction of aircraft and flight common place in today's society. Although this is a considerable feat, a new era in aviation has begun.

In the past century flight vehicles have been primarily manned or man controlled, using human sensors, or sensors controlled by humans to complete the mission of the flight. The next goal in aviation is autonomous flight vehicles; vehicles that can complete missions with as little human guidance as possible and rely solely on their electronic and automated sensors to realize given tasks. Strides towards this goal have already been made as there are currently UAVs (Unmanned Air Vehicles) capable of flying missions; primarily as military surveillance.   However, these vehicles are still of a macro scale – of the same order in size as manned aircraft. To realize the full potential of completely automated air vehicles, the vehicle can be miniaturized to scales at which the vehicles could fly through crowded city streets or even through buildings or building rubble to carry out their missions. The term Micro Air Vehicle (MAV) has been coined to describe these small scale vehicles. A loose definition often given for MAVs is an air vehicle with wingspan 15 cm (~ 6 in.) or less and capable of operating at air speeds below 15 m/s (~ 50 ft/s).

MAVs present many useful and lifesaving applications. Potential applications include surveillance, visual inspections, reconnaissance, targeting, life detection, bio-chemical sensing, and communication links at remote or dangerous locations in both militaristic and civilian settings. On a lighter note, many MAVs/UAVs are being developed as toys. As useful as MAVs could prove, they do not come without their own challenges. The small scale of MAVs demands first and foremost very lightweight and compact components. This requirement can also limit other aspects, such as structural restraints or power consumption of the components (i.e., conventional batteries are too large and bulky for MAV applications).

Furthermore, and more related to the studies in this thesis, the aerodynamic considerations for MAVs are very different than that of conventional macro scale air vehicles. Due to their small size and low flight speeds, the range of chord Reynolds numbers in which MAVs operate is typically from $10^4 \sim 10^5$; whereas conventional aircraft operate in chord Reynolds regimes of $10^6 \sim 10^8$. This substantial shift in Reynolds number drastically changes the flow characteristics and physics. Current designs for airfoils/wings for MAVs have been predominately scaled down versions of macro scale airfoils/wings. Although proven for their own applications, these airfoils forfeit much of their performance in the low Reynolds number regimes associated with MAVs.

An ideology geared for the solution of such a problem is bio-mimetic MAV design. The concept of bio-mimetic design is to use aspects and consequences of natural flyers which are already flying in the MAV design Reynolds regime and apply them to construct new airfoil designs and/or wing configurations for MAVs. The topic of this thesis is to attempt to understand more about the flow characteristics and physics of such novel airfoils/wing

configurations. Namely, an airfoil inspired by the wing of a dragonfly is tested by means of total aerodynamic force measurements and Particle Image Velocimetry (PIV); as well as a flapping wing configuration through total aerodynamic force measurements conducted for a small series of experiments. The results show that these designs may be viable options for MAV applications and hold advantages over scaled down traditional airfoils and wings.

Chapter 2. Study of Bio-Inspired Dragonfly Airfoil

2.1. Background of the Dragonfly Airfoil

Dragonflies, along with many other insects such as locusts and damselflies, use a 'corrugated' shaped airfoil for their wings rather than smooth cambered surfaces. After 150 million years of evolution, it is logical to conclude that this must be due to some benefit from this non-intuitive airfoil design [2-4]. Figure 1 shows the structure of a dragonfly forewing consisting of rigid veins webbed by a flexible membrane material – though despite the membrane, the wings are considered to be essentially rigid.
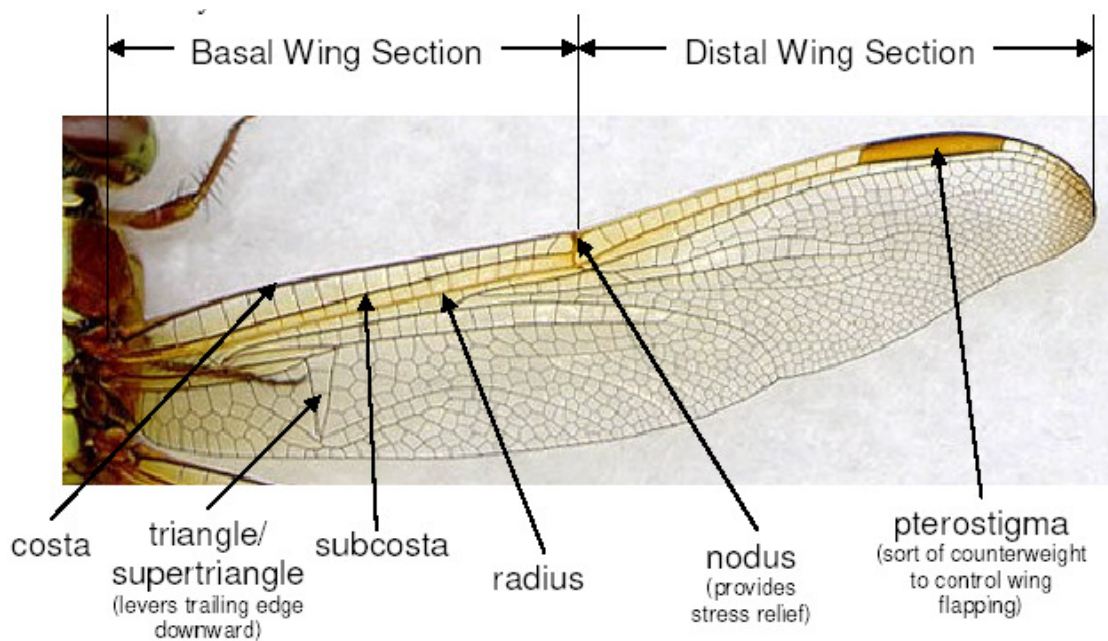
Figure 1. Wing structure of a dragonfly forewing [5].

The typical chord Reynolds number associated with dragonfly flight is less than 5,000 [6]. In this Reynolds regime, boundary layer control and viscous flow considerations become dominant in the flow as opposed to typical manned flight in which such considerations are neglected. It is believed that the corrugation of the wings exploits the

physics of this low Reynolds number flow by acting as a boundary layer trip to transition the laminar flow to a turbulent flow. In doing so, the boundary layer possesses greater energy with which to overcome the adverse pressure gradient over the upper surface of the airfoil and remain attached, in effect delaying stall. Furthermore, the valleys resulting from the corrugation allow for small unsteady vortex structures to form and circulate high-speed fluid to near wall regions promoting boundary layer attachment [7,8]. As a result, the dragonfly wings can produce more lift without the drag penalty associated with traditional airfoil stall at low chord Reynolds number. The advantages to be gained by corrugated airfoils like that of the dragonfly could potentially prove useful in the design of MAV airfoils which also operate in a low Reynolds number flow.

There have been several studies conducted on actual dragonflies and dragonfly inspired airfoils to measure the forces associated with both flapping and steady state gliding configurations. Some of the more notable and recent studies for gliding flight of a dragonfly wing are: a numerical study conducted by Vargas and Mittal [9] of the flow around a 2-D dragonfly airfoil model predicting the small vortex structures in the valleys of the corrugation; a qualitative study of the flow around a dragonfly airfoil by Kwok and Mittal [10] confirming the existence of the vortex structures in a water tunnel; and an experimental study including pressure measurements on the surface and total lift and drag force measurements of a dragonfly airfoil model conducted by Kesel [11]. Additional studies have been listed in the Reference section on page 86. However, these studies have been primarily conducted at $Re_c = 10,000$ or less, which is considerably lower than the range for MAVs. Also, most previous studies conducted have been a biological study of dragonfly wings rather than an analysis of their aerodynamic performance.

More closely related to the current study, Tamai [12] conducted a quantitative study of the flow field around a dragonfly airfoil extracted from the study by Kesel, and compared it with that of a flat plate and low speed GA(W)-1 airfoil at the chord Reynolds number of 34,000 using Particle Image Velocimetry (PIV). The results of the study showed that the corrugated dragonfly airfoil had a higher stall angle than both the flat plate and GA(W)-1 airfoil and was therefore declared to have better aerodynamic performance. Of particular interest, thus motivating this project from the results of the work was the streamlined shape of the flow over the corrugated dragonfly airfoil at lower angles of attack. In order to ensure that the geometry of the corrugation was responsible for the increased performance, it was necessary to investigate the streamlined shape formed by the streamlines of flow. The investigation of the current work was also to determine at what chord Reynolds number the corrugated airfoil no longer held an advantage over the streamlined airfoil shape.

2.2. Experimental Setup for the Dragonfly Airfoil Experiment

The experimental airfoils to be tested were selected from the previous work of Tamai [12]. The flat plate and corrugated dragonfly airfoil descend directly from the study, and the remaining comparison airfoil is again the corrugated dragonfly airfoil however wrapped tautly with paper to produce a smooth surfaced airfoil with identical airfoil characteristics (chord length, maximum thickness, etc…) and corresponding to the streamlines of the flow over the original corrugated dragonfly airfoil. The flat plate has a rectangular cross section with no rounding at the leading and trailing edges and is constructed from balsa with 4.0 mm thickness. The corrugated dragonfly airfoil was extracted from the profile of the mid-section of the forewing of a dragonfly (Aeshna cyanea) as given by Kesel [11] and shown in Figure 2 below. The corrugated dragonfly airfoil was also constructed of balsa with 4.0 mm thickness.
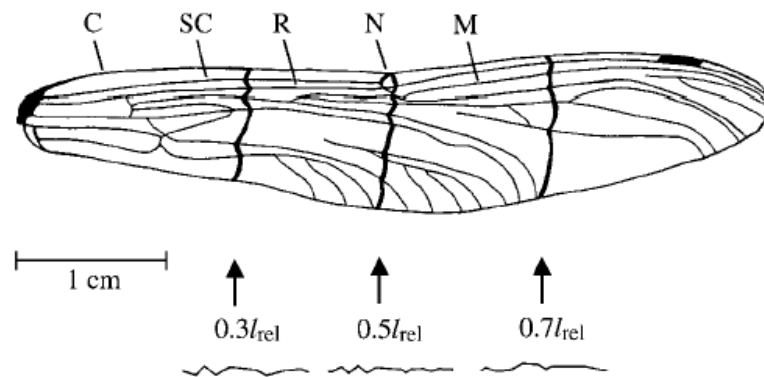
Figure 2. Cross sections of a dragonfly forewing where l_{rel} is the relative span length; the 0.5 l_{rel} cross section was selected for this study [11].

The three test airfoils are considered to have the same nominal chord length of 101 mm and span of 300 mm. Figure 3 shows the cross sections of each airfoil, and Figure 4 details the dimensions of the corrugated dragonfly airfoil used for the study.

a. flat plate

b. wrapped dragonfly airfoil

c. corrugated dragonfly airfoil
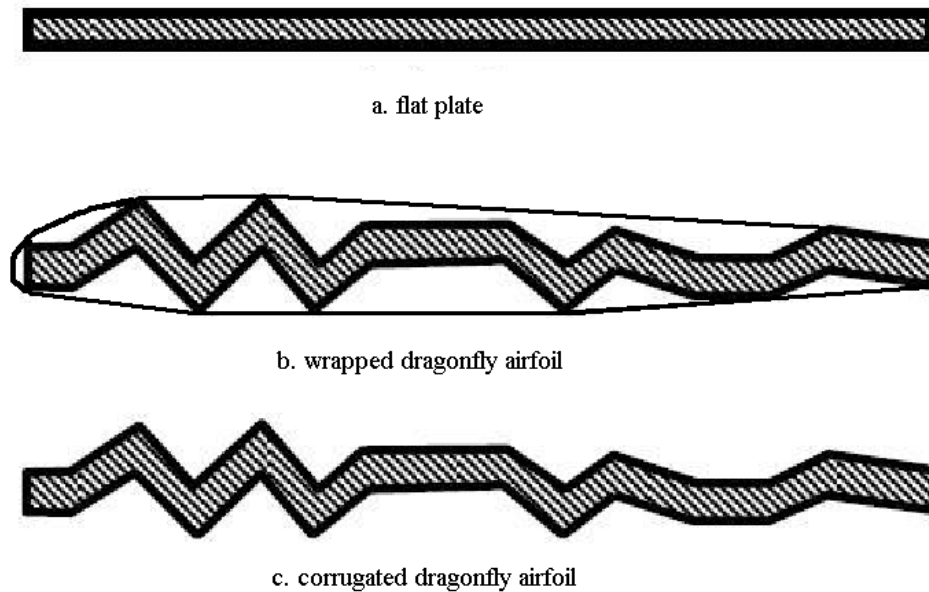
Figure 3. Cross sectional design of the test airfoils.

Dimensions in centimeters
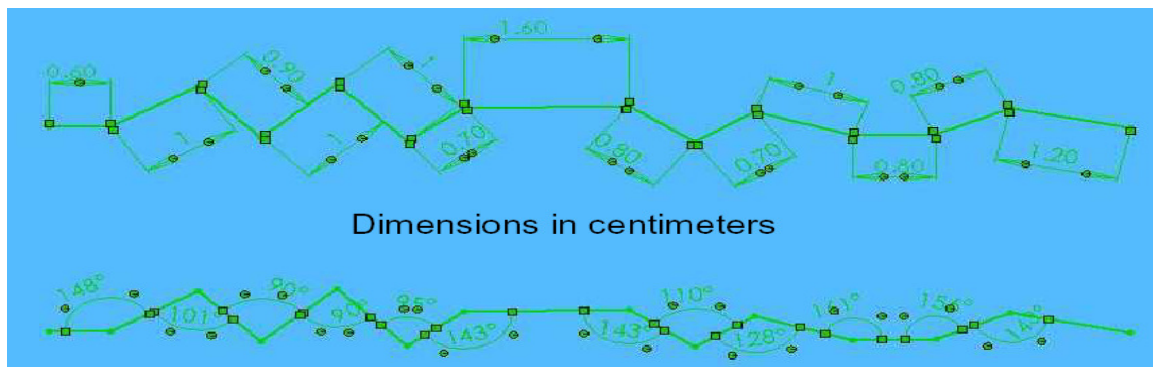
Figure 4. Detailed cross sectional design of corrugated dragonfly airfoil.

The tests were conducted in a low-speed, closed-circuit wind tunnel in the WiST Laboratory of the Aerospace Engineering Department at Iowa State University. The wind tunnel has an optically clear test section with a 30 x 30 cm (1 x 1 ft) cross section; and contains a water cooling system and honeycomb screen structures to produce and maintain a constant temperature, low turbulent flow within the test section. A transverse profile at the center of the test section was measured using a Dantec Dynamics MiniCTA (54T30) in order

to determine the turbulence intensity of the tunnel at 8.3 m/s; Figure 5 shows the results. A single point measurement taken at the center of the test section was also taken for a range of wind tunnel velocities from about 2 ~ 56 m/s. Figure 6 shows the results for the single point measurements. All hotwire measurements were collected at a sampling rate of 500 Hz for 15,000 samples. The results show that the turbulence intensity in the test section for the corresponding tested chord Reynolds numbers was below 1.5%.
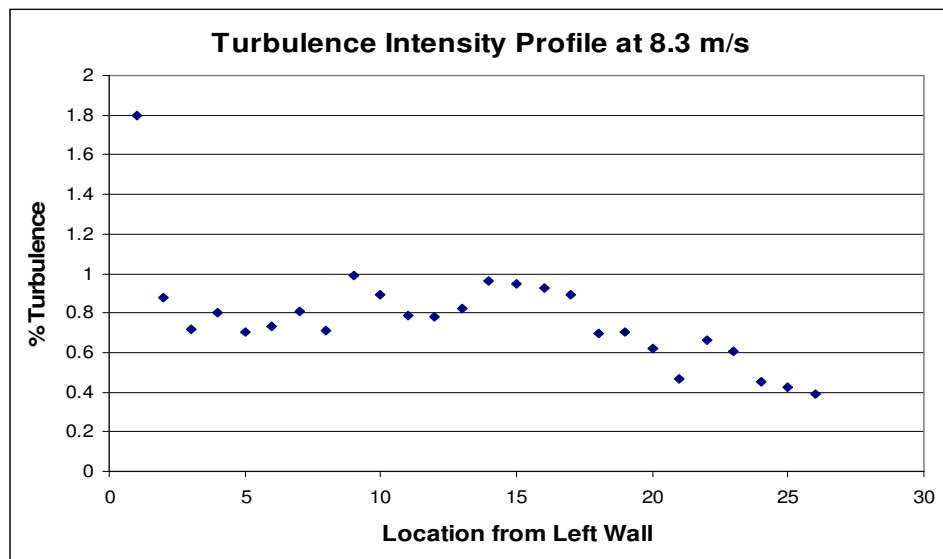
Figure 5. Turbulence intensity horizontal profile of wind tunnel at 8.3 m/s.
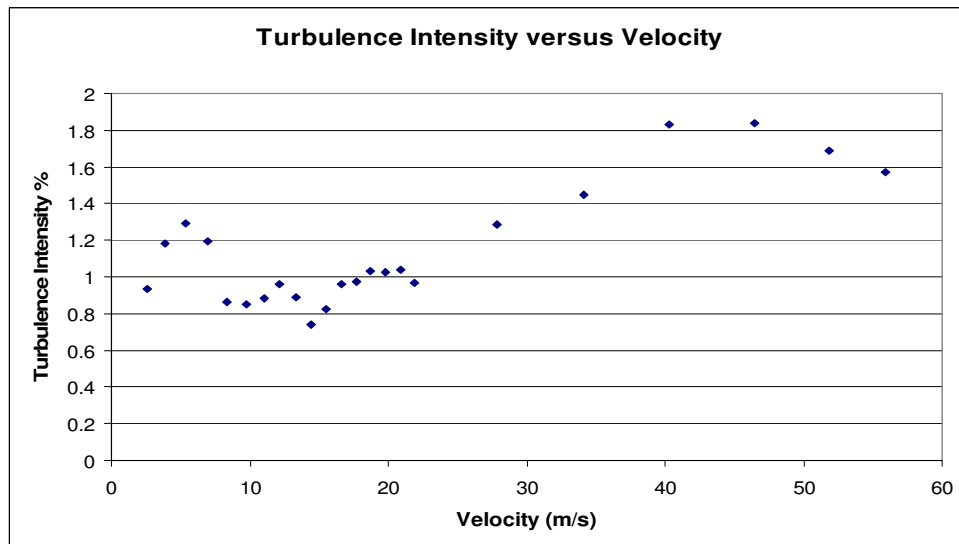
Figure 6. Turbulence intensity of wind tunnel for velocity range 2 ~ 56 m/s.

Total aerodynamic force measurements for the current experiment were taken using a

JR3 Force/Moment Transducer (Model: 30E12A4-I40-EF40N3.1). The sensor is capable of

measuring three orthogonal forces and corresponding moments within 0.25% accuracy (0.1

N) of the limiting capacity of 40 N in the studied orientation. Measurements were taken at a

sampling rate of 1,000 Hz for 15,000 seconds to find the mean total lift and drag forces on

each of the three test airfoils for angle of attack from 0 to 20 degrees in increments of two

degrees. The JR3 system is connected to the host computer DAQ card via a National

Instruments SCB-68 shielded I/O connector block. A diagram of the setup for taking the

force measurements is shown in Figure 7.
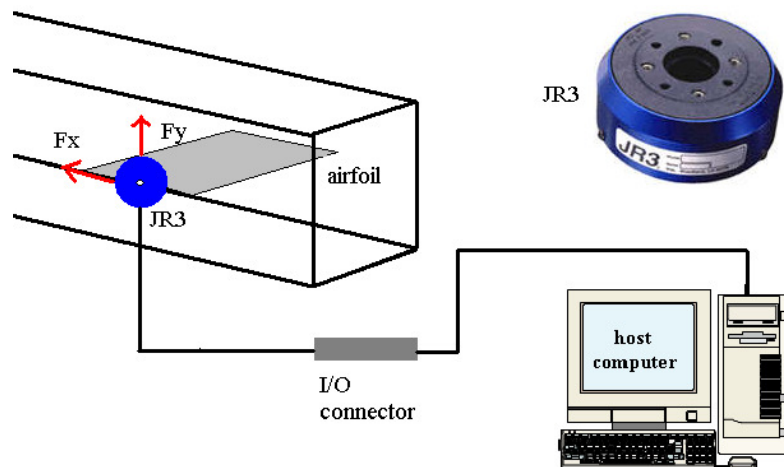
Figure 7. Experimental setup for force measurements using JR3.

A Particle Image Velocimetry (PIV) system was implemented to obtain quantitative

flow field measurements along the chordwise direction at the middle span of each test airfoil.

To perform the experiments, the wind tunnel flow was seeded with   1~5 µm diameter smoke

particles using a Corona Integrated Technologies Inc. Colt 4 smoke generator. A double-

pulsed Nd:Yag laser (NewWave Gemini 200) configured to emit two 200 mJ pulses at a

wavelength of 532 nm was used to illuminate the particles. From the laser head, the laser

was shaped into a thin sheet and reflected up into the test section from below using a convex

and cylindrical lenses and a mirror to reflect the sheet. The sheet thickness reflected at the

mid span of the test airfoil was between 0.5 - 1.0 mm. A 12-bit (1376 x 1040 pixel) CCD

high speed camera (Pixelfly, Cooke Corp) was used to capture the scattering of the particles

and recorded on a host computer using Camware$^{©}$ software. The timing of the system was

controlled using a digital delay generator (Berkley Nucleonics, Model 565). A diagram and

picture of the experimental setup are shown in Figures 8 and 9 respectively.
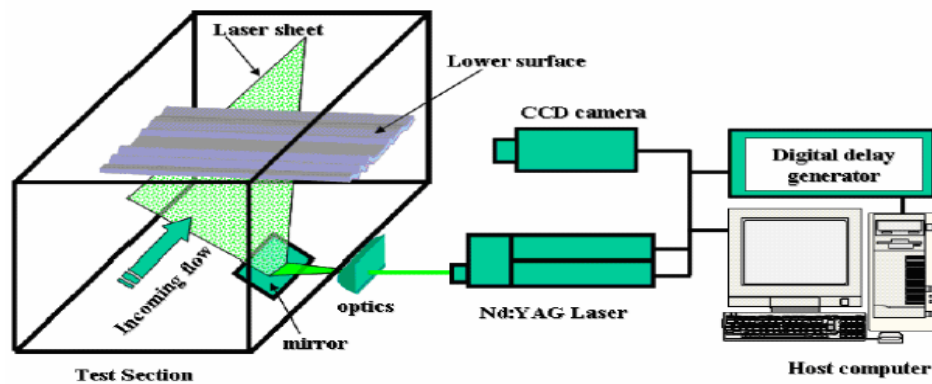
Figure 8. Particle Image Velocimetry setup used to conduct flow field measurements.
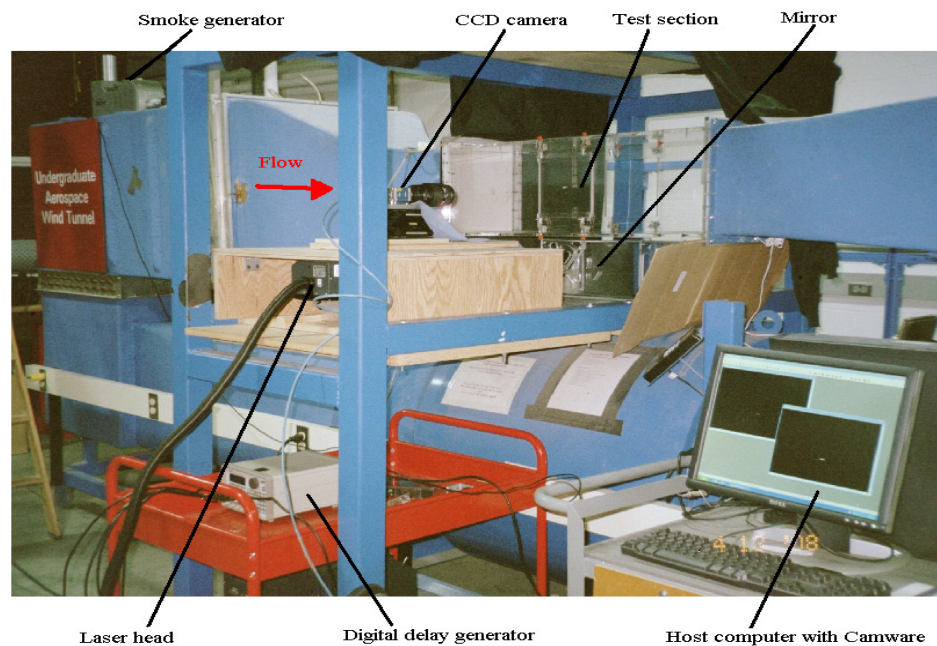
Figure 9. Experimental setup for dragonfly airfoil experiments.

A set of 200 image pairs was taken for each considered case. The image pairs were then used to determine the instantaneous velocity vectors using Insight$^{©}$ with an interrogation window size of 32 x 32 pixels and a 50% overlap to satisfy the Nyquist criterion. A C++ code developed in our lab was then used to process the instantaneous velocity vectors and calculate other flow field quantities such as the instantaneous spanwise vorticity distribution (ω_z), mean and maximum flow velocities in the horizontal and vertical directions (U,V), mean velocity vectors, turbulent velocity fluctuations (*u'*, *v'*), and normalized turbulent kinetic energy distribution (TKE). The measurement uncertainty for the instantaneous velocity vectors is estimated to be about 2.0%; and about 5.0% for the calculated values of the turbulent velocity fluctuations and turbulent kinetic energy. The uncertainty in the calculated instantaneous vorticity is expected to be within 10%. PIV measurements were taken for three different spatial resolutions consisting of measurement window dimensions of approximately 120 mm x 70 mm, 75 mm x 45 mm, and 45 mm x 25 mm in order to resolve structures within the flow field and close to the airfoils surfaces.

2.3. Results and Discussion

2.3.1. Total Aerodynamic Force Measurement

The total aerodynamic force was measured for each of the test airfoils from 0 to 20 degrees angle of attack in increments of two degrees at four chord Reynolds numbers: $Re_c = 58,000$; $Re_c = 80,000$; $Re_c = 102,000$; and $Re_c = 124,000$. This range of Reynolds numbers represents the mid to upper range of the chord Reynolds regime in which MAVs operate. It is noted that MAVs also operate below this range of Reynolds numbers, however, due to the accuracy of the measuring device (JR3) force measurements were only taken in this range. It is also noted that there is existing quantitative flow field data from PIV measurements by Tamai [12] for the dragonfly airfoil and flat plate at a lower chord Reynolds number, $Re_c = 34,000$. Likewise, no measurements were taken above this range of Reynolds numbers to protect the soundness of the models. The mean values for the total lift and drag were found from 15,000 samples acquired at 1,000 Hz by the JR3. Each measurement was taken five times and the results are the average values of these five trials. From these averaged mean force values the coefficients of lift, coefficients of drag and lift-to-drag ratios were calculated.

Figure 10 below shows the lift and drag coefficients for the chord Reynolds number, $Re_c = 58,000$ for the three test airfoils. As seen in the figure, the corrugated dragonfly airfoil outperforms both the wrapped dragonfly airfoil and flat plate by delaying stall until after 12 degrees angle of attack. It is also noted from the figure that the coefficient of drag associated with the corrugated dragonfly airfoil is higher than that for the wrapped airfoil and flat plate; this will play a significant role in the lift-to-drag ratio to be presented and discussed in a later

figure. This increased drag is contrary to other researched studies in which the corrugated

dragonfly airfoil is believed to reduce drag by means of the reversed flow direction in the

valleys of the corrugation canceling some of the skin friction drag around the airfoil.
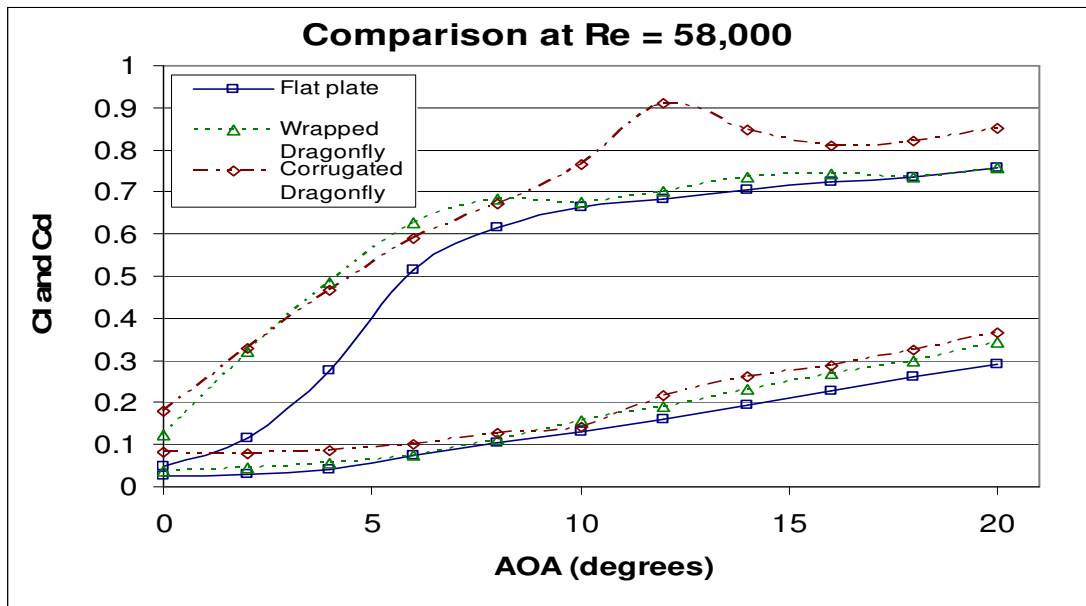
Figure 10. Coefficient of lift and drag for the three test airfoils from
0 to 20 degrees AOA at Re_c = 58,000.

Figures 11, 12, and 13 show the results for the total aerodynamic force coefficients

for the extended chord Reynolds range. Figure 11 shows the coefficient of lift and drag for

the three test airfoils at the chord Reynolds number Re_c = 80,000; followed by Figure 12

which shows the results for Re_c = 102,000; and Figure 13 which shows the results for Re_c =

124,000. It is noted from the results that the performance of the corrugated dragonfly airfoil

does not change significantly, but that the performance of the wrapped dragonfly airfoil

increases considerably and the performance of the flat plate increases marginally with the

increase in chord Reynolds number. This suggests that perhaps the inertial forces in the flow

are beginning to over power the viscous forces that lend the corrugated airfoil its advantages

in the lower Reynolds number regimes.
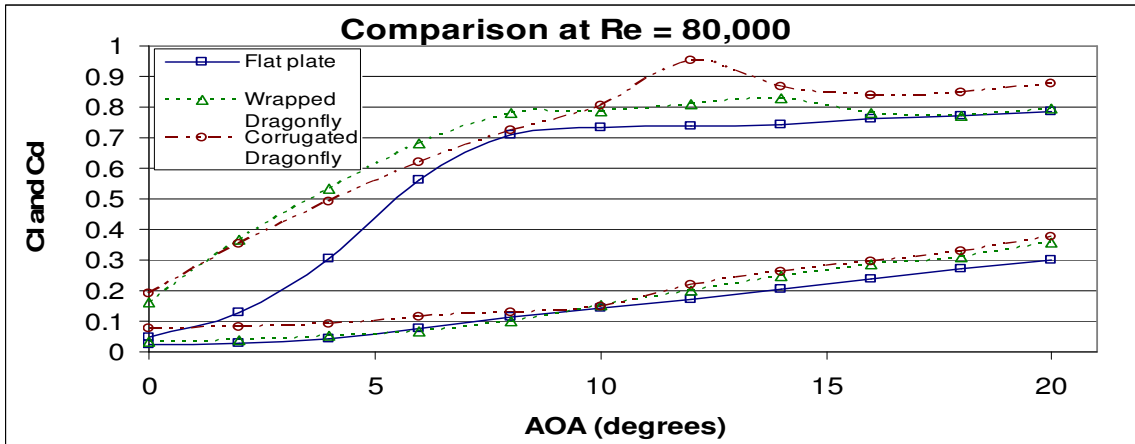
Figure 11. Coefficient of lift and drag for the three test airfoils from
0 to 20 degrees AOA at Re_c = 80,000.
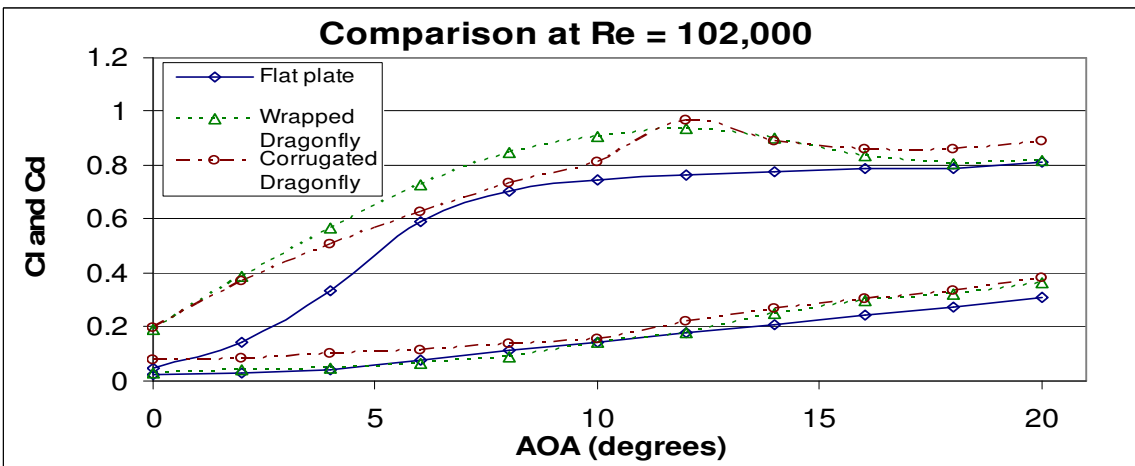
Figure 12. Coefficient of lift and drag for the three test airfoils from
0 to 20 degrees AOA at Re_c = 102,000.
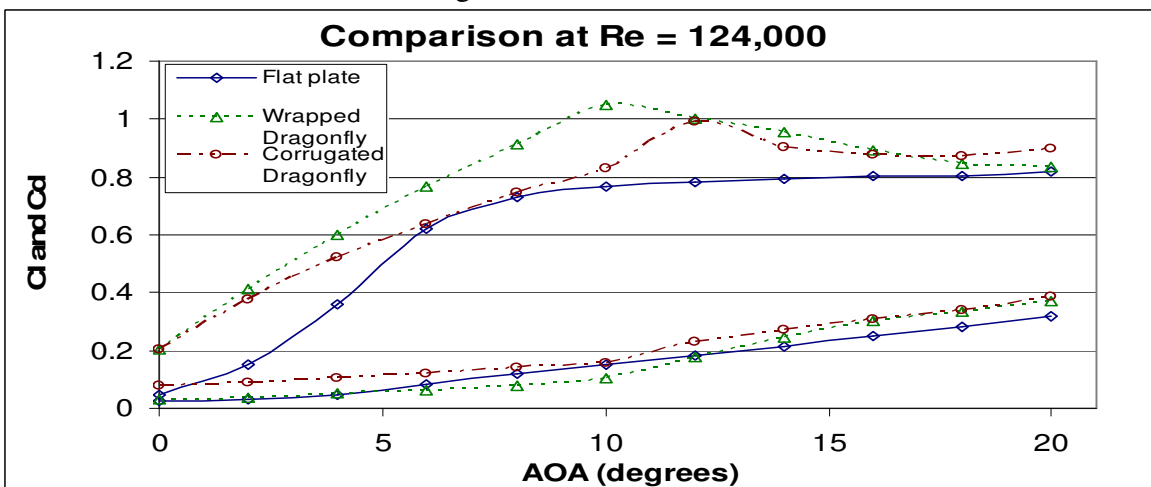
Figure 13. Coefficient of lift and drag for the three test airfoils from
0 to 20 degrees AOA at Re_c = 124,000.

The airfoil performance improvement with increasing chord Reynolds number can be seen more clearly by examining each airfoil individually; the results are presented in this form in Figures 14, 15 and 16 showing the lift and drag coefficients for each airfoil at varying chord Reynolds number. The most dramatic improvement is found in the wrapped dragonfly airfoil. Figure 15 shows that the stall angle of the wrapped dragonfly airfoil is delayed approximately 4 degrees AOA from $Re_c = 58,000$ to $Re_c = 124,000$; thus allowing the maximum coefficient of lift to increase significantly for the higher Reynolds number case. Also due to the delayed stall of the airfoil at $Re_c = 124,000$ there is a significant decrease in the drag coefficient at 10 degrees AOA as well; correlating to greater airfoil efficiency and better performance resulting from the continued flow attachment. The corrugated dragonfly airfoil shows the least response to the increasing Reynolds number of the test airfoils. The plot of the coefficient of drag shows no significant differences for varying Reynolds numbers and the coefficients of lift show only a very modest increase. The flat plate similarly shows little change with increasing chord Reynolds number. It is interesting to note however, that all three test airfoils exhibit the most change in the Reynolds increase from $Re_c = 58,000$ to $Re_c = 80,0000$. This may be attributed to a change in the flow physics in response to the increasing inertial effects overshadowing the viscous aspects of the flow. The repercussion of this would suggest that the corrugated dragonfly airfoil is most advantageous in flows in which the chord Reynolds number is below $Re_c = 80,0000$.
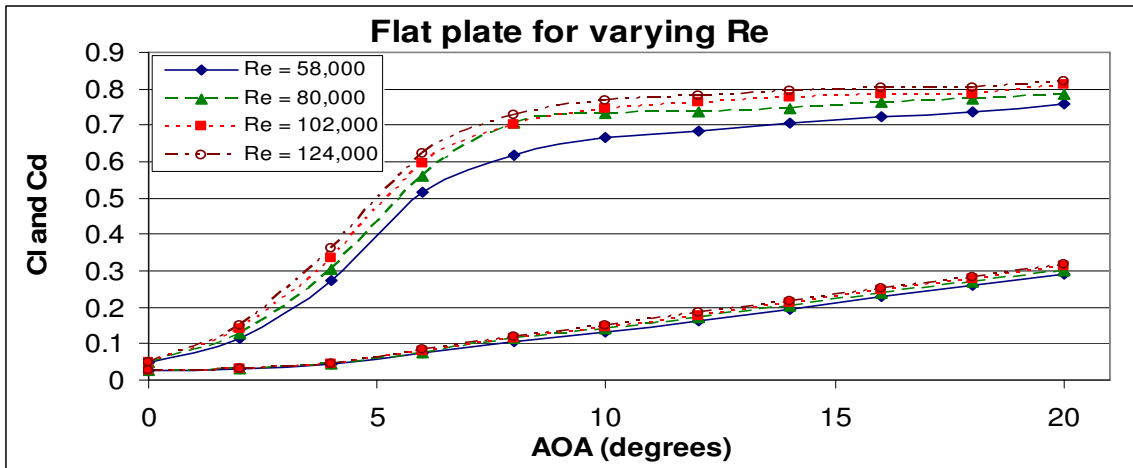
Figure 14. C_l and C_d versus angle of attack for the flat plate with varying Re_c.
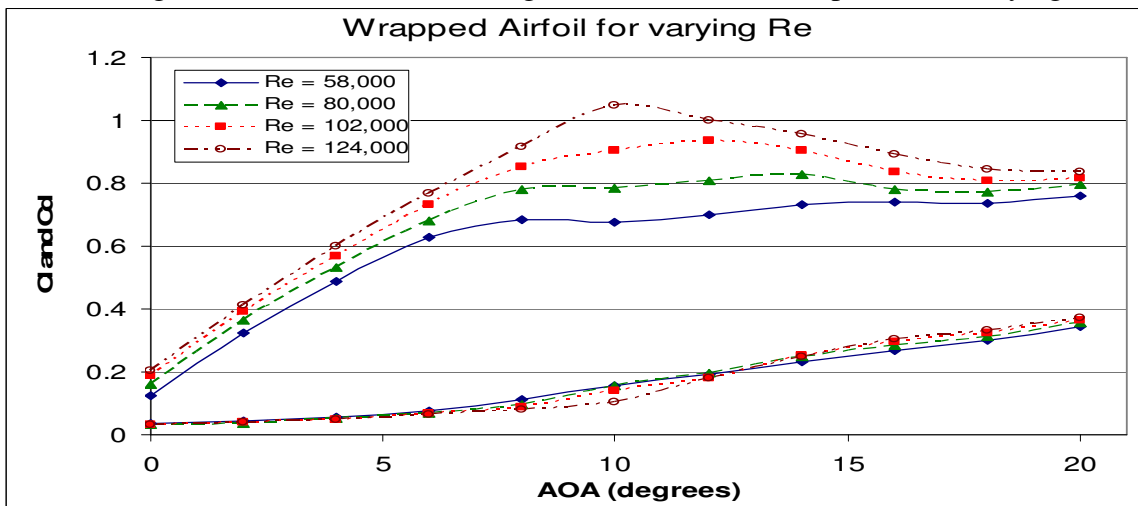
Figure 15. C_l and C_d versus angle of attack for the wrapped dragonfly airfoil with varying Re_c.
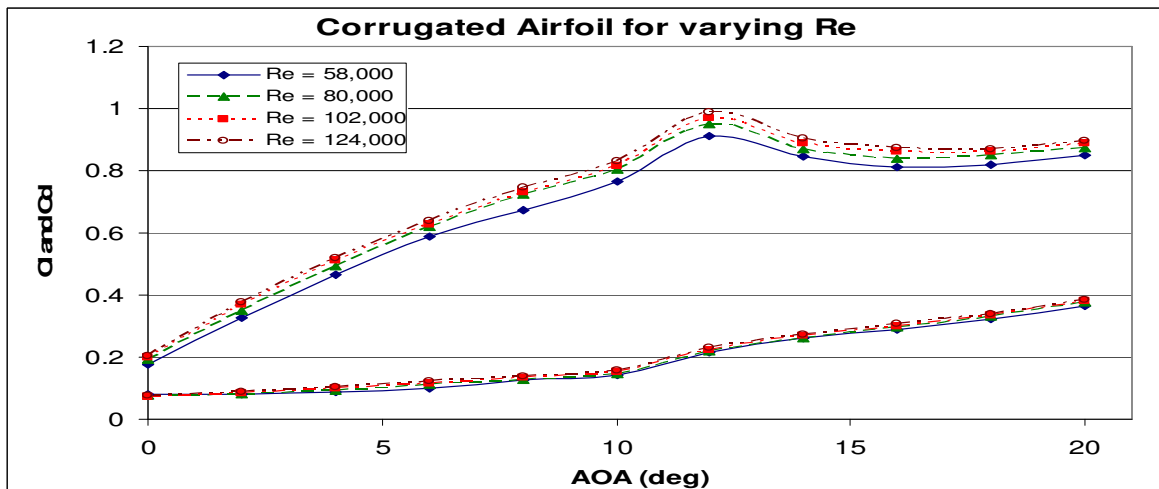
Figure 16. C_l and C_d versus angle of attack for the corrugated dragonfly airfoil with varying Re_c.

A more direct measure often used to compare the efficiency of given airfoils is the lift-to-drag ratio. Again the airfoils can be compared in two ways, against one another at a specified chord Reynolds number, shown in Figures 17, 18, 19, and 20 corresponding to Re_c = 58,000, Re_c = 80,0000, Re_c = 102,000 and Re_c = 124,000 respectively; or each airfoil compared with itself for varying chord Reynolds number, shown in Figures 21, 22, and 23 for the flat plate, wrapped dragonfly airfoil and the corrugated dragonfly airfoil respectively. The results shown in these plots provide insight into the consequence of the higher drag for the corrugated dragonfly airfoil at low angles of attack and support that the there appears to be little advantage of the corrugated dragonfly airfoil over the chord Reynolds number Re_c = 80,0000. The lift-to-drag ratio results do little to promote the corrugated dragonfly airfoil for the tested chord Reynolds numbers; however it is the application for which the airfoil is intended that the corrugated dragonfly airfoil gains its usefulness.
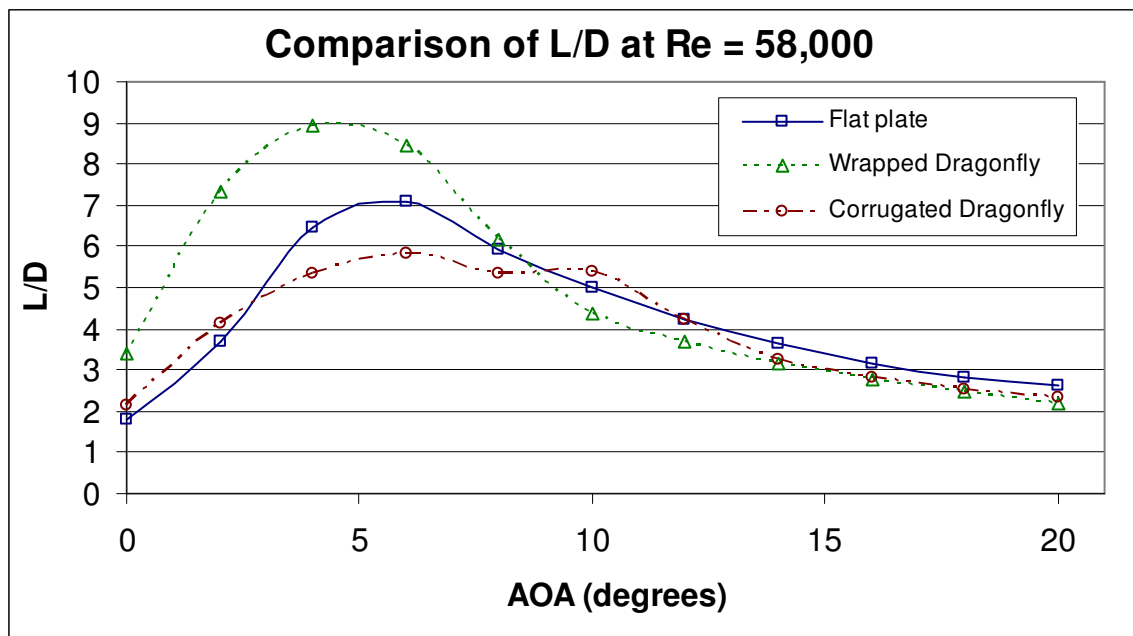
Figure 17. Lift-to-drag ratio versus angle of attack for test airfoils at Re_c = 58,000.
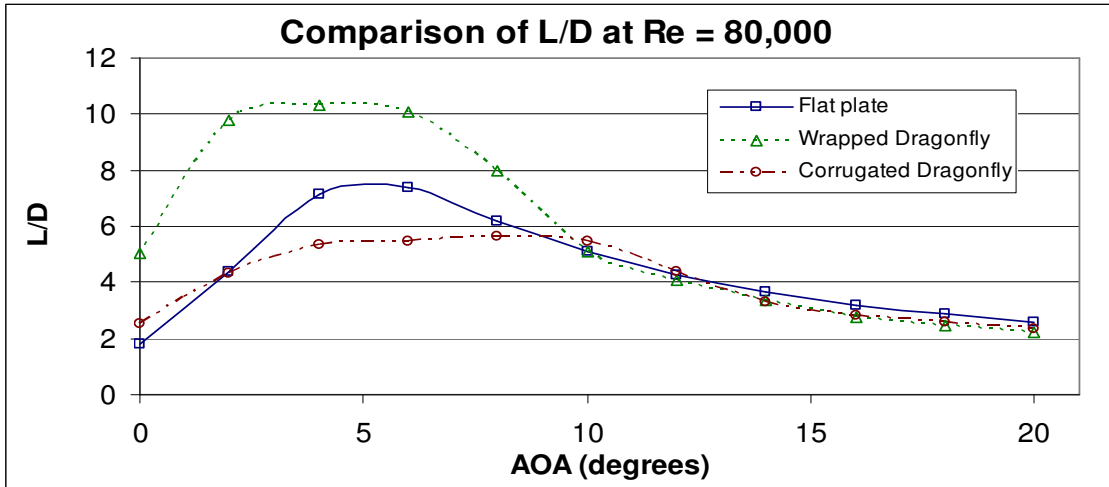
Figure 18. Lift-to-drag ratio versus angle of attack for test airfoils at $Re_c = 80,000$.
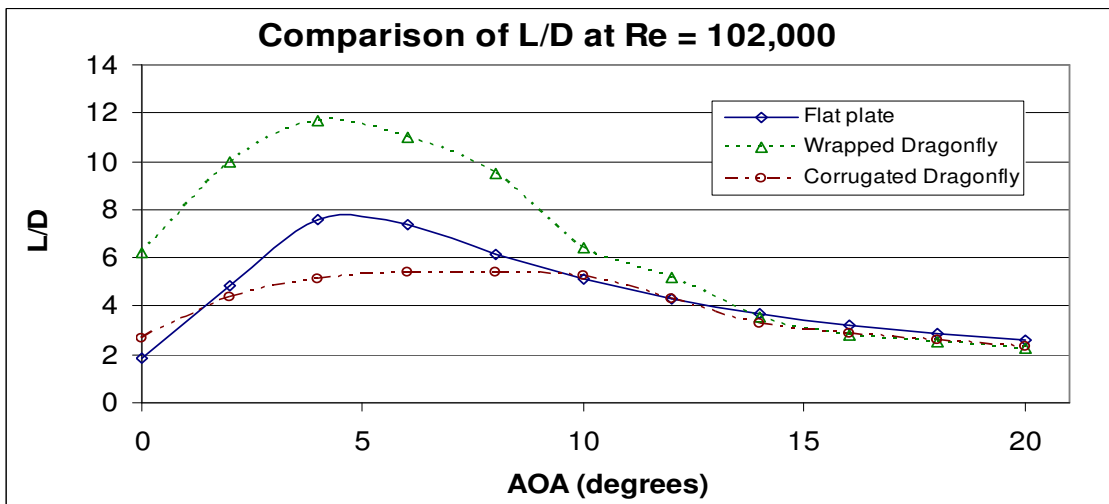
Figure 19. Lift-to-drag ratio versus angle of attack for test airfoils at $Re_c = 102,000$.
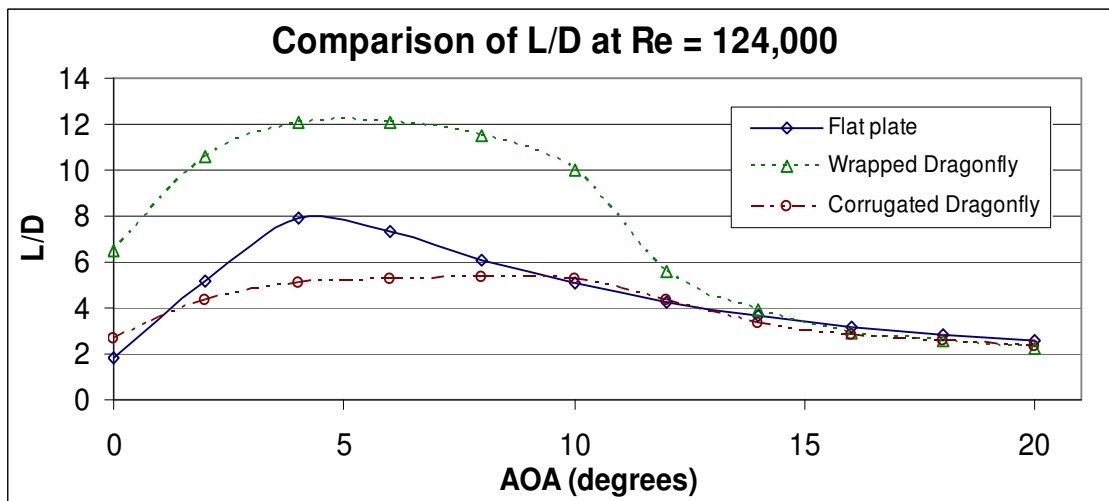
Figure 20. Lift-to-drag ratio versus angle of attack for test airfoils at $Re_c = 124,000$.
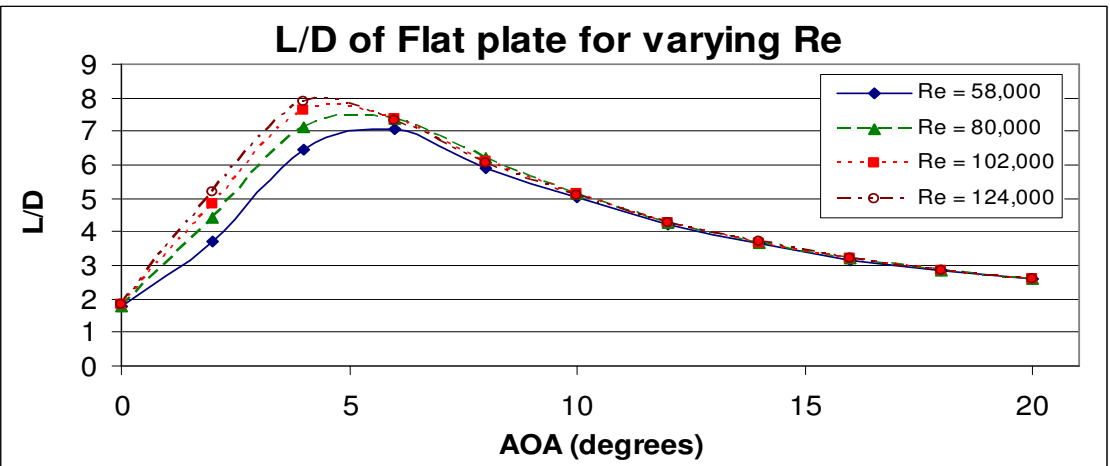
Figure 21. Lift-to-drag ratio versus angle of attack for the flat plate for varying Re_c.
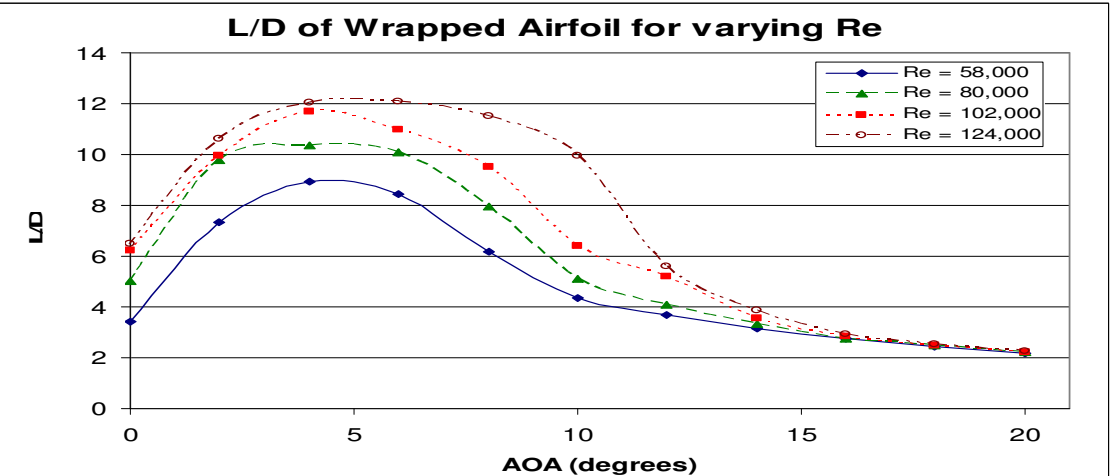
Figure 22. Lift-to-drag ratio versus angle of attack for the wrapped dragonfly airfoil for varying Re_c.
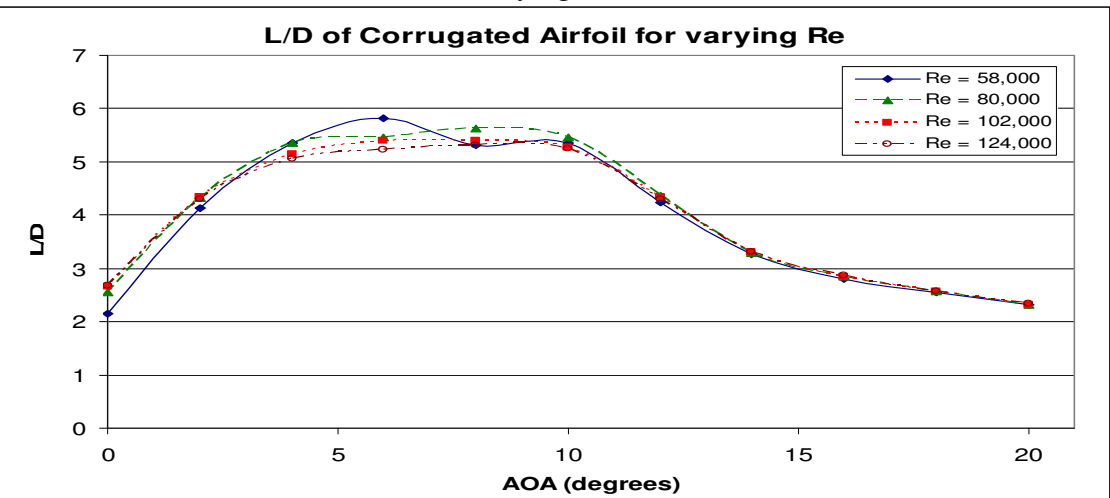
Figure 23. Lift-to-drag ratio versus angle of attack for the corrugated dragonfly airfoil for varying Re_c.

The results shown in the lift-to-drag ratio plots for the test airfoils show a similar result to that of the chord Reynolds effect on the lift and drag coefficients. The lift-to-drag ratio of the wrapped dragonfly airfoil increases significantly as the Reynolds number increases. The flat plate shows a modest increase in the lowers angle of attack, and the corrugated dragonfly airfoil shows little reflection of change in Reynolds number.

Despite the poor lift-to-drag ratio displayed by the corrugated dragonfly airfoil at the test chord Reynolds numbers, the inspection of the actual forces for the test airfoils at the chord Reynolds number $Re_c = 58,000$ indicates the importance of the corrugation. Figure 24 shows the lift and drag forces measured in Newtons for the three test airfoils below. From the plot it is apparent that the maximum lifting force generated by the corrugated airfoil due to the delayed stall angle is approximately 30% higher than that for the wrapped dragonfly airfoil and flat plate. Although the increased drag may require more power, the increased lift at this low airspeed can allow the vehicle to loiter, which could prove essential in many MAV applications. The ability to remain aloft at lower airspeeds could potentially supersede the need for aerodynamic efficiency.
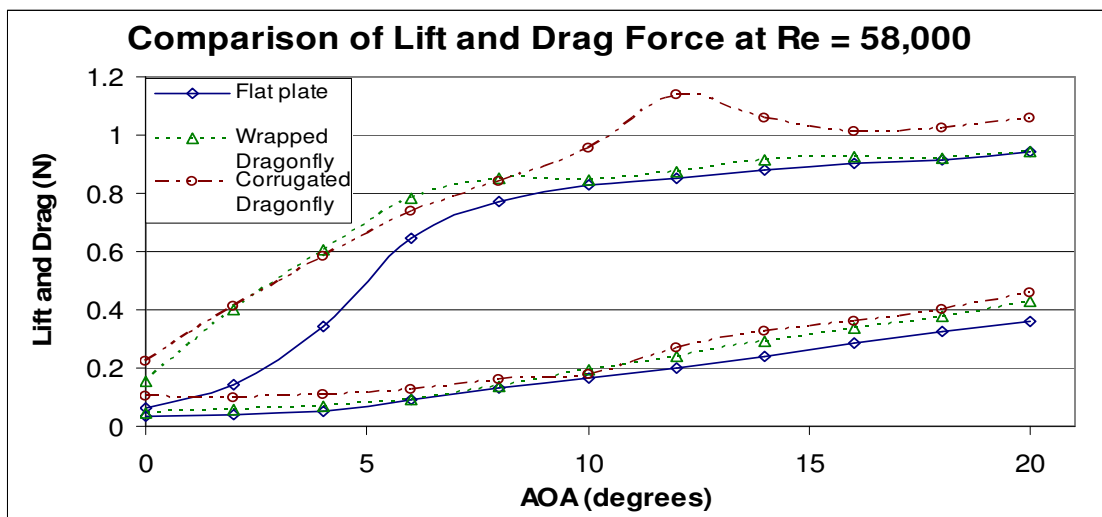
Figure 24. Lift and drag forces measured for the three test airfoils at $Re_c = 58,000$.

2.3.2 PIV Measurement

The results of the quantitative PIV flow measurements are presented in the following pages. The results of the entire flow field (120 mm x 70 mm measurement window) around the airfoil are presented first and will be discussed in greater detail at the conclusion of the full view figures. The full view results are contained within Figure 25-57. Figures 25-54 compare the instantaneous velocity vectors and vorticity along with the ensemble-averaged streamlines around each of the test airfoils from 2 to 20 degrees angle of attack in two degree increments. Figures 55-57 present the ensemble-averaged velocity vectors around each of the airfoils from 2 to 20 degrees angle of attack in two degree increments. Results are then presented for the 45 mm x 25 mm measurement window detailing the flow at the leading edge for each of the test airfoils in Figures 58-66. Figures 58-60 present the instantaneous velocity and vorticity, ensemble-averaged streamlines, and normalized turbulent kinetic energy for the flat plate from 6 to 14 degrees angle of attack in two degree increments. Figures 61-63 likewise present the results for the wrapped dragonfly airfoil; and Figures 64-66 show the results for the corrugated dragonfly airfoil. The results are discussed in detail after the presentation of the figures. Figures 67-72 present the results for the PIV measurements with measurement window size 75 mm x 45 mm showing approximately 75% of the upper surface of the airfoil. Figures 67, 69, and 71 show the instantaneous velocity vectors and vorticity distribution for the flat plate, wrapped dragonfly airfoil, and corrugated dragonfly airfoil respectively from 6 to 14 degrees angle of attack by two degree increments. Figures 68, 70, and 72 show the ensemble-averaged streamlines for the airfoils for the same range of angle of attack.
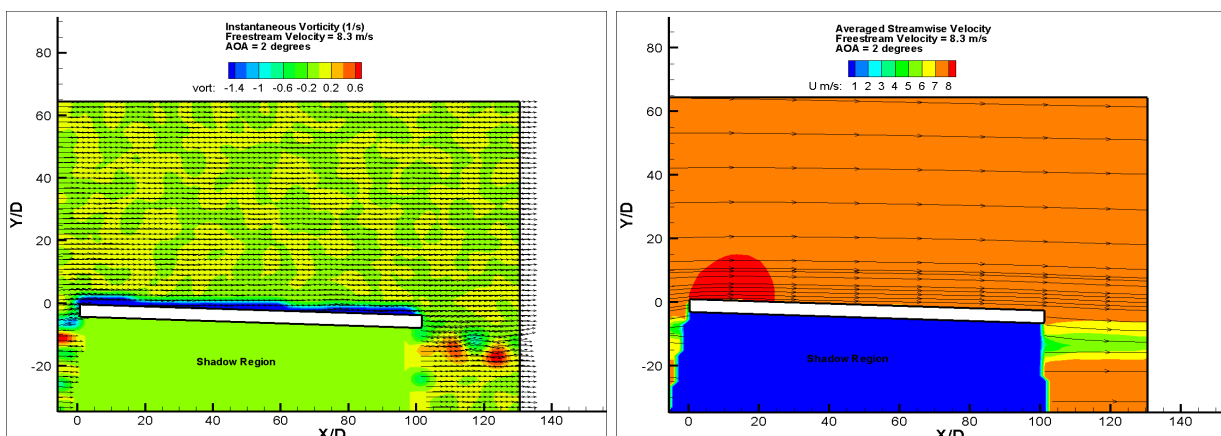
Figure 25. Instantaneous velocity vectors and spanwise vorticity distribution (left) and ensemble-averaged streamlines (right) around the flat plate at AOA = 2 degrees.
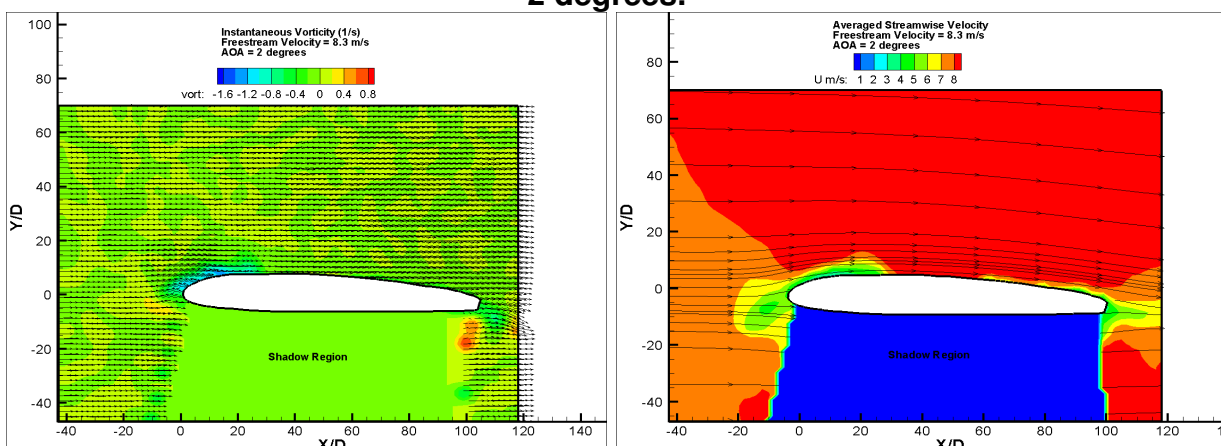
Figure 26. Instantaneous velocity vectors and spanwise vorticity distribution (left) and ensemble-averaged streamlines (right) around the wrapped dragonfly airfoil at AOA = 2 degrees.
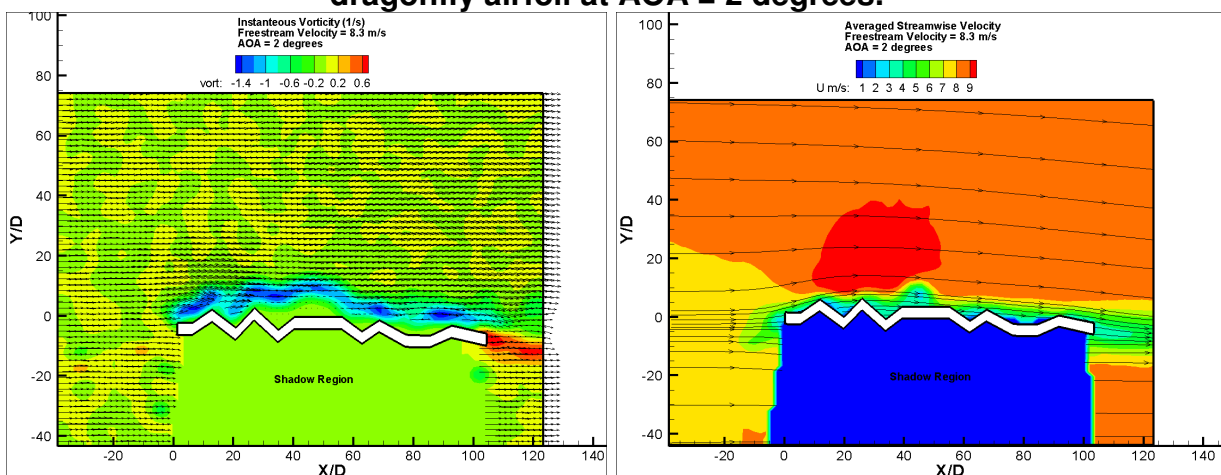
Figure 27. Instantaneous velocity vectors and spanwise vorticity distribution (left) and ensemble-averaged streamlines (right) around the dragonfly airfoil at AOA = 2 degrees.
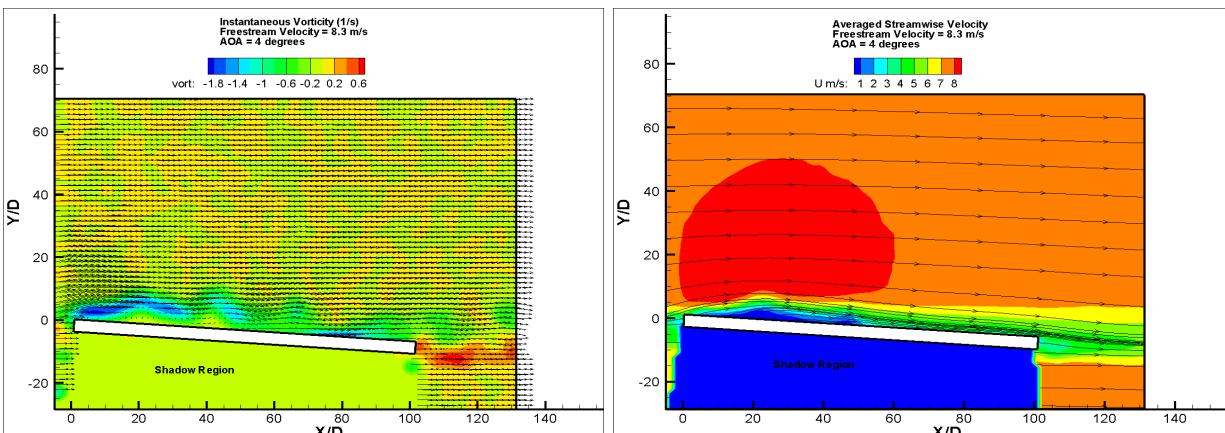
Figure 28. Instantaneous velocity vectors and spanwise vorticity distribution (left) and ensemble-averaged streamlines (right) around the flat plate at AOA = 4 degrees.
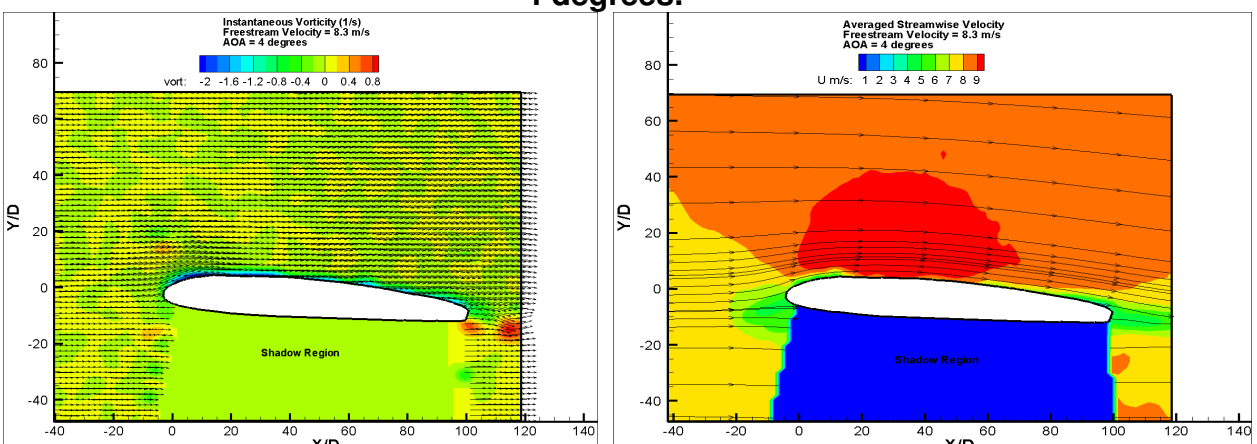
Figure 29. Instantaneous velocity vectors and spanwise vorticity distribution (left) and ensemble-averaged streamlines (right) around the wrapped dragonfly airfoil at AOA = 4 degrees.
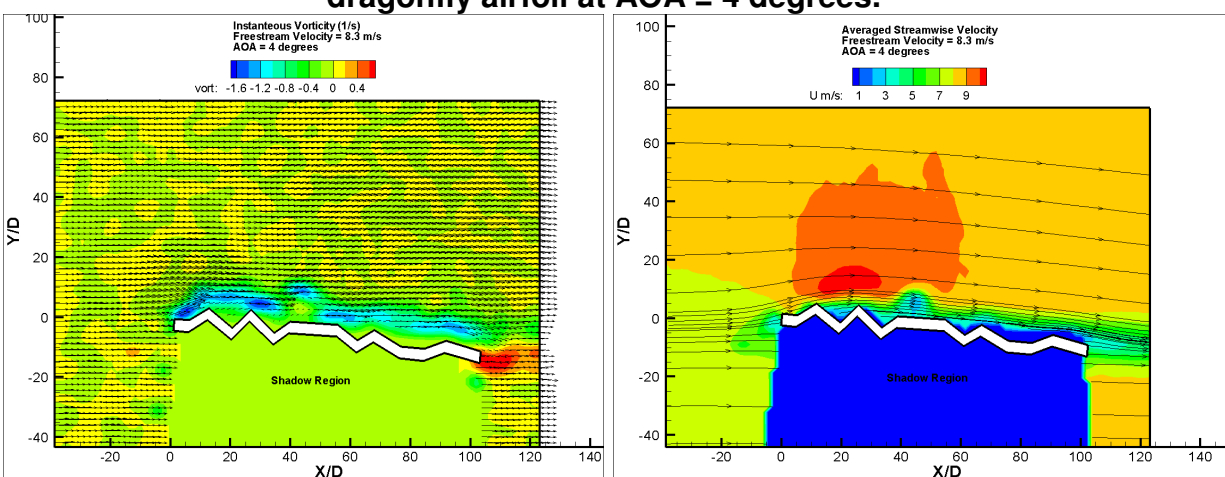
Figure 30. Instantaneous velocity vectors and spanwise vorticity distribution (left) and ensemble-averaged streamlines (right) around the dragonfly airfoil at AOA = 4 degrees.
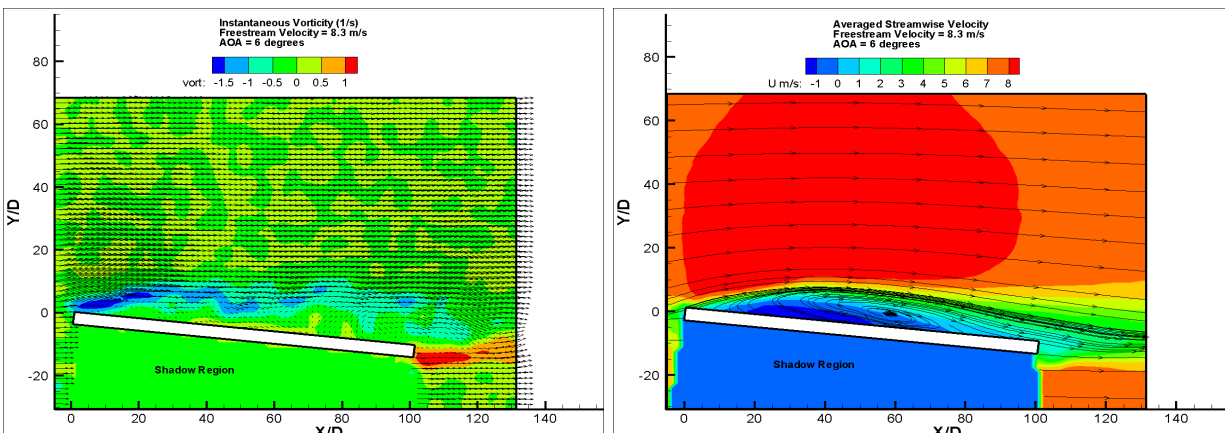
Figure 31. Instantaneous velocity vectors and spanwise vorticity distribution (left) and ensemble-averaged streamlines (right) around the flat plate at AOA = 6 degrees.
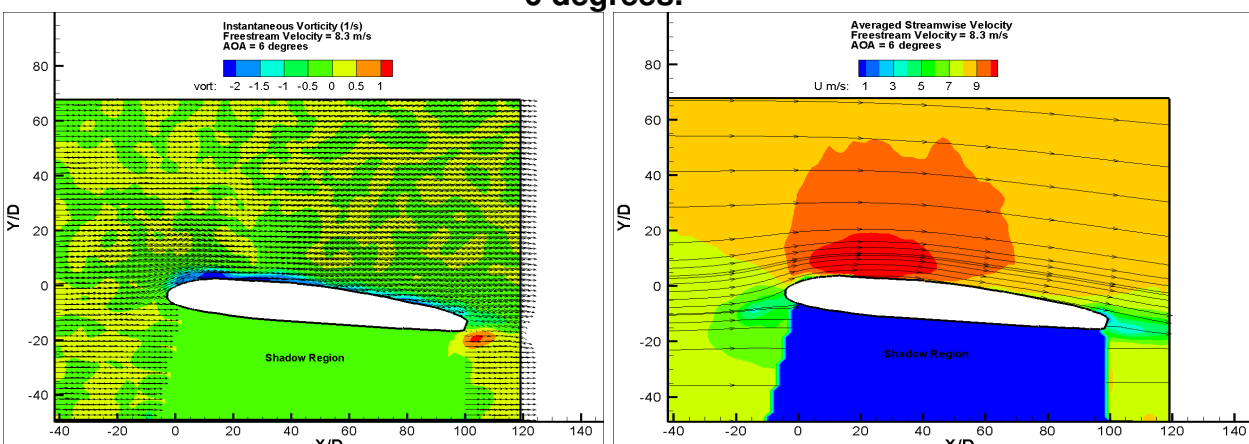
Figure 32. Instantaneous velocity vectors and spanwise vorticity distribution (left) and ensemble-averaged streamlines (right) around the wrapped dragonfly airfoil at AOA = 6 degrees.
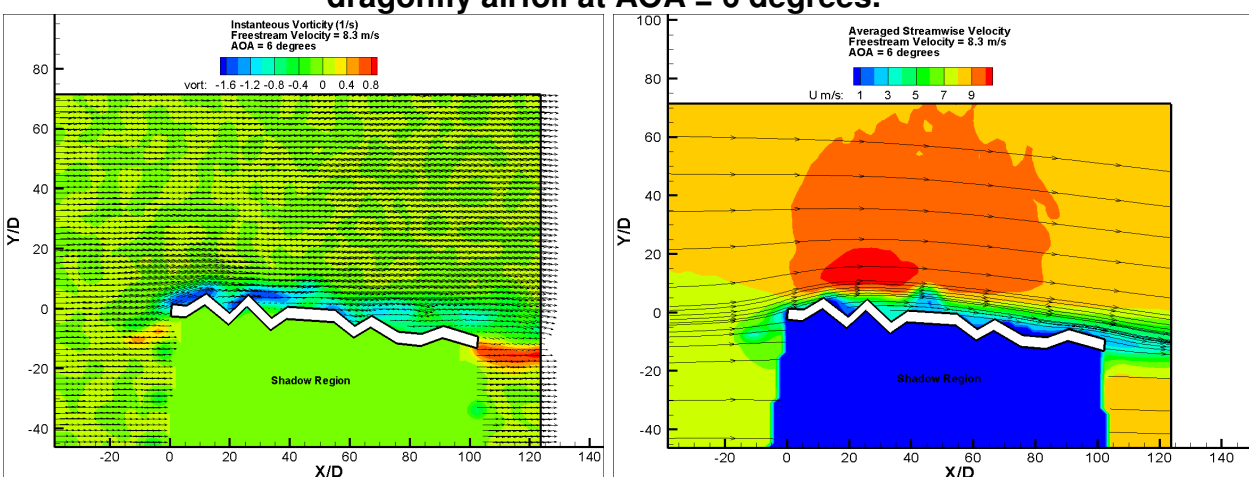
Figure 33. Instantaneous velocity vectors and spanwise vorticity distribution (left) and ensemble-averaged streamlines (right) around the dragonfly airfoil at AOA = 6 degrees.
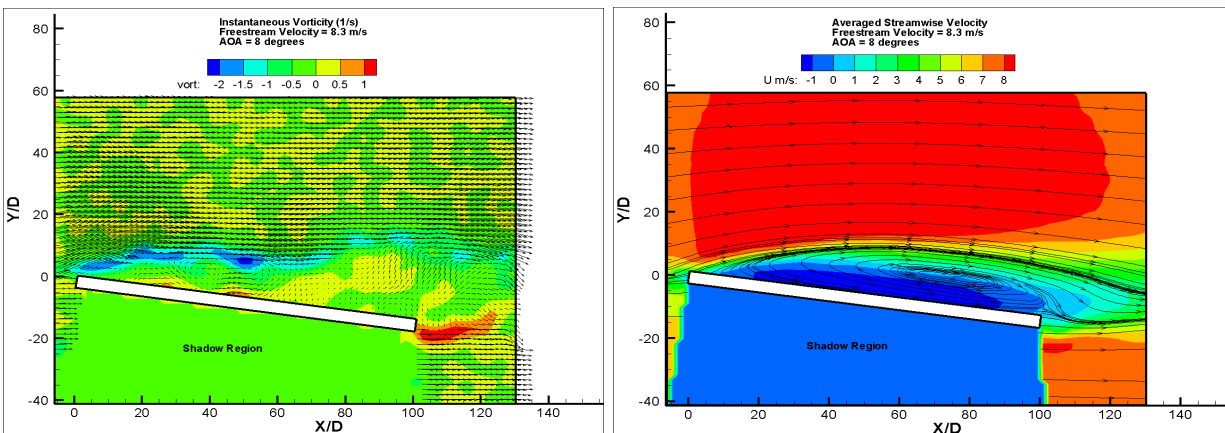
Figure 34. Instantaneous velocity vectors and spanwise vorticity distribution (left) and ensemble-averaged streamlines (right) around the flat plate at AOA = 8 degrees.
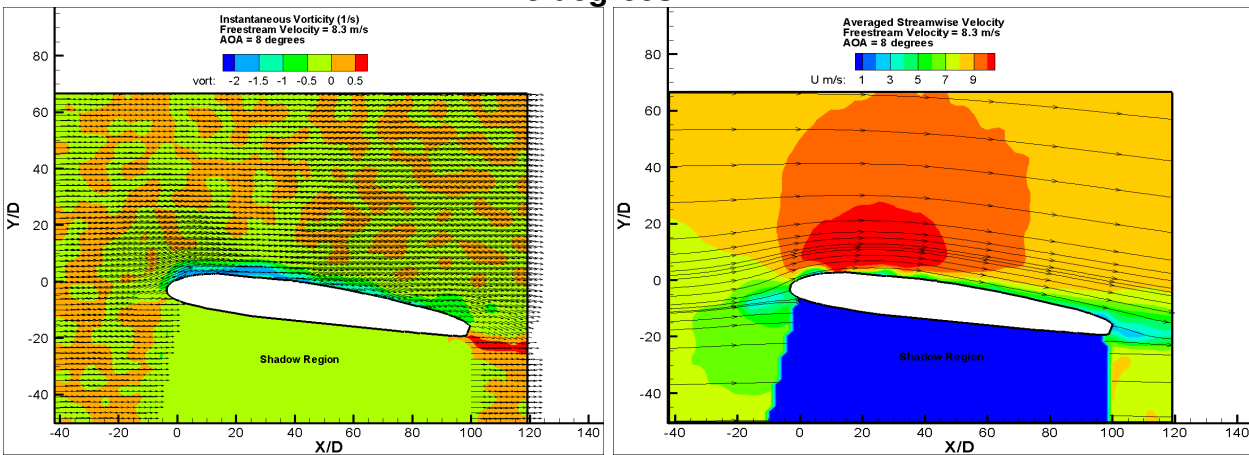
Figure 35. Instantaneous velocity vectors and spanwise vorticity distribution (left) and ensemble-averaged streamlines (right) around the wrapped dragonfly airfoil at AOA = 8 degrees.
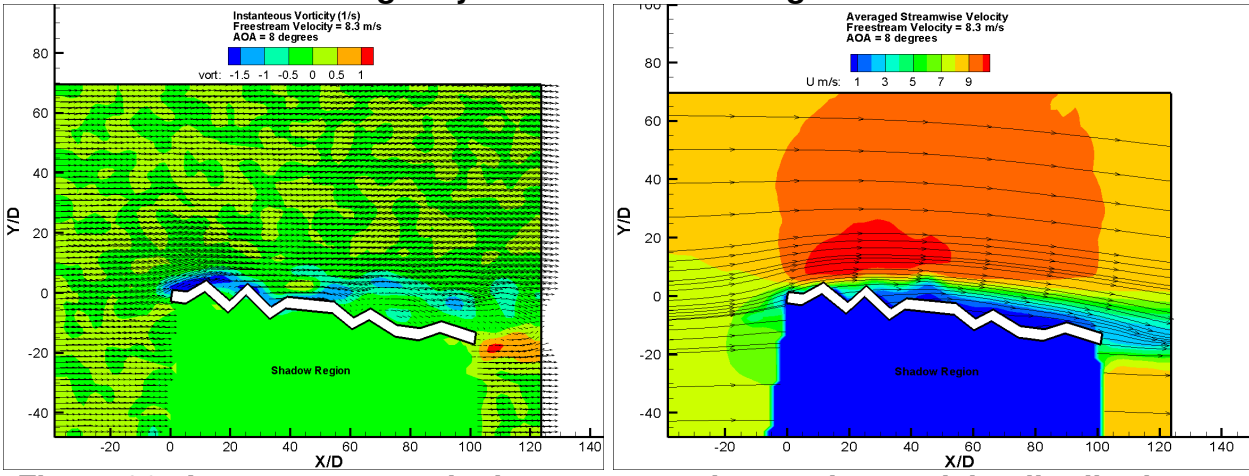
Figure 36. Instantaneous velocity vectors and spanwise vorticity distribution (left) and ensemble-averaged streamlines (right) around the dragonfly airfoil at AOA = 8 degrees.
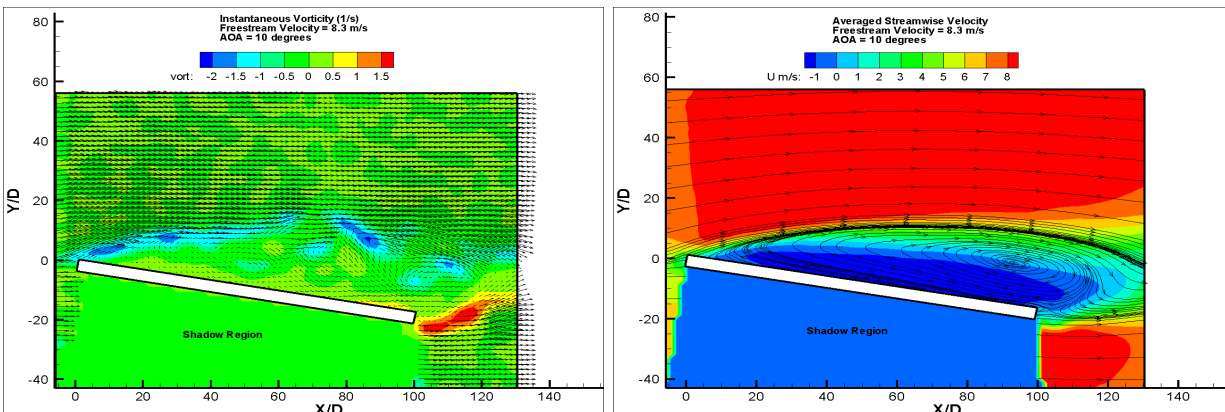
Figure 37. Instantaneous velocity vectors and spanwise vorticity distribution (left) and ensemble-averaged streamlines (right) around the flat plate at AOA = 10 degrees.
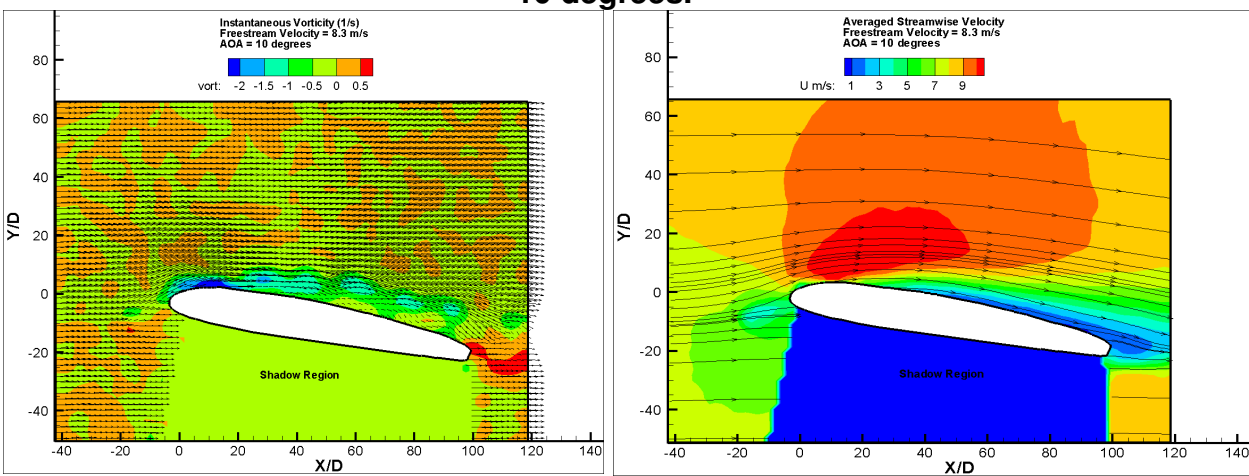
Figure 38. Instantaneous velocity vectors and spanwise vorticity distribution (left) and ensemble-averaged streamlines (right) around the wrapped dragonfly airfoil at AOA = 10 degrees.
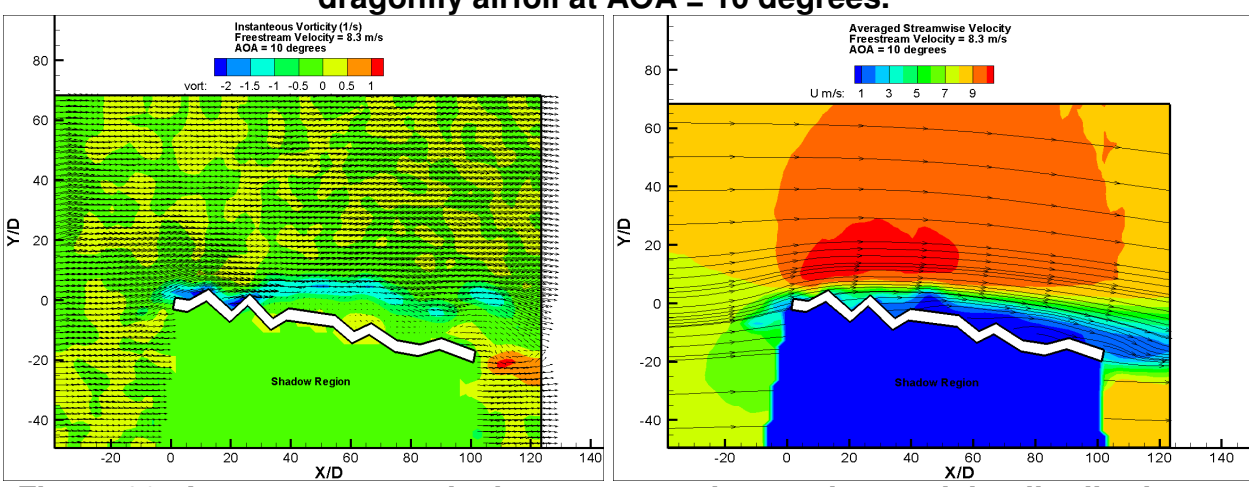
Figure 39. Instantaneous velocity vectors and spanwise vorticity distribution (left) and ensemble-averaged streamlines (right) around the dragonfly airfoil at AOA = 10 degrees.
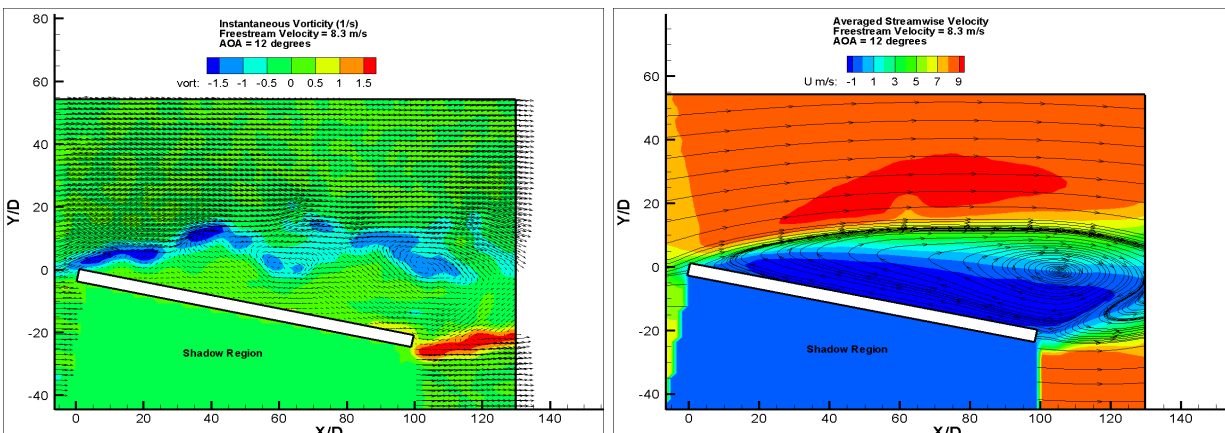
Figure 40. Instantaneous velocity vectors and spanwise vorticity distribution (left) and ensemble-averaged streamlines (right) around the flat plate at AOA = 12 degrees.
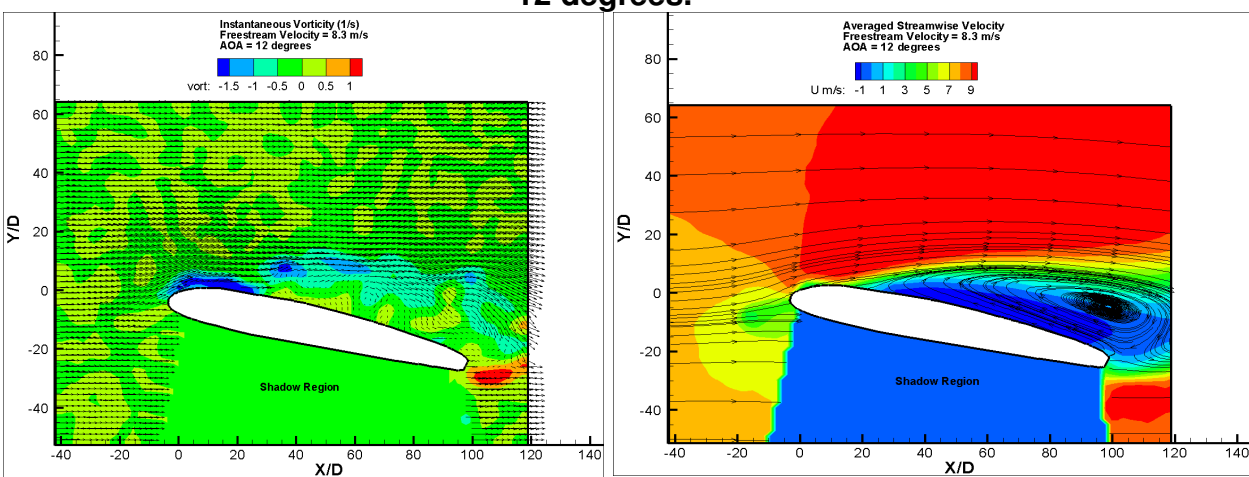
Figure 41. Instantaneous velocity vectors and spanwise vorticity distribution (left) and ensemble-averaged streamlines (right) around the wrapped dragonfly airfoil at AOA = 12 degrees.
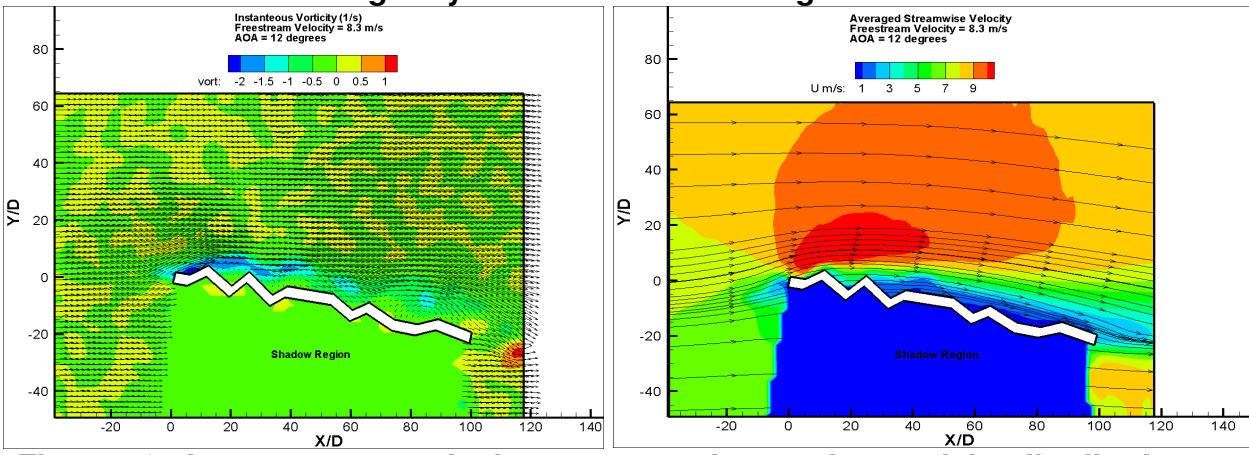
Figure 42. Instantaneous velocity vectors and spanwise vorticity distribution (left) and ensemble-averaged streamlines (right) around the dragonfly airfoil at AOA = 12 degrees.
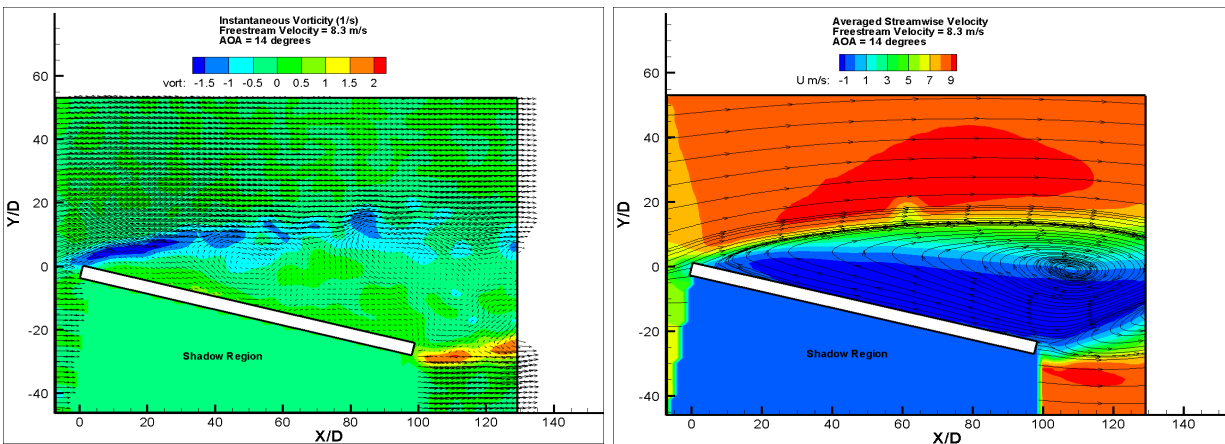
Figure 43. Instantaneous velocity vectors and spanwise vorticity distribution (left) and ensemble-averaged streamlines (right) around the flat plate at AOA = 14 degrees.
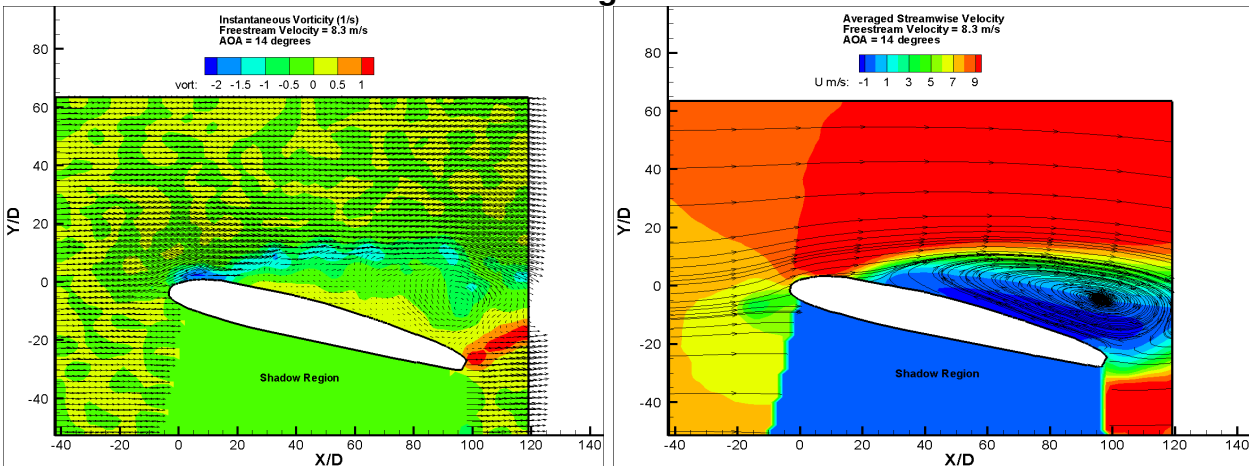
Figure 44. Instantaneous velocity vectors and spanwise vorticity distribution (left) and ensemble-averaged streamlines (right) around the wrapped dragonfly airfoil at AOA = 14 degrees.
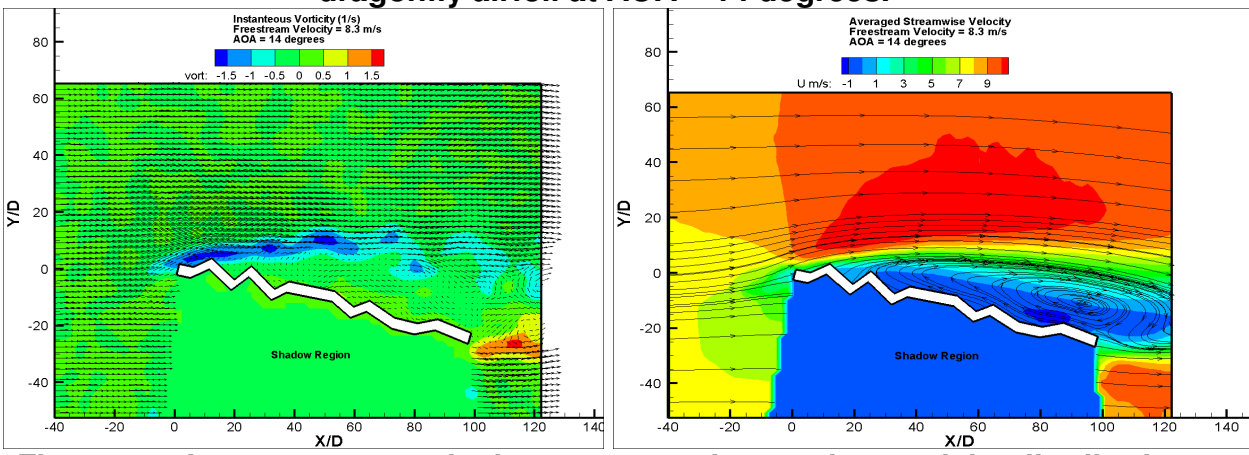
Figure 45. Instantaneous velocity vectors and spanwise vorticity distribution (left) and ensemble-averaged streamlines (right) around the dragonfly airfoil at AOA = 14 degrees.
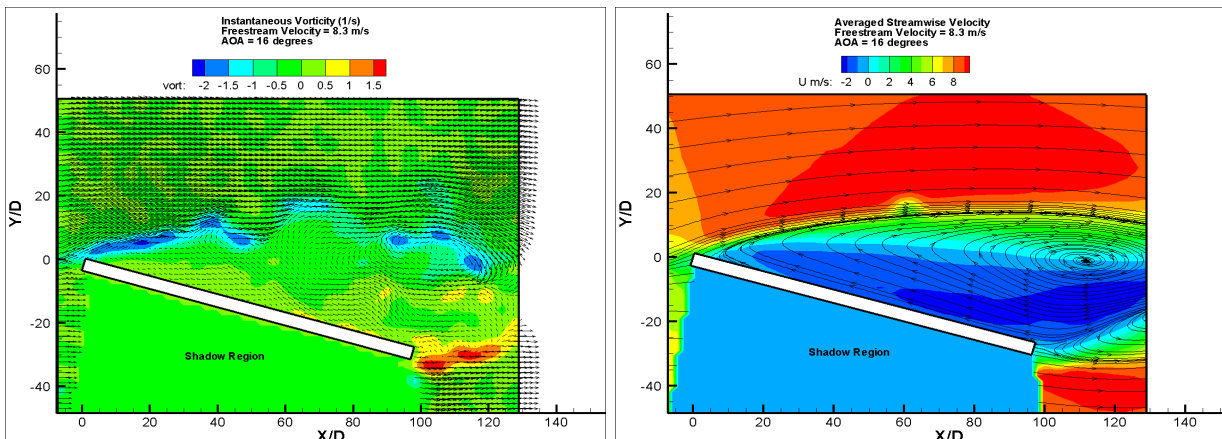
Figure 46. Instantaneous velocity vectors and spanwise vorticity distribution (left) and ensemble-averaged streamlines (right) around the flat plate at AOA = 16 degrees.
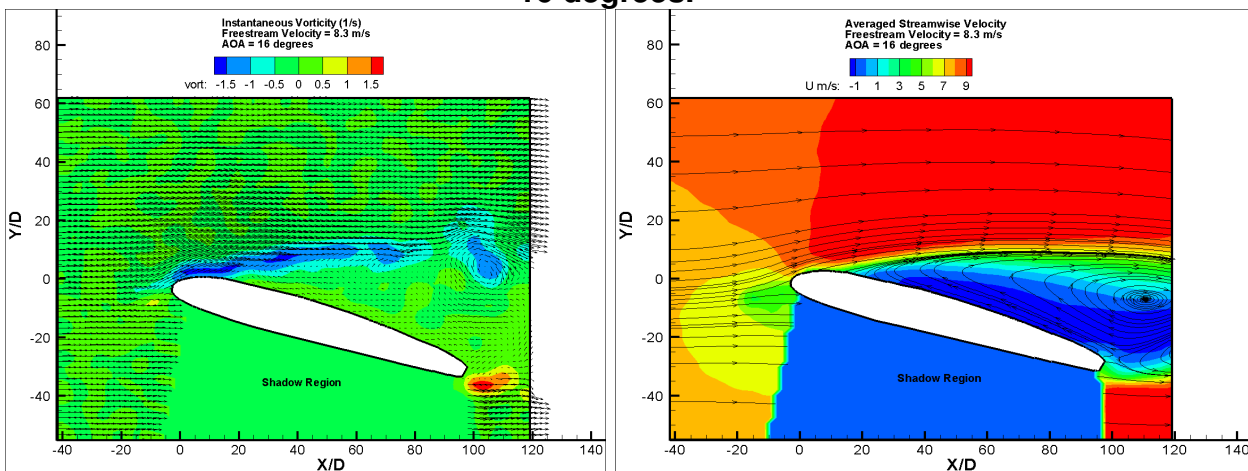
Figure 47. Instantaneous velocity vectors and spanwise vorticity distribution (left) and ensemble-averaged streamlines (right) around the wrapped dragonfly airfoil at AOA = 16 degrees.
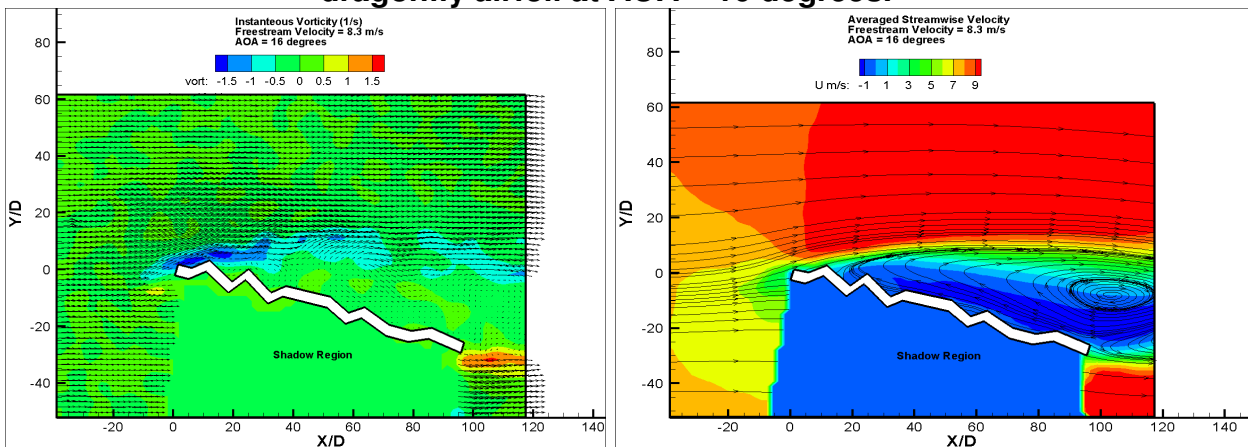
Figure 48. Instantaneous velocity vectors and spanwise vorticity distribution (left) and ensemble-averaged streamlines (right) around the dragonfly airfoil at AOA = 16 degrees.
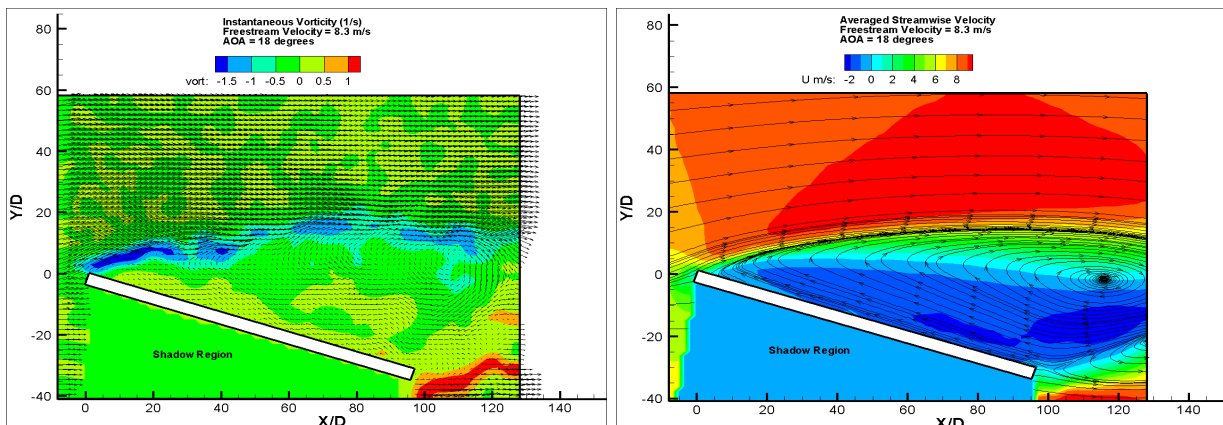
Figure 49. Instantaneous velocity vectors and spanwise vorticity distribution (left) and ensemble-averaged streamlines (right) around the flat plate at AOA = 18 degrees.
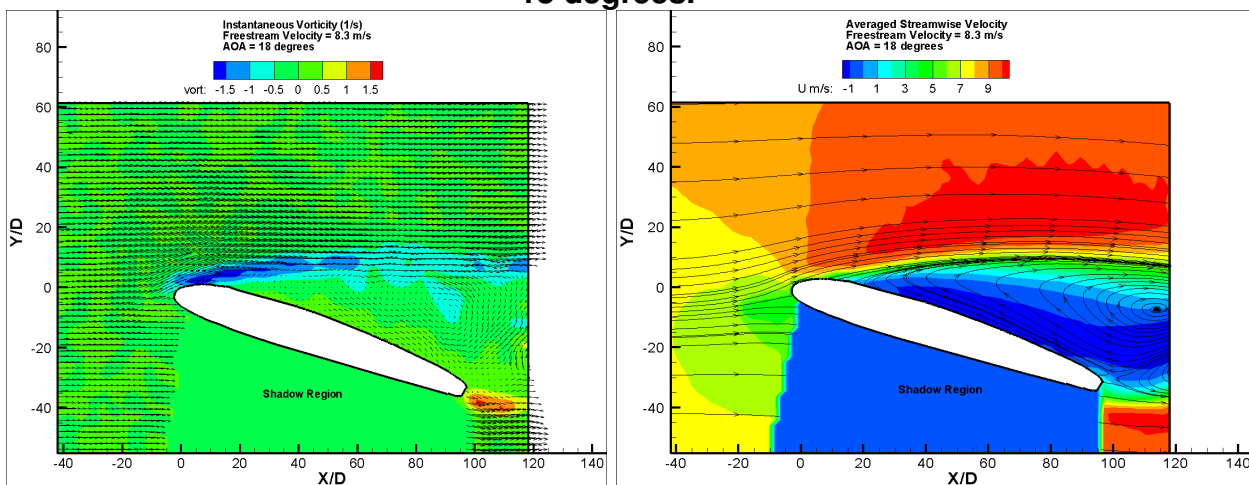
Figure 50. Instantaneous velocity vectors and spanwise vorticity distribution (left) and ensemble-averaged streamlines (right) around the wrapped dragonfly airfoil at AOA = 18 degrees.
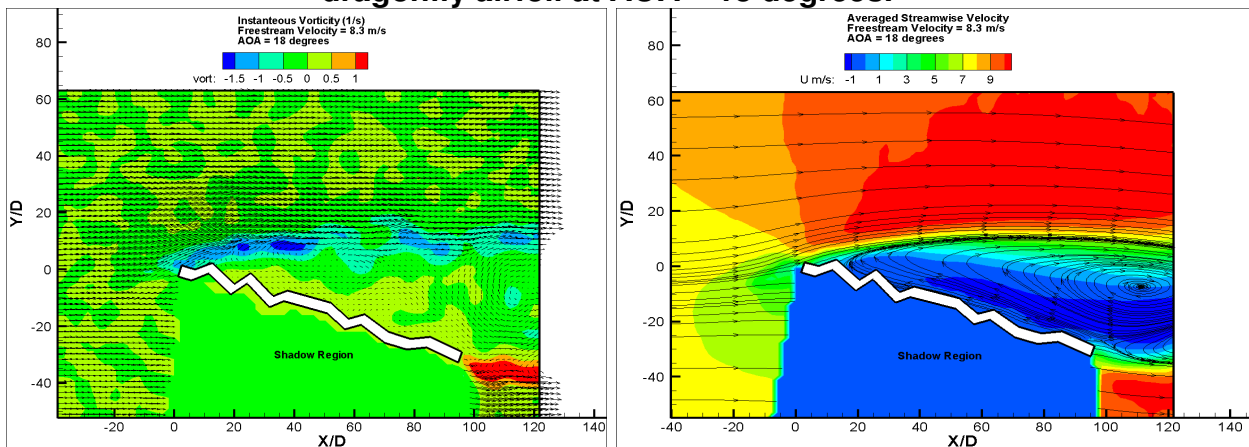
Figure 51. Instantaneous velocity vectors and spanwise vorticity distribution (left) and ensemble-averaged streamlines (right) around the dragonfly airfoil at AOA = 18 degrees.
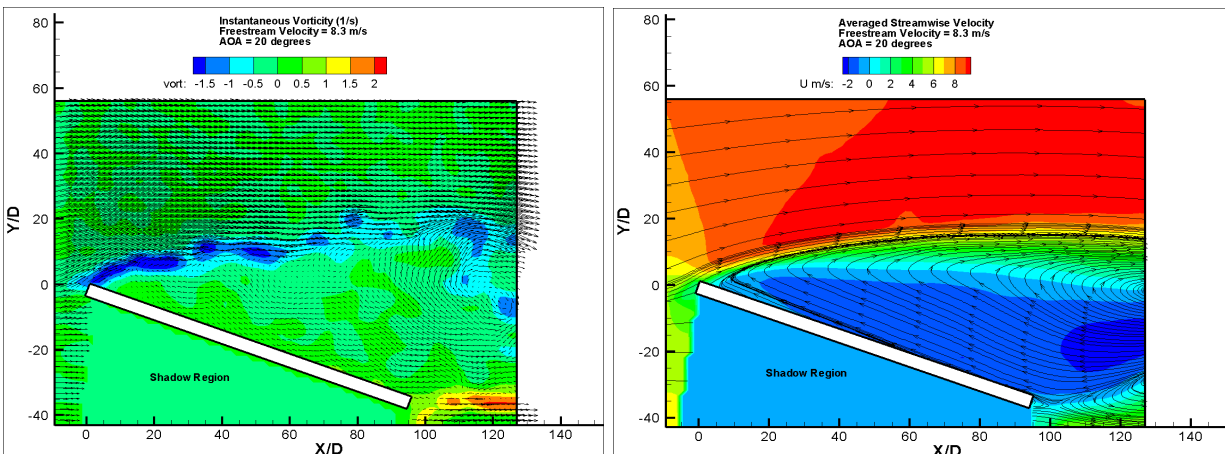
Figure 52. Instantaneous velocity vectors and spanwise vorticity distribution (left) and ensemble-averaged streamlines (right) around the flat plate at AOA = 20 degrees.
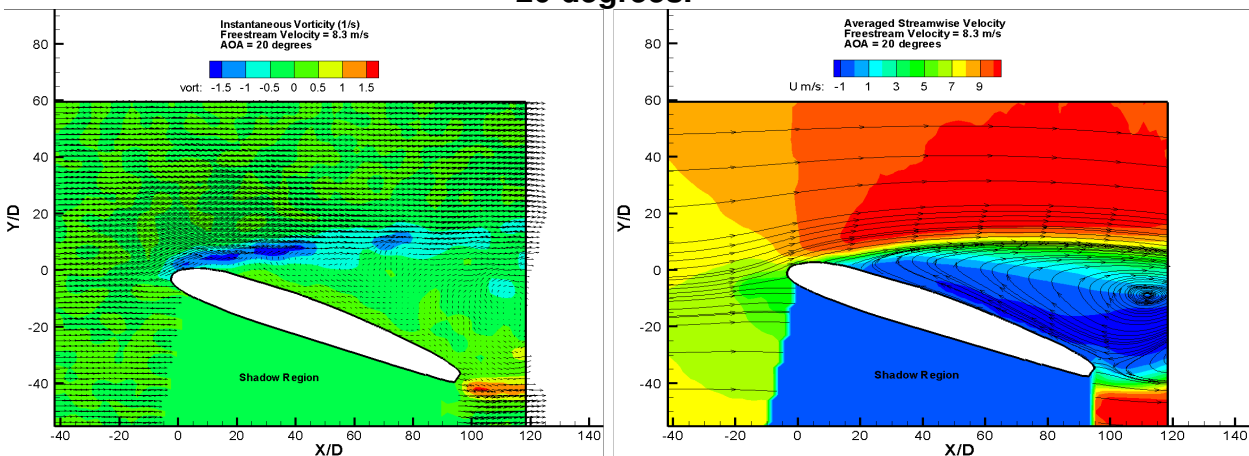
Figure 53. Instantaneous velocity vectors and spanwise vorticity distribution (left) and ensemble-averaged streamlines (right) around the wrapped dragonfly airfoil at AOA = 20 degrees.
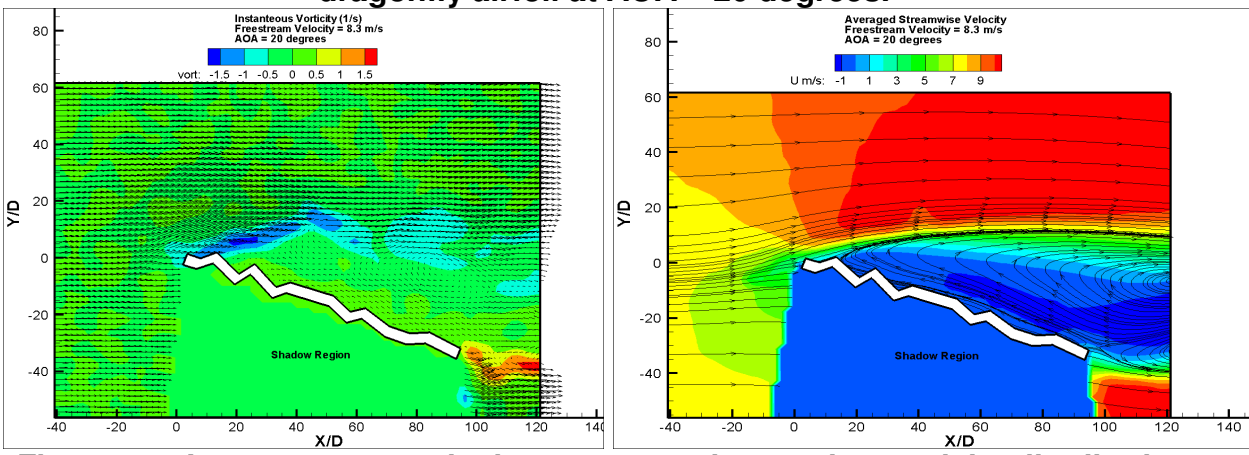
Figure 54. Instantaneous velocity vectors and spanwise vorticity distribution (left) and ensemble-averaged streamlines (right) around the dragonfly airfoil at AOA = 20 degrees.

AOA = 2 degrees AOA = 4 degrees AOA = 6 degrees

AOA = 8 degrees AOA = 10 degrees AOA = 12 degrees

AOA = 14 degrees AOA = 16 degrees AOA = 18 degrees

AOA = 20 degrees
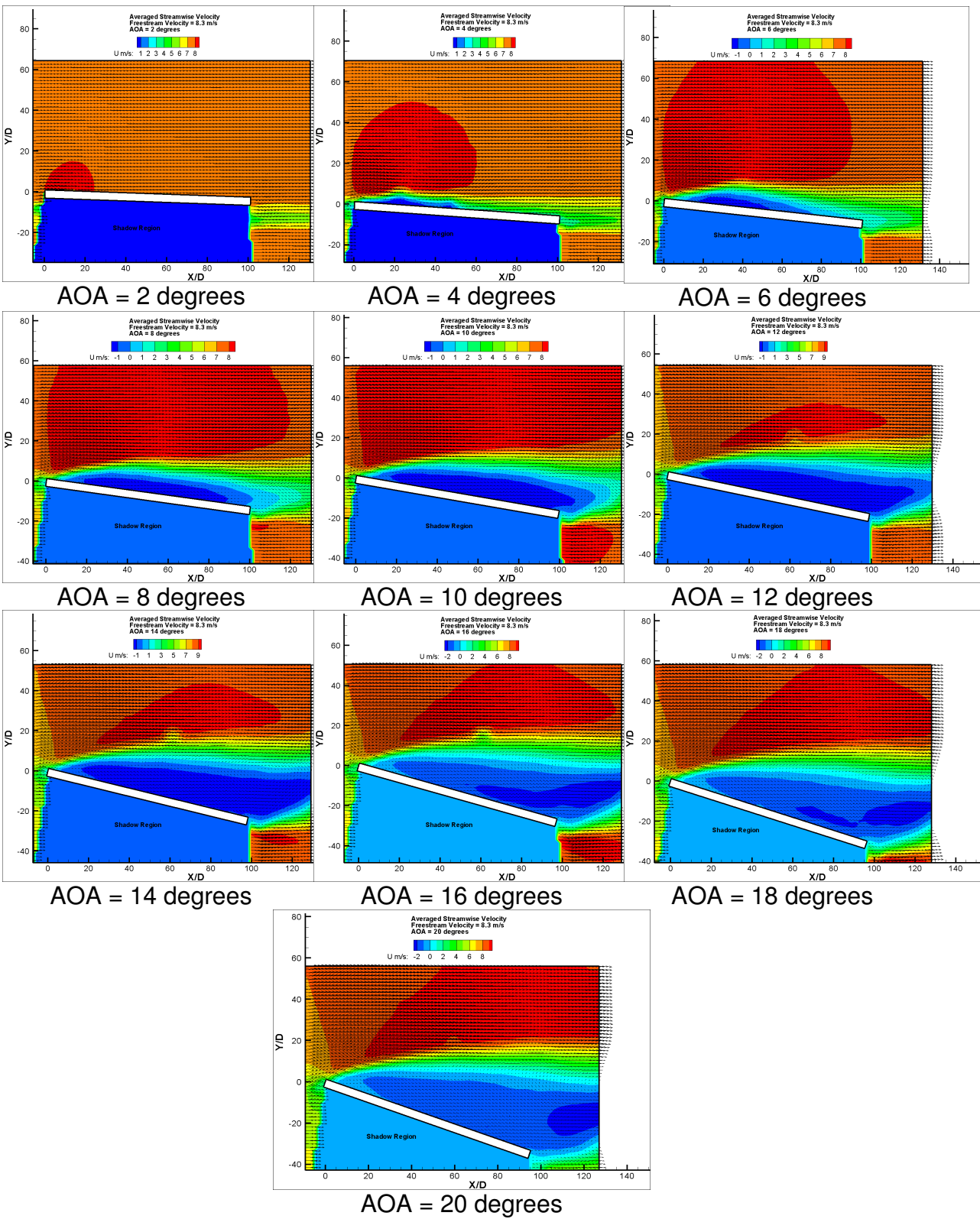
Figure 55. Ensemble-averaged velocity vectors around the flat plate.

AOA = 2 degrees   AOA = 4 degrees   AOA = 6 degrees

AOA = 8 degrees   AOA = 10 degrees   AOA = 12 degrees

AOA = 14 degrees   AOA = 16 degrees   AOA = 18 degrees

AOA = 20 degrees
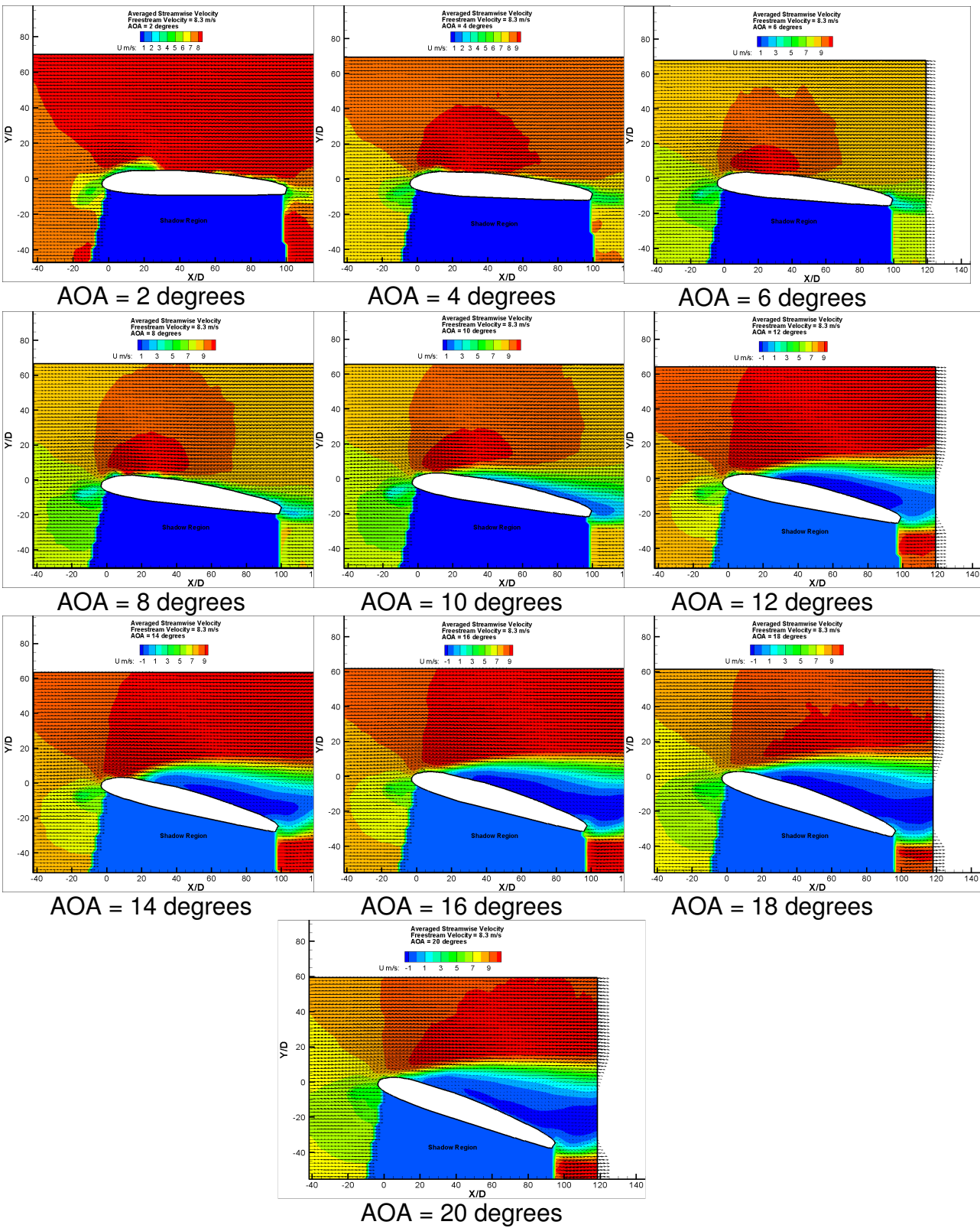
Figure 56. Ensemble-averaged velocity vectors around the wrapped dragonfly airfoil.
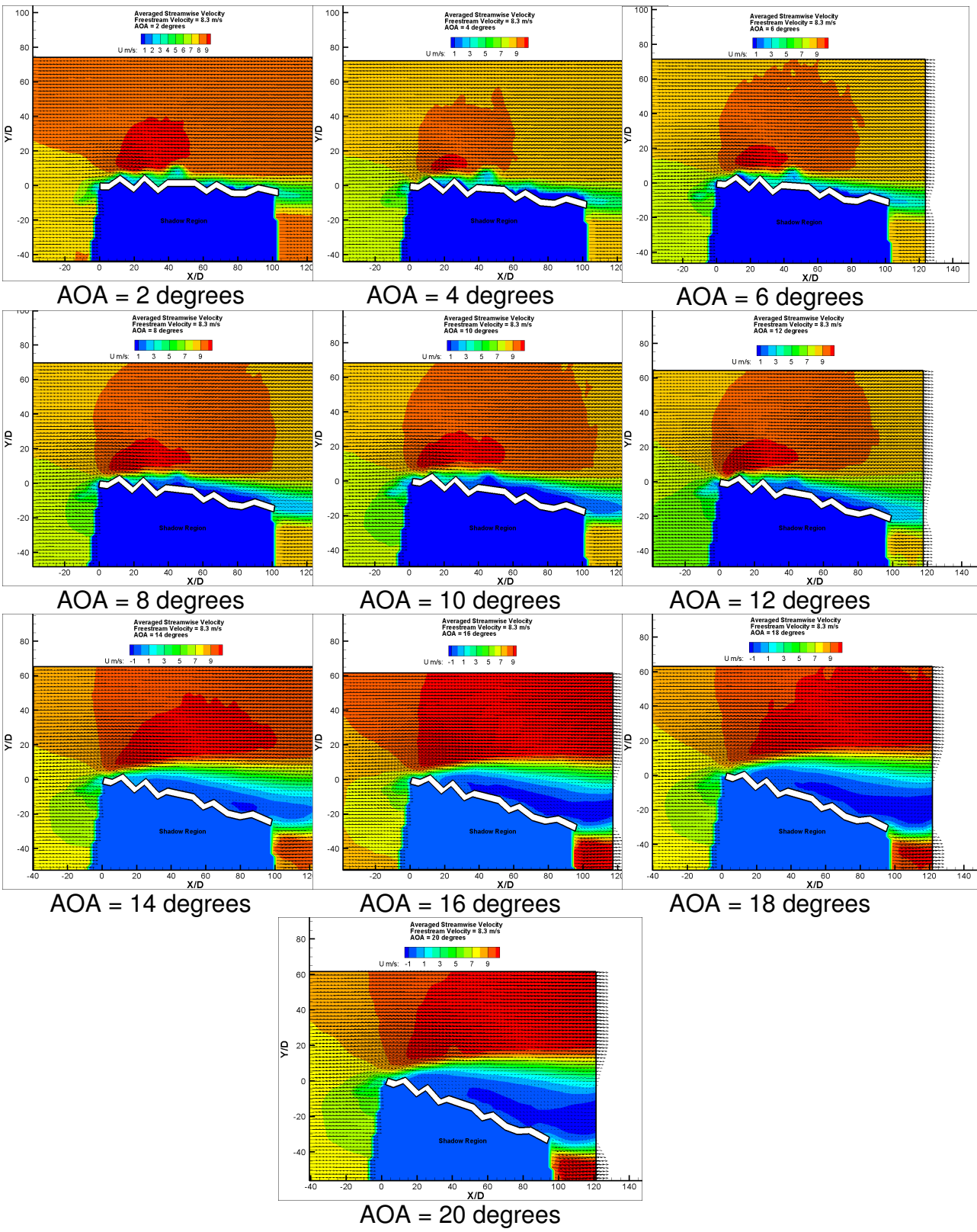
Figure 57. Ensemble-averaged velocity vectors around the dragonfly airfoil.

Figures 25-27 shows the flow over the three test airfoils at 2 degrees angle of attack. As is shown in the figures by the ensemble-averaged streamlines, the flow is closely following the surface of the airfoil; with the exception of the dragonfly airfoil in which the flow does not follow the corrugated shape directly, but an 'envelope' shape very similar to the physical boundary of the wrapped dragonfly airfoil (motivating this study). It is clear that there is no separation over any of the test airfoils at this low angle of attack. Also, it can be seen from the instantaneous vorticity distribution that there is a thin vortex layer of negative sense over the upper surface of the airfoils; this is a visualization of the boundary layer attached to the surface of the airfoils, or the envelope profile in the case of the corrugated dragonfly airfoil. The instantaneous velocity vectors also show that there is little momentum deficit in the flow where the vectors exit the measurement frame behind the airfoil. This low momentum deficit is directly related to the drag due to the airfoil, which in the case of 2 degrees angle of attack is quite low. This fact is reemphasized in the mean velocity vectors in Figures 55-57.

Figures 28-30 show the flow over the airfoils at 4 degrees AOA. The picture here is very similar to that of 2 degrees AOA. The wrapped dragonfly and corrugated dragonfly airfoils both continue to have attached flow (boundary layer) at the surface of the airfoil. The flat plate is experiencing small separation bubbles on the upper surface of the airfoil at 4 degrees. It can also be seen from the mean velocity vectors shown in Figure 55 for 4 degrees angle of attack that the separation bubbles have increased the momentum deficit and thus the drag when compared to 2 degrees AOA.

In Figures 31-39 the airfoils are shown with increasing angle of attack from 6 degrees to 10 degrees. Both the wrapped and corrugated dragonfly airfoils continue to have attached

flow and boundary layers with nominal momentum deficits that increase only slightly. The flat plate however, is completely stalled by 10 degrees angle of attack. As the angle of attack increases, the adverse pressure gradient over the upper surface of the flat plate (and the other airfoils) becomes stronger. The laminar boundary layer of the flat plate cannot resist this adverse pressure gradient and therefore detaches from the body and a region of circulating flow forms over the airfoil's upper surface. At 6 degrees angle of attack, the separated region spans approximately half of the upper surface of the flat plate. At 8 degrees AOA, the separated region extends both directions and the entire surface of the flat plate is stalled. As shown in the instantaneous velocity vectors and the mean velocity vectors, the momentum deficit increases significantly with the growing separated region as the angle of attack increases.

Figures 40-42 are somewhat the *coup de grâce* of the PIV measurements. The afore mentioned figures show the test airfoils at 12 degrees angle of attack and clearly show that the flow over the flat plate and wrapped dragonfly airfoil to be detached from the surface whereas the corrugated dragonfly airfoil shows streamlines still smoothly following the same envelope shape as in the lower angles of attack. The instantaneous vorticity distribution shown in the figures lend to this fact by showing separated boundary layers for the flat plate and wrapped dragonfly airfoils, but attached (to the envelope profile) to the corrugated dragonfly airfoil. This is the required evidence to show that the corrugations of the dragonfly airfoil are the cause of the increased performance at low chord Reynolds number. Furthermore, the ensemble-averaged velocity vectors reflect this by showing the relatively low momentum deficit of the corrugated dragonfly airfoil when compared to the flat plate and the wrapped dragonfly airfoil.

Figures 43-45 show the test airfoils at 14 degrees angle of attack. At this high angle of attack, the boundary layers over the airfoils cannot resist the strength of the adverse pressure gradient and separate from the body. It is noted however that the corrugated dragonfly does provide a little drag relief as is evidenced by the momentum deficit shown by the ensemble-averaged velocity vectors shown in Figure 57.

Figures 46-54 show the remaining results for angles of attack from 16 to 20 degrees AOA. In this range of angle of attack all of the test airfoils have succumb to complete airfoil stall and the corrugated dragonfly airfoil behavior closely matches that of the wrapped dragonfly airfoil.

A closer inspection of the flow is necessary to understand why the corrugations of the dragonfly airfoil improve the performance over the other test airfoils. The following figures (Figures 58-66) show a zoomed in region of less than 50% of the upper surface of the test airfoils. The measurement window size is approximately 45 mm x 25 mm. The results will be discussed in more detail after the presentation of the figures.

Flat plate, AOA = 6 degrees

Flat plate, AOA = 8 degrees

Flat plate, AOA = 10 degrees

Flat plate, AOA = 12 degrees

Flat plate, AOA = 14 degrees
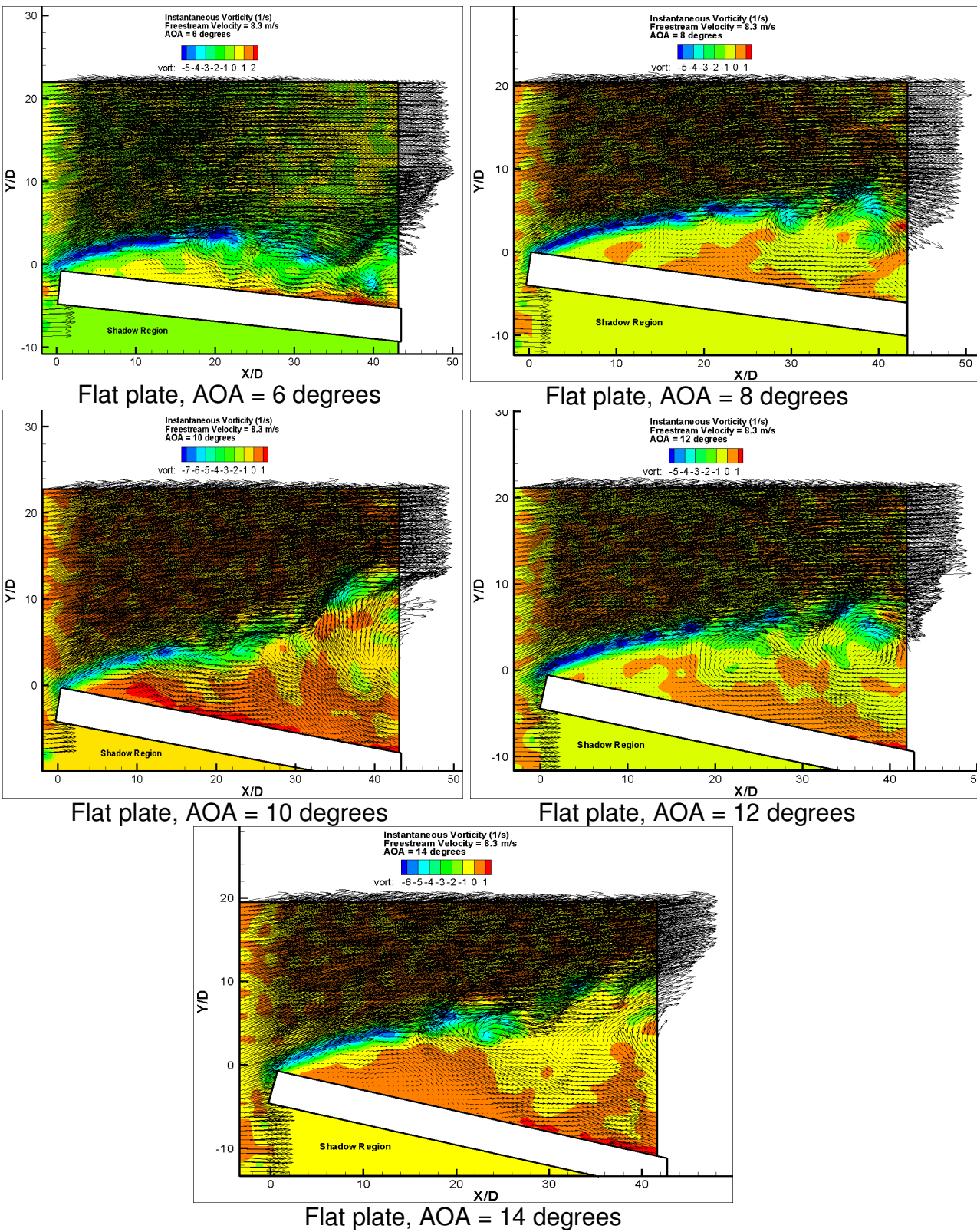
Figure 58. Instantaneous velocity vectors and spanwise vorticity distribution close to the leading edge of the flat plate.

Flat plate, AOA = 6 degrees

Flat plate, AOA = 8 degrees

Flat plate, AOA = 10 degrees

Flat plate, AOA = 12 degrees

Flat plate, AOA = 14 degrees
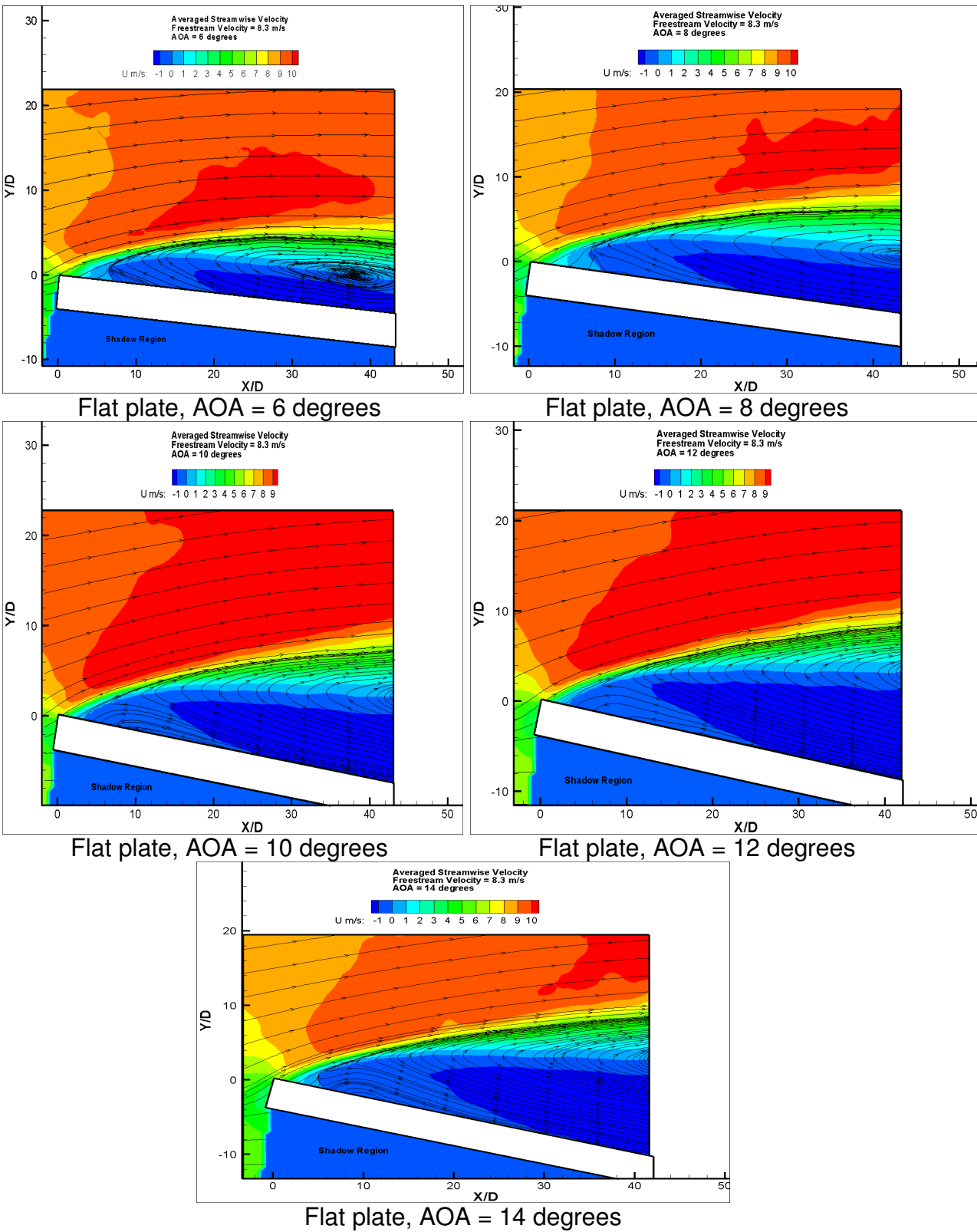
Figure 59. Ensemble-averaged streamlines close to the leading edge of the flat plate.

Flat plate, AOA = 6 degrees

Flat plate, AOA = 8 degrees

Flat plate, AOA = 10 degrees

Flat plate, AOA = 12 degrees
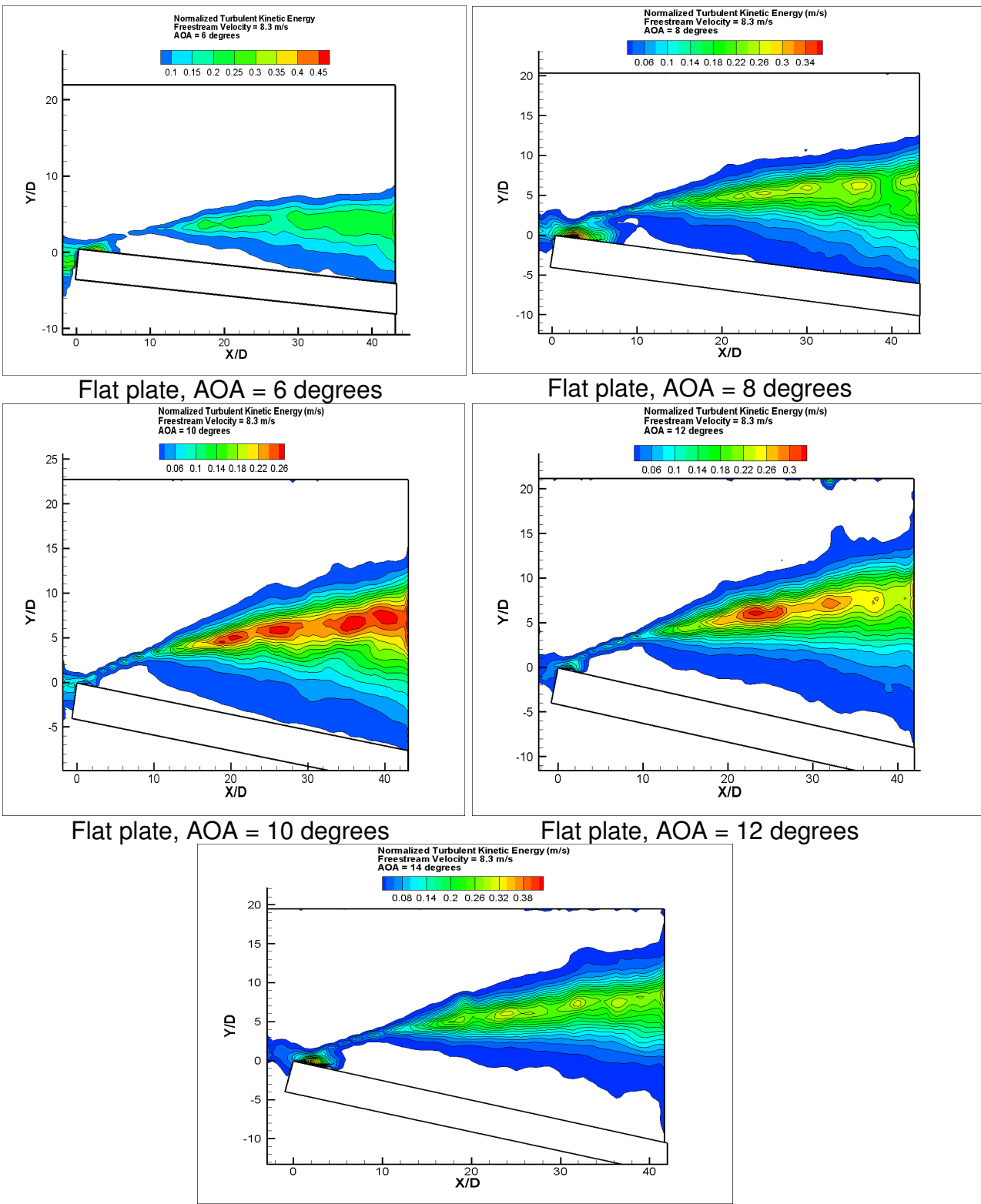
Flat plate, AOA = 14 degrees

Figure 60. Turbulent kinetic energy distribution close to the leading edge of the flat plate.

Wrapped dragonfly, AOA = 6 degrees

Wrapped dragonfly, AOA = 8 degrees

Wrapped dragonfly, AOA = 10 degrees

Wrapped dragonfly, AOA = 12 degrees

Wrapped dragonfly, AOA = 14 degrees
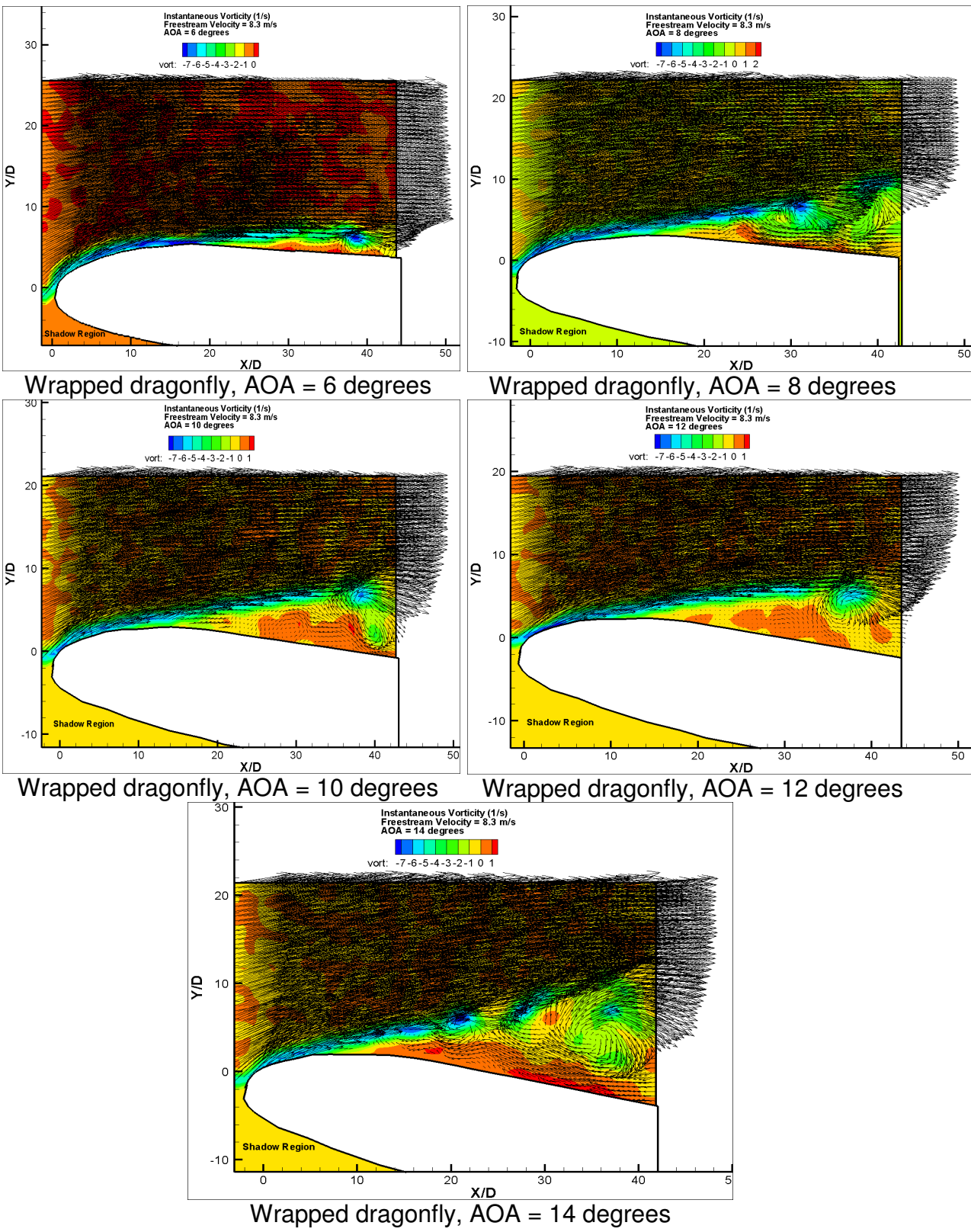
Figure 61. Instantaneous velocity vectors and spanwise vorticity distribution close to the leading edge of the wrapped dragonfly airfoil.
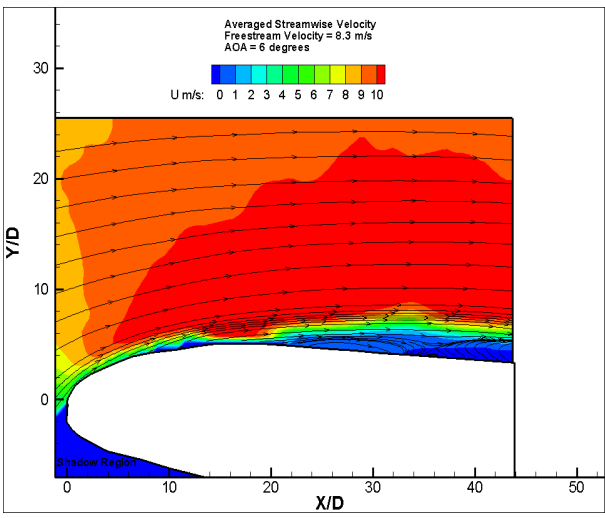
Wrapped dragonfly, AOA = 6 degrees
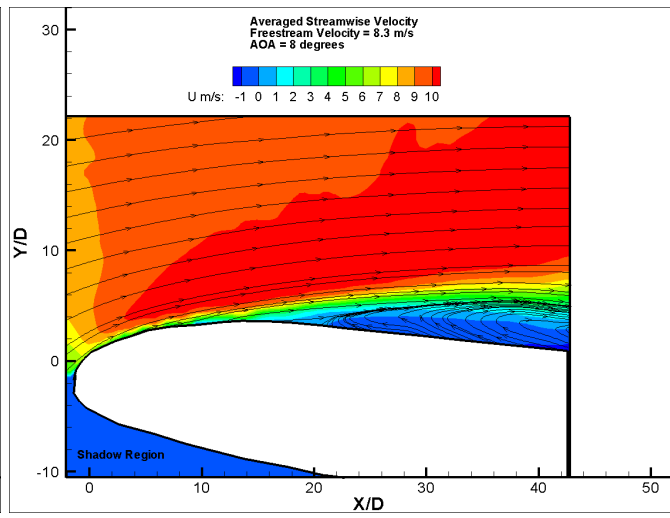
Wrapped dragonfly, AOA = 8 degrees
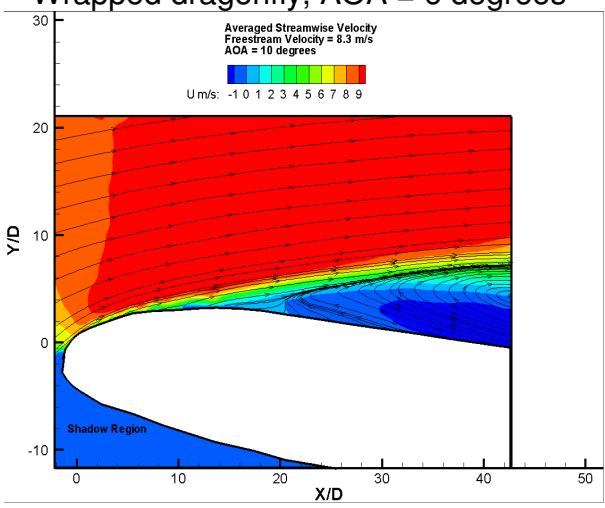
Wrapped dragonfly, AOA = 10 degrees
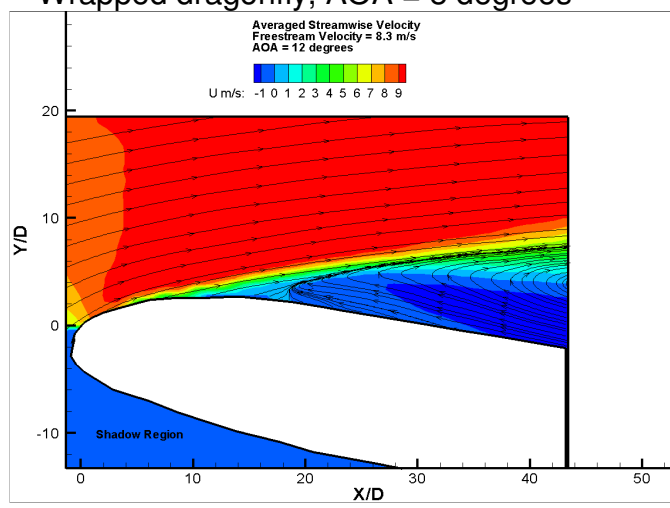
Wrapped dragonfly, AOA = 12 degrees
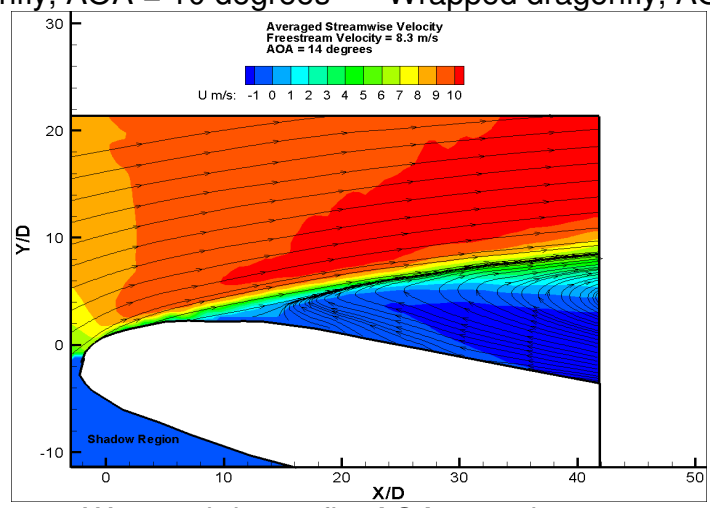
Wrapped dragonfly, AOA = 14 degrees

Figure 62. Ensemble-averaged streamlines close to the leading edge of the wrapped dragonfly airfoil.
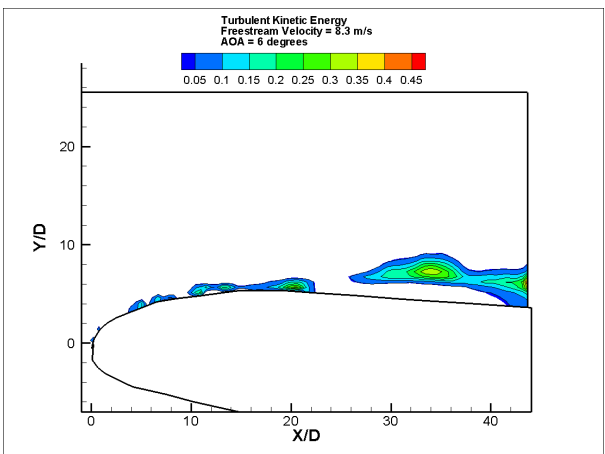
Wrapped dragonfly, AOA = 6 degrees
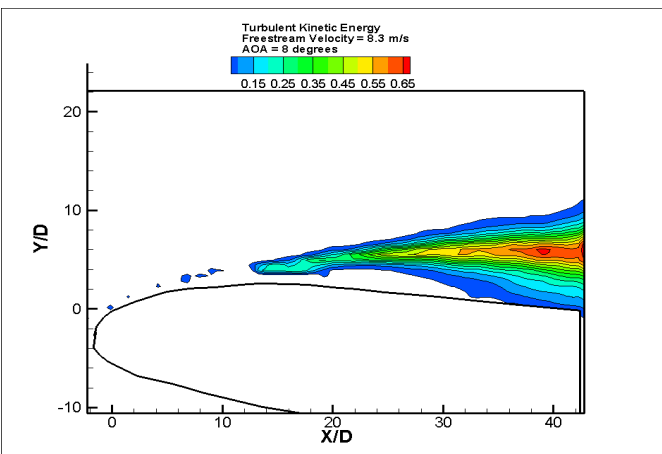
Wrapped dragonfly, AOA = 8 degrees
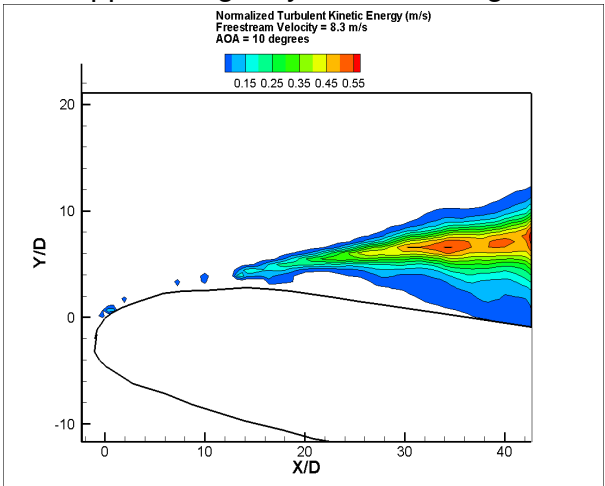
Wrapped dragonfly, AOA = 10 degrees
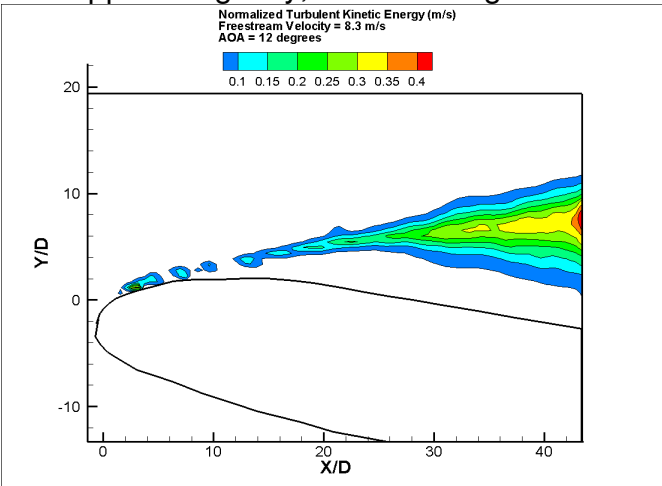
Wrapped dragonfly, AOA = 12 degrees
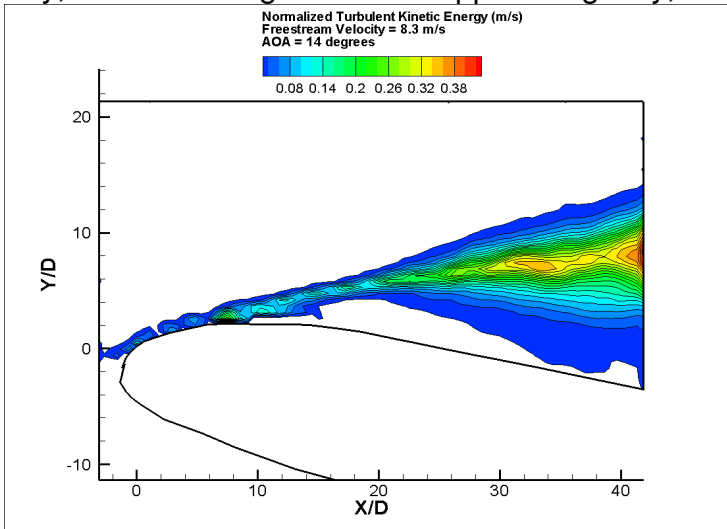
Wrapped dragonfly, AOA = 14 degrees

Figure 63. Turbulent kinetic energy distribution close to the leading edge of the wrapped dragonfly airfoil.

Dragonfly, AOA = 6 degrees

Dragonfly, AOA = 8 degrees

Dragonfly, AOA = 10 degrees

Dragonfly, AOA = 12 degrees

Dragonfly, AOA = 14 degrees
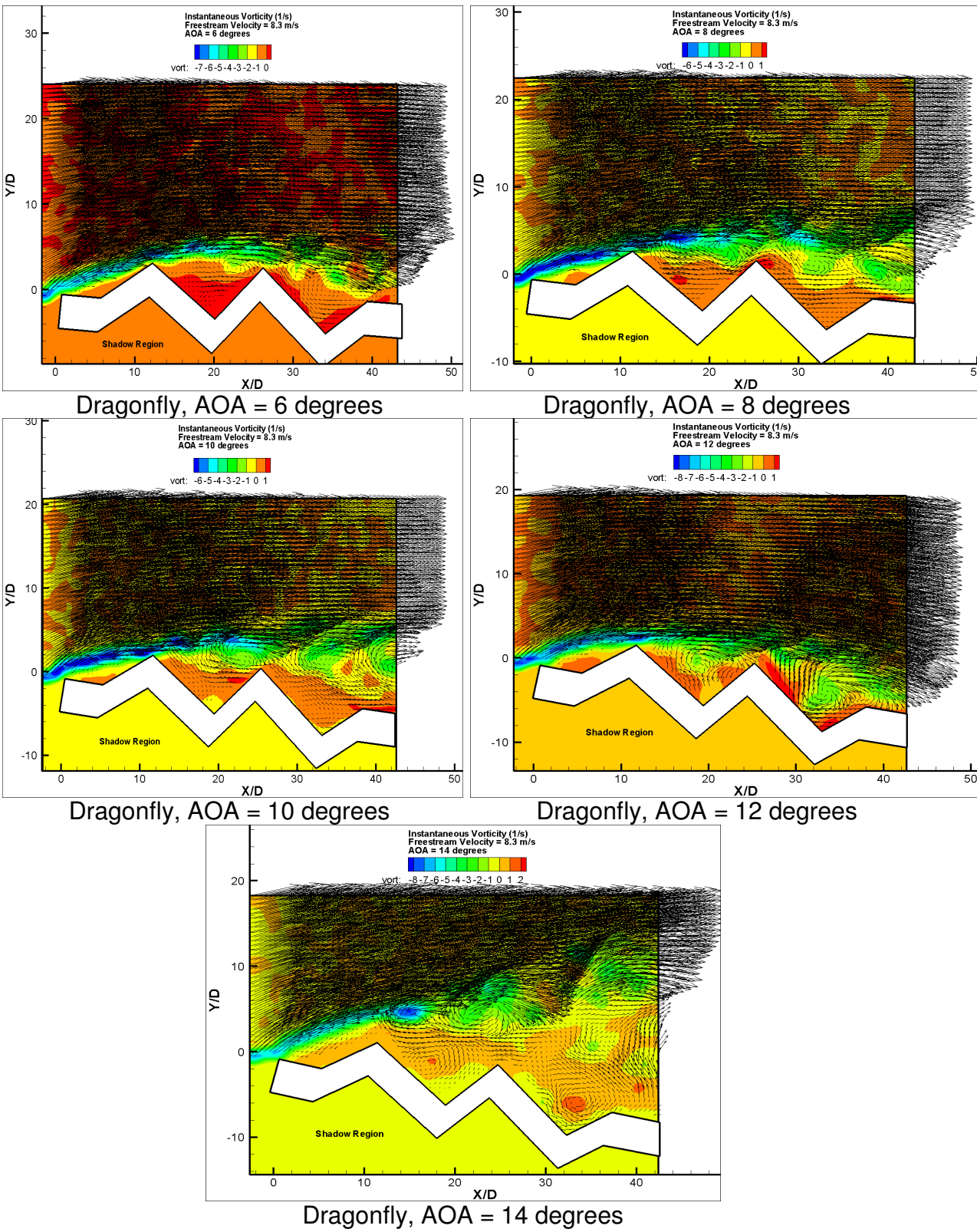
Figure 64. Instantaneous velocity vectors and spanwise vorticity distribution close to the leading edge of the dragonfly airfoil.

Dragonfly, AOA = 6 degrees

Dragonfly, AOA = 8 degrees

Dragonfly, AOA = 10 degrees

Dragonfly, AOA = 12 degrees

Dragonfly, AOA = 14 degrees
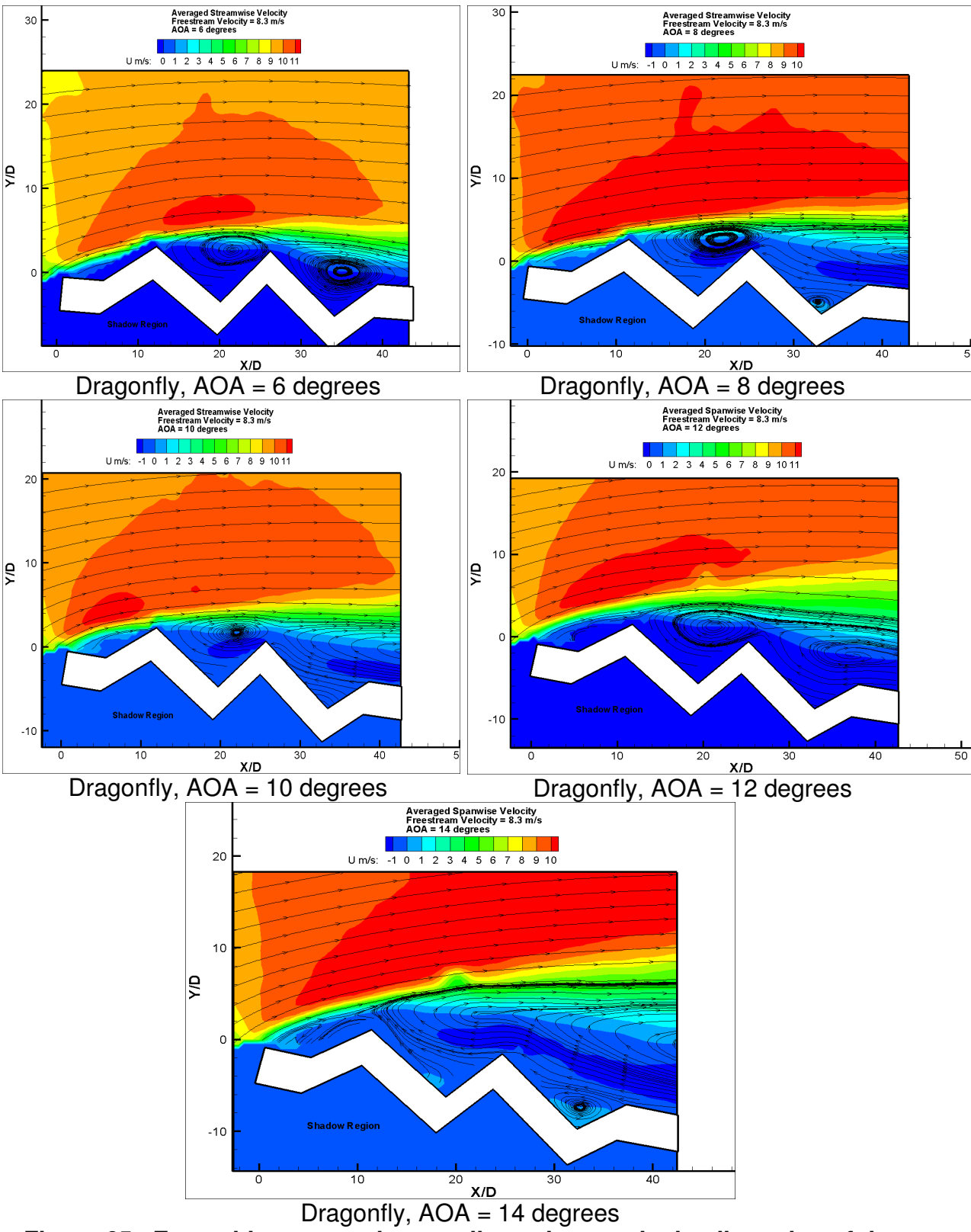
Figure 65. Ensemble-averaged streamlines close to the leading edge of the dragonfly airfoil.
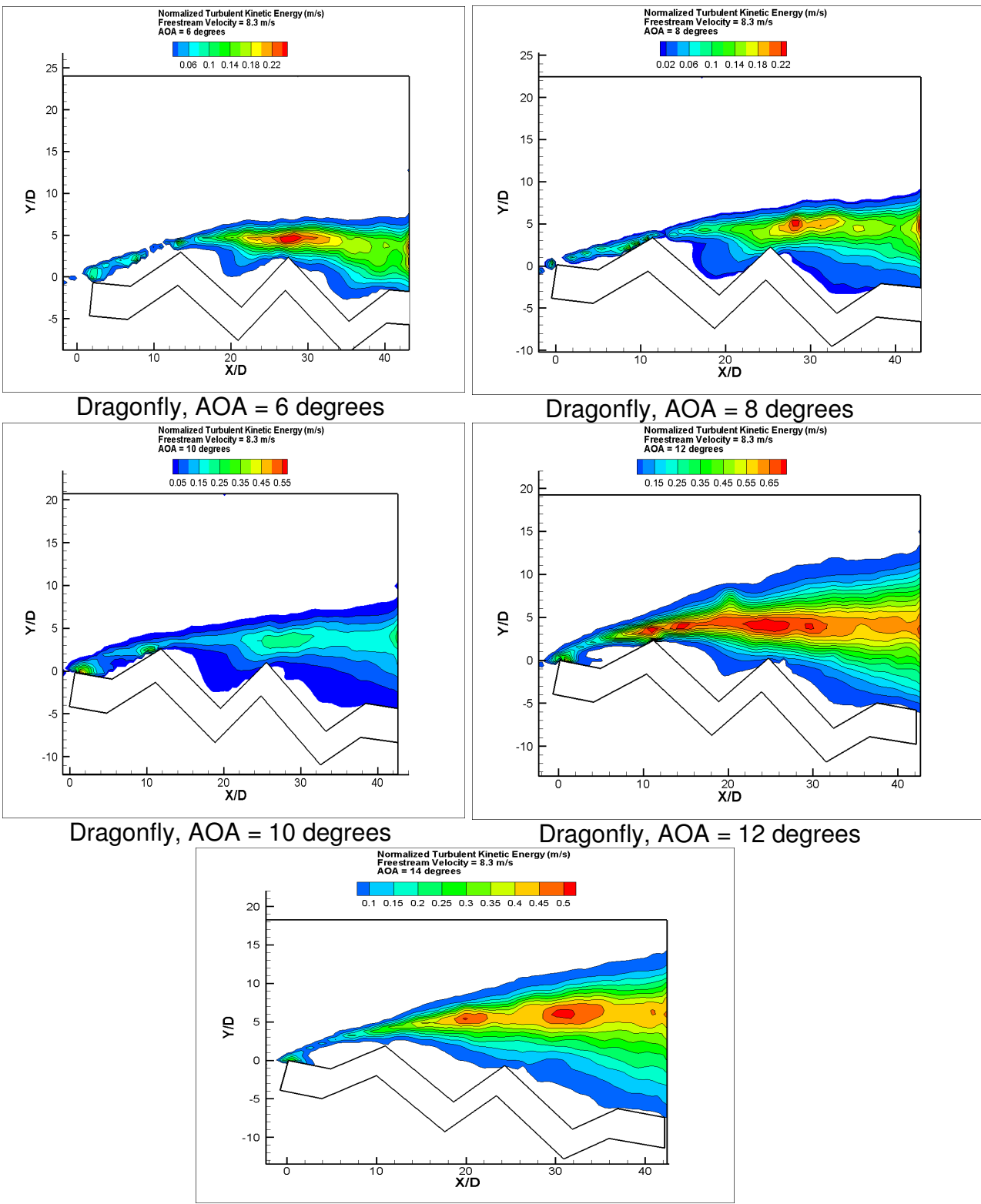
Dragonfly, AOA = 6 degrees

Dragonfly, AOA = 8 degrees

Dragonfly, AOA = 10 degrees

Dragonfly, AOA = 12 degrees

Dragonfly, AOA = 14 degrees

Figure 66. Turbulent kinetic energy distribution close to the leading edge of the dragonfly airfoil.

Figures 58-60 show the region of the flow immediately surrounding the leading edge of the flat plate. It is evident by the results for the ensemble-averaged streamlines (Figure 59) that the flat plate is experiencing separated flow even at the low angle of attack 6 degrees. It is known from the full view figures that at 6 degrees AOA the flow does reattach to the surface of the flat plate forming a separation bubble, and also that for the higher angles of attack the boundary layer never recovers and completely separates from the airfoil surface due to the adverse pressure gradient. Figure 58 shows a laminar boundary layer separating at the leading edge of the airfoil in all cases, and then rapidly transitioning into turbulence and forming unsteady vortex structures as a result of Kelvin-Helmholtz instabilities. The turbulent kinetic energy shown in Figure 60 also demonstrates this fact; it shows only a very thin low magnitude layer near the leading edge and as the boundary layer transitions the wake of the turbulent kinetic energy broadens over the surface of the airfoil. It is also noted from the figure that the turbulent kinetic energy in the case of AOA = 6 degrees (the only angle of attack where the flow reattaches to the surface), is considerably lower than in the higher angle of attack cases. It is believed that this lower turbulent energy is due to the boundary layer remaining in a transitioning state rather than becoming a fully turbulent boundary layer and is able to overcome a weaker adverse pressure gradient and reattaches as a semi-laminar boundary layer on the surface of the flat plate. Figures 58-60 also provide the visualization of the boundary layer separation increasing with angle of attack. In Figure 58, the vortex layer is seen increasingly elevating from the surface of the flat plate with increasing angle of attack. This same phenomenon is also evident by the streamlines of the recirculation region deflecting higher from the surface, and the turbulent kinetic energy pulling away from the surface as the angle of attack increases.

The flow around the leading edge of the wrapped dragonfly airfoil is shown in Figures 61-63. These figures offer a look at the flow not seen in the full view figures; in particular, there are separation bubbles on the surface of the airfoil before it experiences stall at 12 degrees AOA. At angle of attack 6 degrees the streamlines indicate a very small separated recirculation region as the flow leaves the measurement window. As the angle of attack increases to 8 and 10 degrees AOA, the size of the separation bubble also increases along with the strength of the adverse pressure gradient. The instantaneous velocity vectors and vorticity distribution shown in Figure 61 exhibit similar features to that of the flat plate described for the flat plate. A notable feature of the results in Figure 61 is that as the angle of attack increases, the adverse pressure gradient strengthens and the transition of the boundary layer from laminar to turbulent moves upstream closer to the leading edge of the airfoil. Figure 63 shows the results of the turbulent kinetic energy of the flow and also illustrates this trend; as the angle of attack increases, the turbulent energy near the leading edge increases. Also to note in Figure 63 is a similar behavior of the turbulent kinetic energy pulling away from the surface of the airfoil as the angle of attack increases representing the boundary layer separation increase. Figures 61 and 62 support this proposal by showing the vortex layer of the boundary layer and the streamlines deflecting higher from the surface of the airfoil with increasing angle of attack.

Figures 64-66 show the results for the corrugated dragonfly airfoil. It is immediately obvious by inspection of Figures 64 and 65 that the flow has taken on a much more complex flow pattern. An interesting aspect of Figure 64 which shows the instantaneous velocity vectors and vorticity is that the boundary layer begins much the same as the flat plate and wrapped dragonfly airfoil boundary layers as a smooth laminar flow. The difference

however, is when the boundary layer of the corrugated dragonfly airfoil reaches the first peak of the corrugation; the boundary layer is suddenly 'tripped' into turbulence. It can be seen from the figure that the now turbulent boundary layer follows the envelope shape of the streamlines until the airfoil is stalled at 14 degrees AOA. This phenomenon is quite similar to the well known physics of a dimpled golf ball in which the dimples act to reduce separation by creating a turbulent boundary layer over the ball. The ensemble-averaged streamlines (Figure 65) show that the corrugation has trapped an unsteady vortex structure within the valleys of the airfoil. Of interest is how the vortex structures change with angle of attack. At 6 degrees angle of attack, the results show two discrete vortex structures of the same clockwise sense in the valleys that can be seen in the measurement window. At 8 degrees AOA the vortex structure in the first valley is the same as in the 6 degree AOA case, however the vortex in the second valley from the leading edge appears to be pushed down into the valley by a larger structure coming from downstream. At 10 degrees AOA, the vortex structure in the second valley from the leading edge is no longer visible and only the larger structure from out of the measurement window and the vortex structure in the first valley remain. At 12 degrees AOA, the separated region from the downstream structure has moved up the airfoil and is beginning to merge with the vortex in the first valley; and at 14 degrees angle of attack the larger structure has engulfed the structure from the first valley and the airfoil is stalled. Also interesting in the 14 degrees angle of attack case is the new vortex structure forming in the second valley that has opposite sense as the original clockwise vortex structure – the corrugations are now performing the same function but with a reversed flow direction. The turbulent kinetic energy shown in Figure 66 supports the idea of the peak acting as a boundary layer trip; the figure shows a thin, low magnitude layer of turbulent

energy coming up from the leading edge and then widening and strengthening after reaching the first peak. The separation of the boundary layer after airfoil stall can also be observed in the turbulent kinetic energy; before airfoil stall, the turbulent kinetic energy is concentrated on the envelope profile and dips down into the valleys of the corrugation, in contrast after airfoil stall, the turbulent kinetic energy begins to separate from the envelope profile and no energy is seen in the corrugations of the airfoil.

In order to observe more of the airfoil surface, the measurement window size was increased to 75 mm x 45 mm. The results are presented in the following pages and will be discussed in detail after the presentation of the figures. Figures 67-72 show the results of the instantaneous velocity vectors and vorticity distribution, and the ensemble-averaged streamlines for the flat plate, wrapped dragonfly airfoil, and corrugated dragonfly airfoil respectively. The angle of attack range is shown for 6 to 14 degrees by two degree increments.

Flat plate, AOA = 6 degrees

Flat plate, AOA = 8 degrees

Flat plate, AOA = 10 degrees

Flat plate, AOA = 12 degrees

Flat plate, AOA = 14 degrees
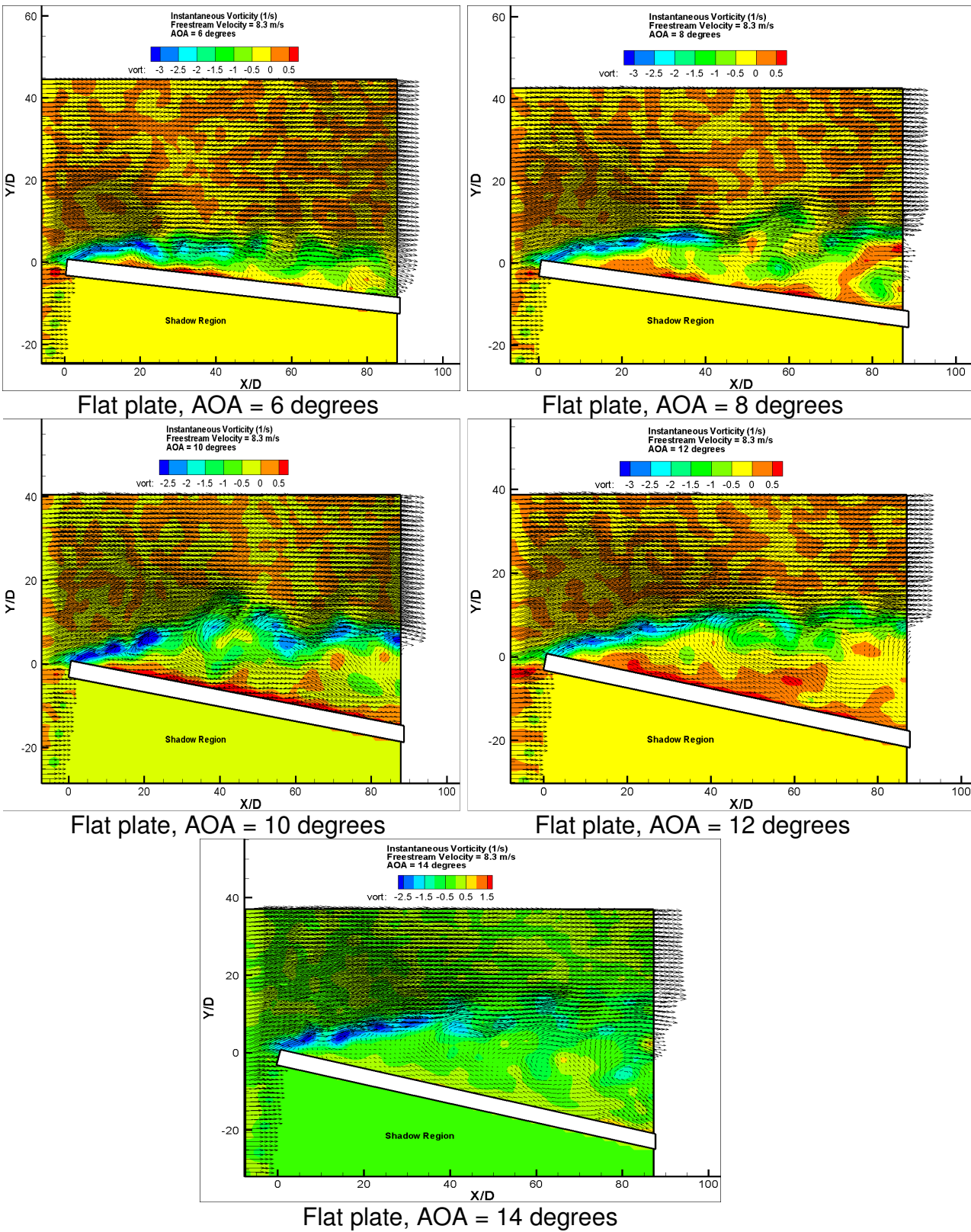
Figure 67. Instantaneous velocity vectors and spanwise vorticity distribution over upper surface of the flat plate.

Flat plate, AOA = 6 degrees

Flat plate, AOA = 8 degrees

Flat plate, AOA = 10 degrees

Flat plate, AOA = 12 degrees

Flat plate, AOA = 14 degrees
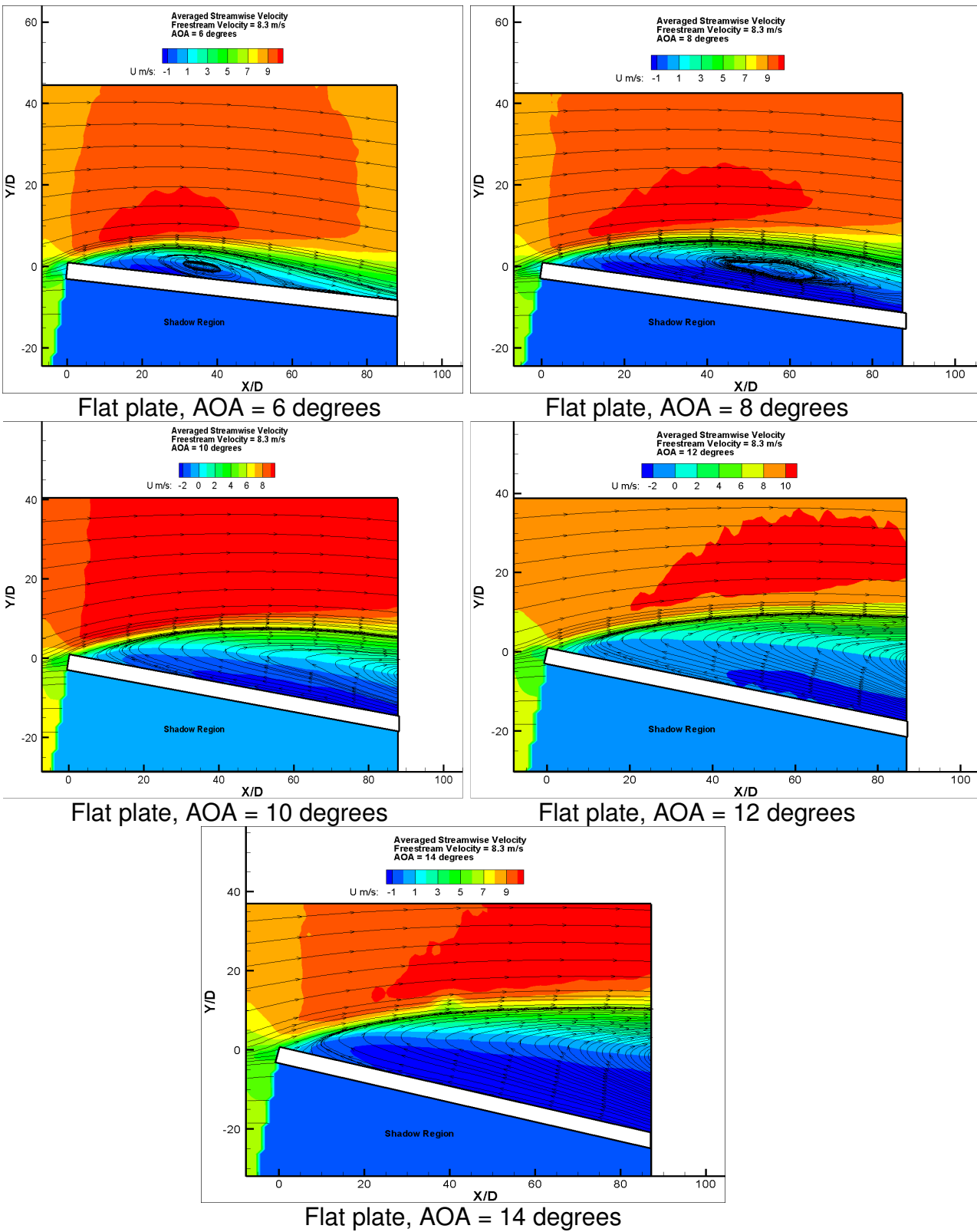
Figure 68. Ensemble-averaged streamlines over the upper surface of the flat plate.
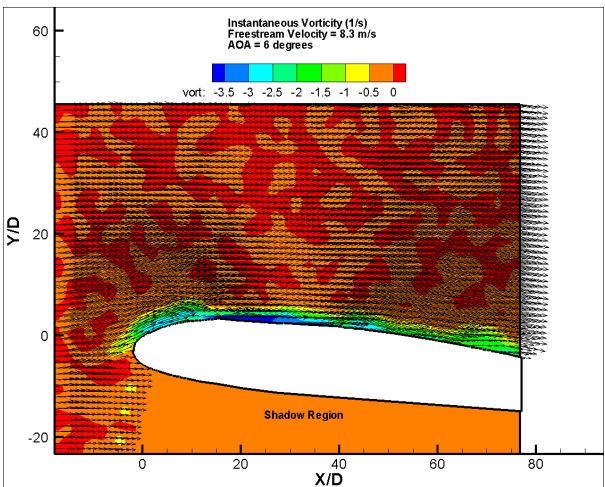
Wrapped dragonfly, AOA = 6 degrees
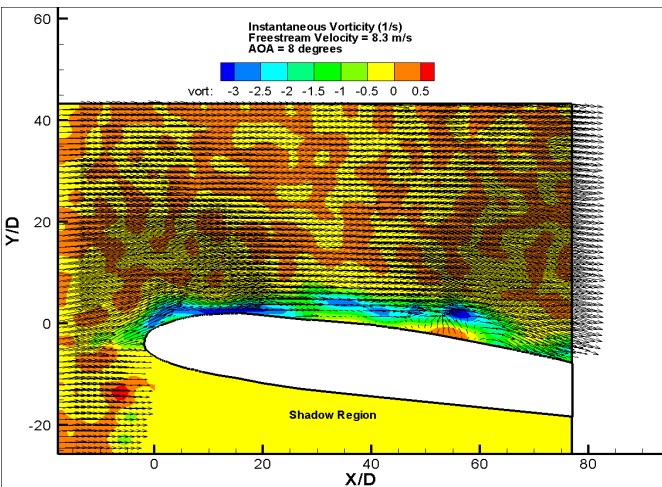
Wrapped dragonfly, AOA = 8 degrees
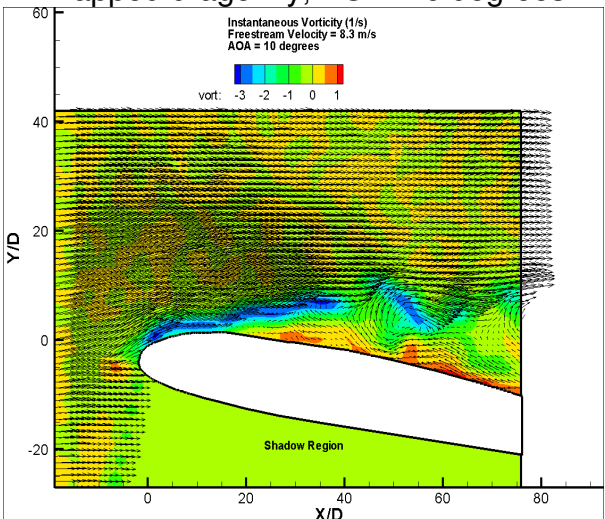
Wrapped dragonfly, AOA = 10 degrees
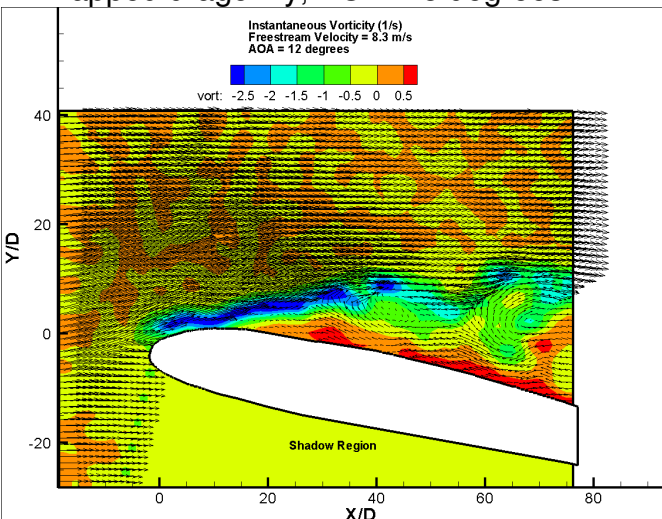
Wrapped dragonfly, AOA = 12 degrees
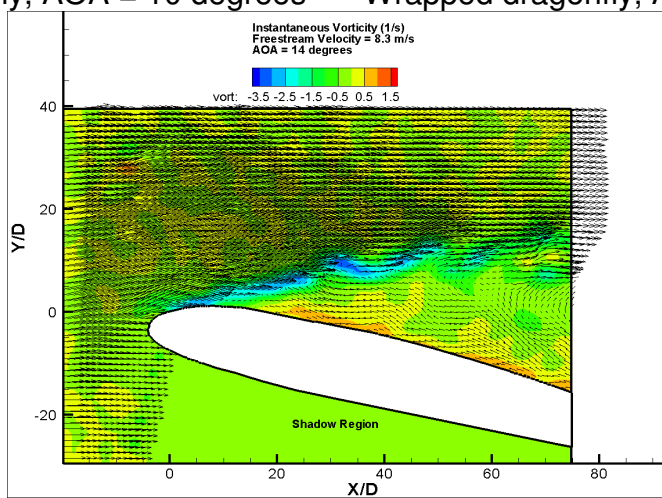
Wrapped dragonfly, AOA = 14 degrees

Figure 69. Instantaneous velocity vectors and spanwise vorticity distribution over upper surface of the wrapped dragonfly airfoil.

Wrapped dragonfly, AOA = 6 degrees

Wrapped dragonfly, AOA = 8 degrees

Wrapped dragonfly, AOA = 10 degrees

Wrapped dragonfly, AOA = 12 degrees

Wrapped dragonfly, AOA = 14 degrees
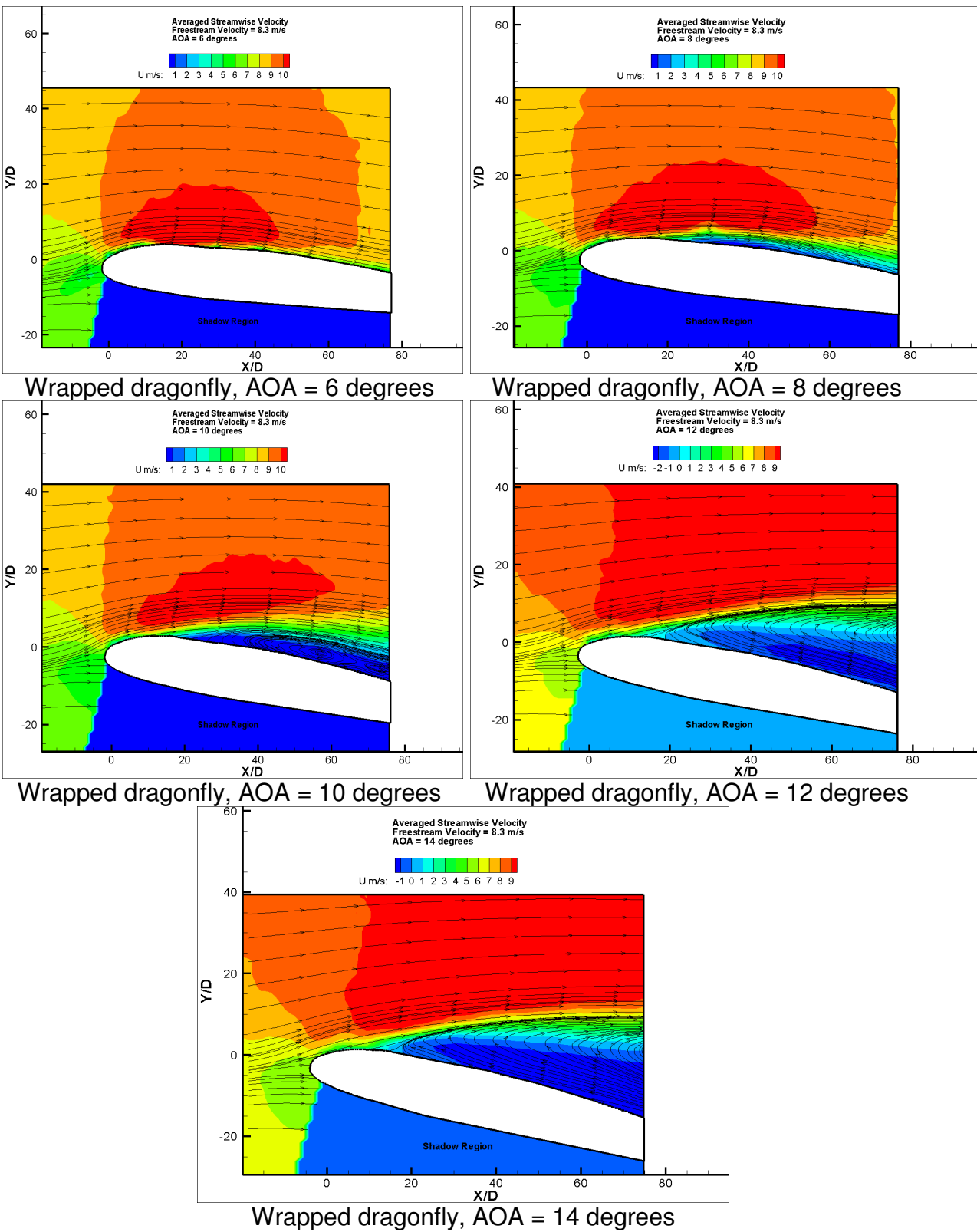
Figure 70. Ensemble-averaged streamlines over the upper surface of the wrapped dragonfly airfoil.

Dragonfly, AOA = 6 degrees

Dragonfly, AOA = 8 degrees

Dragonfly, AOA = 10 degrees

Dragonfly, AOA = 12 degrees

Dragonfly, AOA = 14 degrees
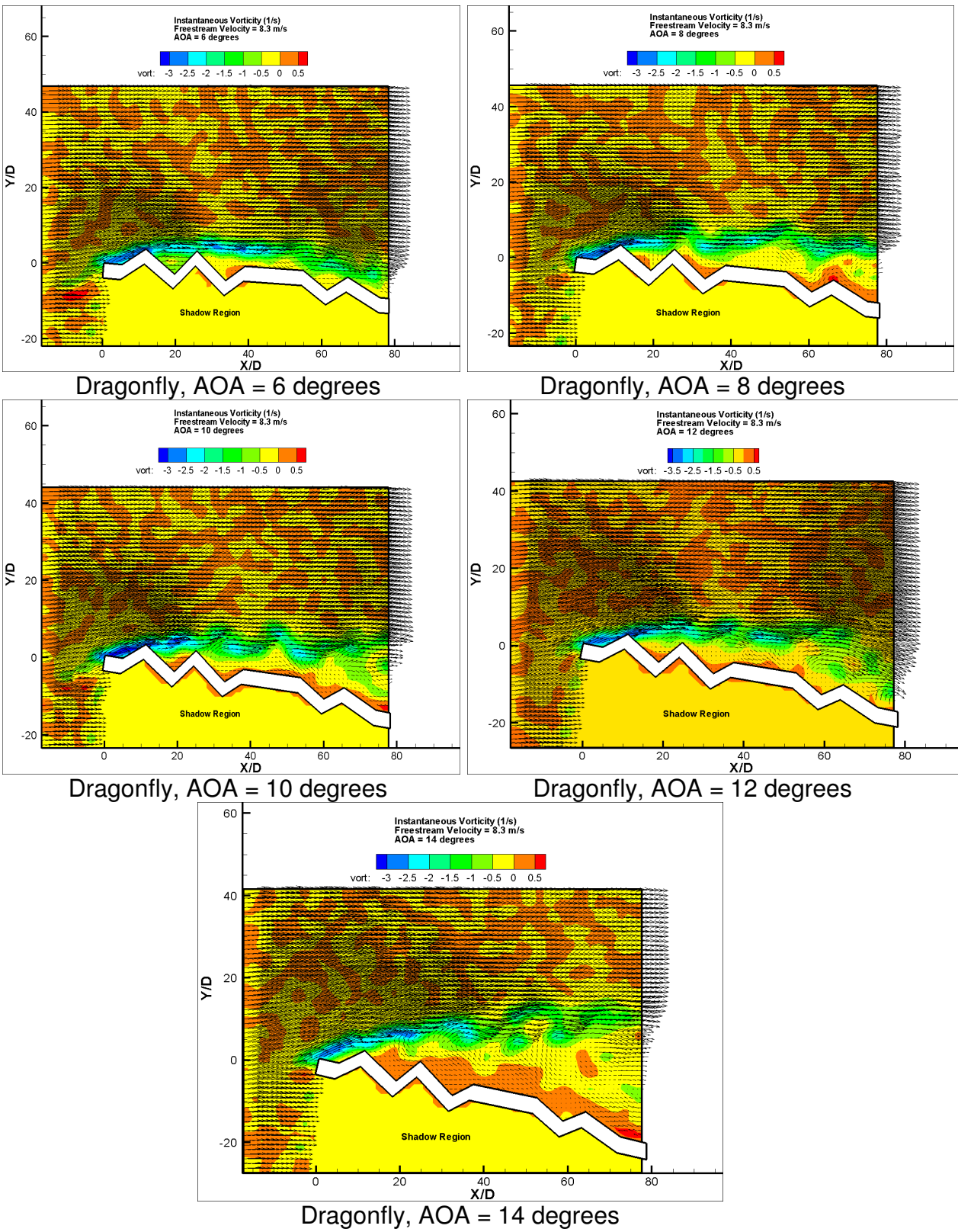
Figure 71. Instantaneous velocity vectors and spanwise vorticity distribution over upper surface of the dragonfly airfoil.

Dragonfly, AOA = 6 degrees

Dragonfly, AOA = 8 degrees

Dragonfly, AOA = 10 degrees

Dragonfly, AOA = 12 degrees

Dragonfly, AOA = 14 degrees
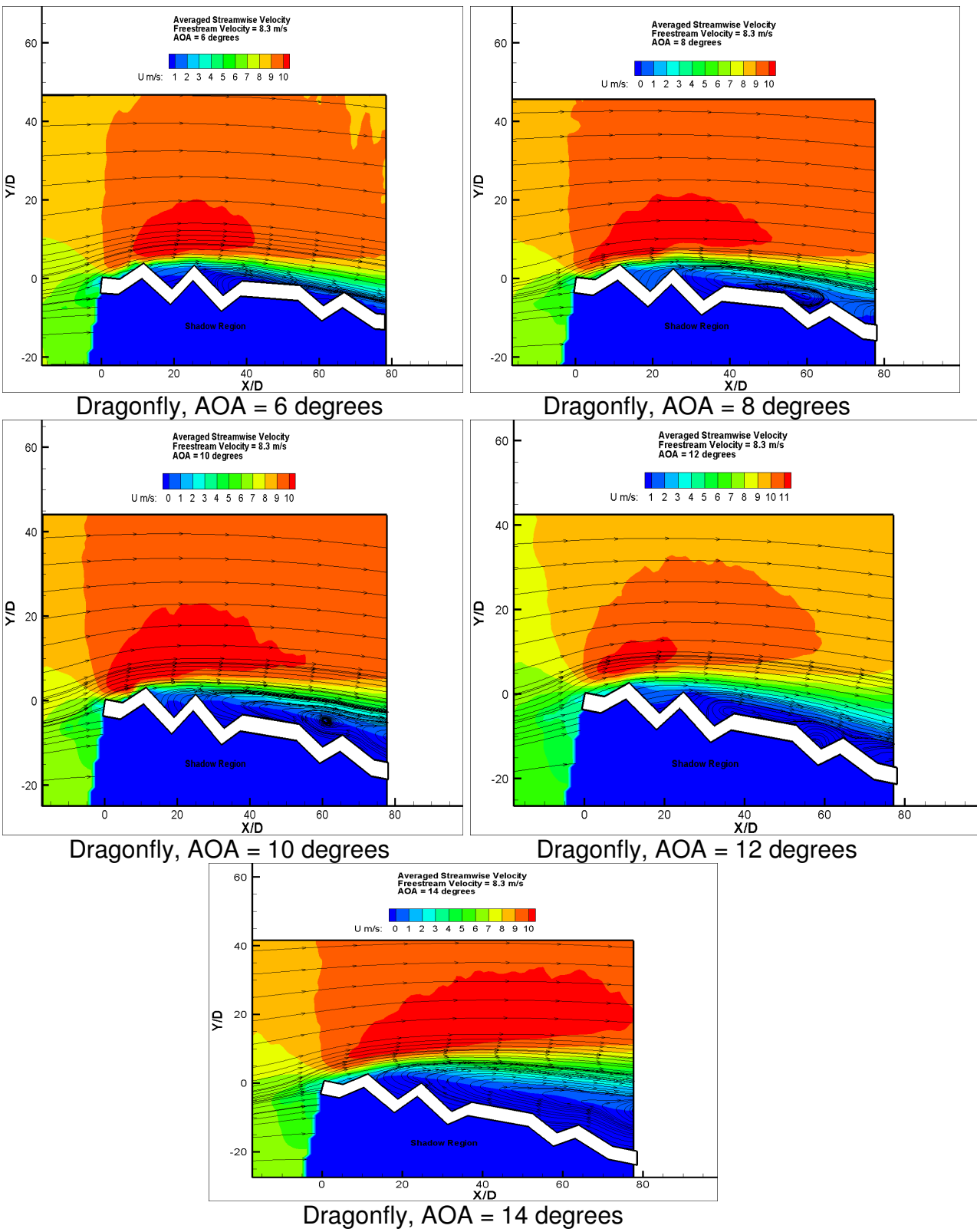
Figure 72. Ensemble-averaged streamlines over the upper surface of the dragonfly airfoil.

Figures 67 and 68 show the results for the flat plate. The spatial resolution of this measurement window does not provide any real insight into the flow not already observed in the previous measurement windows. Although the results do not show any new phenomena, they do verify and serve as supporting evidence to earlier findings. A separation bubble of about 50% of the chord length is present at 6 degrees AOA, and at 8 degrees and higher AOA the separation region shows the flat plate to be stalled.

Figures 69 and 70 offer another look at the flow on the upper surface of the wrapped dragonfly airfoil. The ensemble-averaged streamlines again show the existence of the separation bubbles at 8 and 10 degrees AOA. The instantaneous results further support the notion of the boundary layer separation and transition due to instabilities in the separated flow, as well as the increasing separation of the boundary layer from the surface with increasing angle of attack.

The results of the corrugated dragonfly airfoil shown in Figures 71 and 72 provide a better visualization of the boundary layer following the same smooth profile despite the strengthening adverse pressure gradient due to the increasing angle of attack. Also present in the measurement window is the recirculation region that was downstream in the more refined measurement window. In the case of 8 degrees AOA, the separation region appears to be filling the 'valley' created by the second and third peaks from the leading edge of the airfoil. As the angle of attack is increased the structure extends along the length of the airfoil until it is fully extended from the first to last peak and the boundary layer separates resulting in the stall of the airfoil.

2.4. Conclusion

The results from an experiment conducted consisting of three test airfoils: a flat plate, smooth profile (i.e., wrapped dragonfly) airfoil, and a corrugated dragonfly airfoil; tested in the chord Reynolds regime from $Re_c = 58,000$ to $Re_c = 124,000$ for the angle of attack range from 0 to 20 degrees have been presented in detail. The results from the present experiment as well as past studies provide ample evidence of the advantages of an airfoil with corrugations such as that of a dragonfly in low Reynolds number flows. Comparing the force measurements from the airfoils with varying Reynolds number showed that the performance of the corrugated dragonfly airfoil was better than that of the flat plate and wrapped dragonfly airfoil for Reynolds number approximately 1.0×10^5 or lower by delaying the stall of the airfoil to a higher angle of attack. The culmination of the force measurements and the PIV measurements taken showed that the corrugated dragonfly airfoil could delay stall until after 12 degrees whereas both other test airfoils were already experiencing full airfoil stall.

These results, while important, are not particularly useful. The underlying goal of the research was to learn and understand how and why the corrugation holds an advantage over the smooth airfoil. The key to designing better airfoils for MAV applications is to know how to exploit the advantages of the corrugation and knowing its limitations. The PIV measurements show how the corrugation of the airfoil surpasses the smooth airfoil. The corrugation peaks act as a boundary layer trip to transition the laminar boundary layer into turbulence while remaining 'attached' to the envelope profile of the high speed streamlines. The valleys promote clockwise vortex structures that help the boundary layer stay 'attached' by pulling high speed flow into near wall regions. It is by these two processes that the

corrugated airfoil can overcome the adverse pressure gradient and thus delay stall, in turn increasing the performance of the airfoil.

The PIV measurements for this study were conducted only for the chord Reynolds number $Re_c = 58,000$. However, very similar results were found in the work by Tamai [12] at the chord Reynolds number $Re_c = 34,000$. The study by Tamai showed the existence and strong presence of the valley vortex structures in the corrugated airfoil from 5.0 to 10.0 degrees AOA. At 12.5 degrees AOA, the vortex structures have been pushed down into the valleys by the recirculation region over the latter half of the airfoil at the very onset of the airfoil stall; similar to the results for the 8 degree AOA case shown in Figure 64 of the present work. In the 15.0 degrees AOA case in the study by Tamai, the airfoil is completely stalled and the valleys of the corrugation show vortex structures of the opposite sense; much like the results of the present study. It is this author's belief that as the Reynolds number becomes lower, the viscous forces of the flow are of greater influence than the inertial effects, and thus the vortex structures in the valleys will sustain themselves at higher angles of attack when compared with higher Reynolds number flows. The consequence of this is that as the Reynolds number increases to a certain limit, the valleys no longer possess the vortex structures and the airfoil performs more like a traditional smooth airfoil would – as is evidenced by the force measurements of this study. It is with this understanding of the flow physics associated with corrugated airfoils that design solutions might be optimized, producing a high performance airfoil for MAV applications in the Reynolds regime of MAVs rather than scaling down airfoils optimized for macro type vehicles.

Chapter 3. Study of Flapping Wing Configuration

3.1. Introduction to Flapping Flight

Flapping wings is the technique employed by all natural flyers to achieve their flight (the author does not consider animals such as flying squirrels or flying snakes that glide to be natural fliers as they cannot produce lift with which to achieve significant climb). Through history, man has always dreamed and attempted to fly like birds – most all in failure. Then, slightly over 100 years ago, manned flight was achieved; however not by flapping wings, but rather using a fixed wing pushed or pulled through the air by a propeller. With the success of the fixed wing, the development of flapping winged vehicles was pushed aside and deemed impractical.

The underlying cause for the failure of manned ornithopters (flapping wing vehicles) is essentially inadequate materials for the demanding structural requirements. In order for manned ornithopters to experience similar wing loading compared to that of a bird, the wing area must be vastly increased due to the increased payload. However, this problem is not easily solved by just increasing the wing area. For increasing the wing area also increases the weight of the vehicle requiring again more wing area. At the scale of manned ornithopters, no material possessed an adequate strength to weight ratio to achieve a configuration that was light enough and strong enough to produce and withstand the required loads associated with flapping flight.

MAVs however, are not of the scale of manned ornithopters. Along with new light weight composites that have developed in recent years with significant improvement in strength to weight ratio, flapping wing configurations have not only become feasible but

thanks to several toy companies a reality (i.e., the WowWee Flytech Dragonfly shown below

in Figure 73). Among the potential advantages of flapping flight are increased maneuvering,

the capability to hover or loiter, and increased aerodynamic efficiency. The intent of the

present study is to increase our understanding of the physics associated with flapping wing

flight through force measurements subjected to several adjusted parameters. To be armed

with the fundamental basis of the technique allows the improvement of wing designs, motor

design requirements, and the ability to produce reliable and viable MAVs that exploit this

most natural method of flight.

Figure 73. WowWee Flytech Dragonfly remote controlled ornithopter.

Due to the potential application to MAVs, flapping wing configurations has once

more become a driving research topic in the aeronautic/aerodynamic community within the

last few years. Some notable such studies are Kim et al [16] which investigates a smart

flapping wing that uses a piezoelectric mechanism to control wing camber through total

aerodynamic force measurement. The study conducted by Ho et al [17] compares flapping

wings of different flexibility by direct force measurements. Several numerical studies have also been conducted to explore flapping flight, including work by Shyy et al [18] which presents some results for 2-D as well as 3-D simulations; and Pederazani et al [19] showing results for a 2-D heaving flexible airfoil in a viscous flow. Additional resources for flapping flight studies can be found listed in the Reference section on page 87.

The current study is a very preliminary beginning to future work to be researched in the complex topic of flapping flight. The results presented in this thesis consist of total aerodynamic force measurements for a wing configuration model in which only the wing beat (flapping frequency), body orientation, and incoming flow velocity is controlled. The model does exhibit passive wing pitching by means of flexibility through the deformation of the wing structure; but the wing skin is essentially non-flexible. It is noted that birds, bats, and insects employ many other mechanisms during locomotion such as tension control of the wing skin in bats and leading edge feather tufts in birds as well as complicated wing kinematics similar to rowing as well as moveable joints. The present studied has been simplified in order to explore and gain understanding of a very basic level of flapping flight physics.

3.2. Experimental Setup for Flapping Wing Configuration Experiment

The experiments for the flapping wing configuration were conducted using a currently existing remote controlled ornithopter model. The model is a Cybird P1 manufactured by NEUROS Co. in Korea. The flapping mechanism uses a Scottish yoke gear mechanism to drive the wings from a rotary electric motor. The gearbox and motor are shown in Figure 74 below.
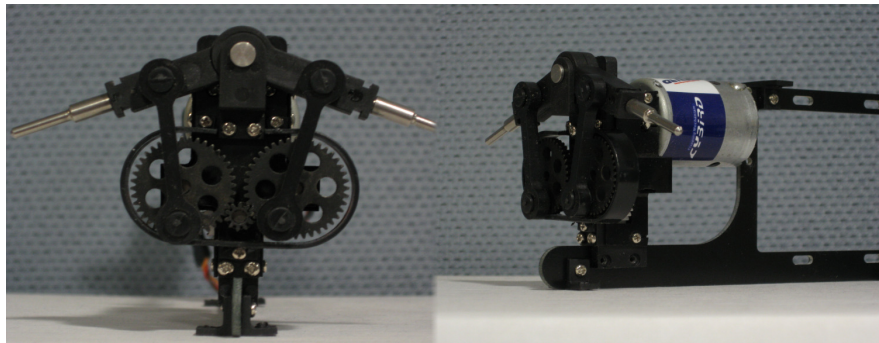
Figure 74. Cybird P1 gearbox and motor.

In order for the experiments to be conducted, a custom metal bracket was designed to bolt onto the Cybird frame. Airfoil shaped tubing was then used to connect the bracket to the mount for the JR3. Figure 75 depicts a side view and top view of the Cybird shown on page 65. The top view provides the location of the chord length used in the calculation for the chord Reynolds number. The experimental setup for the wind tunnel test is also shown on the following page in Figure 76. During the experiments, the Cybird was powered by a BK Precision 1760A DC power supply.
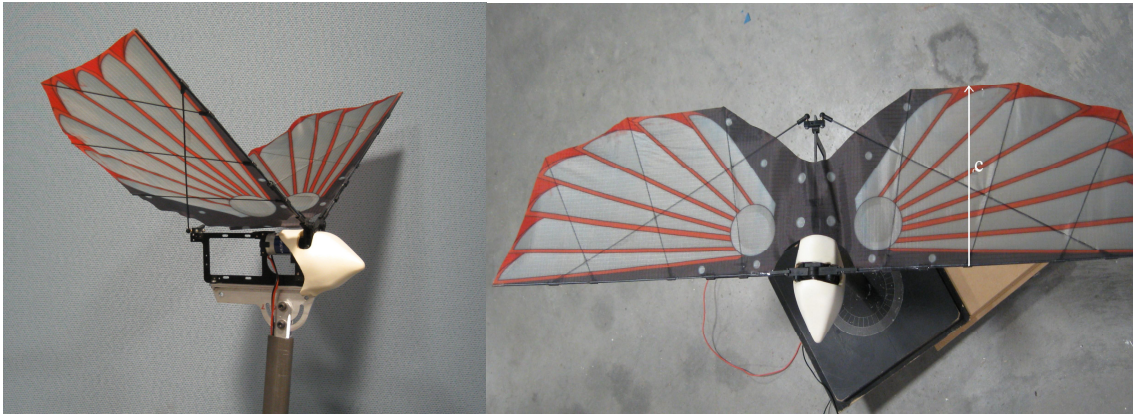
Figure 75. Cybird P1 side and top views.
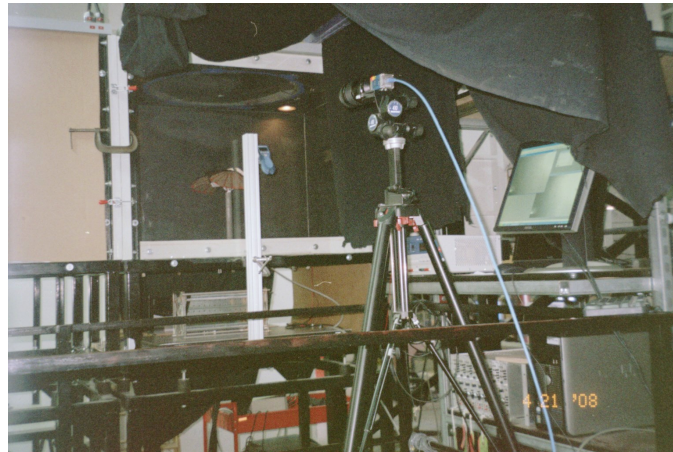
Figure 76. Experimental rig and setup for flapping wing configuration experiments.

The setup for the JR3 in the current experiment is the same as for the corrugated dragonfly airfoil experiment with the exception that the model is supported from below rather than from the side. In this orientation the lift (force normal to the incoming flow) is along the z-axis of the JR3; and the drag (force tangential to the incoming flow) is oriented along the x-axis of the JR3. As in the dragonfly airfoil experiment, the mean values and time series were recorded for 15,000 samples at a sampling rate of 500 Hz.

The vibration of the rig introduced a great deal of noise into the system, therefore a Matlab program was written to analyze the time series of the lift forces using FFT in order to find the wing beat frequency. A sample time series plot and the corresponding frequency

identified through the code are presented below in Figure 77.
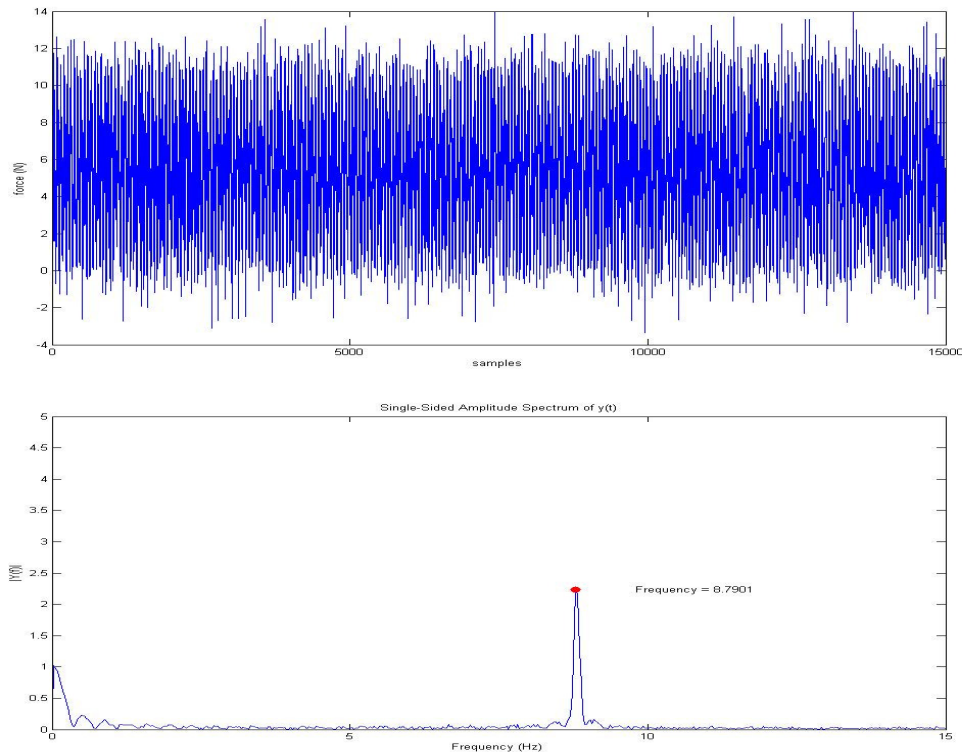
Figure 77. Time series and wing beat frequency for 5 degrees AOA static case.

The tests were conducted in the Bill James Wind Tunnel located in the WiST

Laboratory of the Aerospace Engineering Department at Iowa State University. The wind

tunnel is an open loop tunnel with a 91.5 cm x 76 cm (3 ft x 2.5 ft) test section. The tunnel is

equipped with multiple layers of screens at the inlet to promote laminar, low turbulent flow

in test section. The quality of the flow in the test section was tested by measuring the

turbulence intensity profile of the cross section at the test Reynolds numbers as well as a

velocity profile of a center point of the test section using the Dantec Dynamics MiniCTA

described in the experimental setup section of the corrugated dragonfly airfoil experiment

(**2.2**). A calibration curve for the wind tunnel is provided in Figure 78 followed by Figure 80

which shows the velocity profile of the test section for V = 4.12 m/s. The results of the

turbulence intensity tests are shown below in Figures 80-83. The turbulence intensity does not exceed 1% for the velocities used in the test with the exception of one point in both the 4.12 m/s and 6.05 m/s cross section profiles. The turbulence intensity at these points is believed to be due vortex shedding from a pitot-static tube just upstream of the test section.
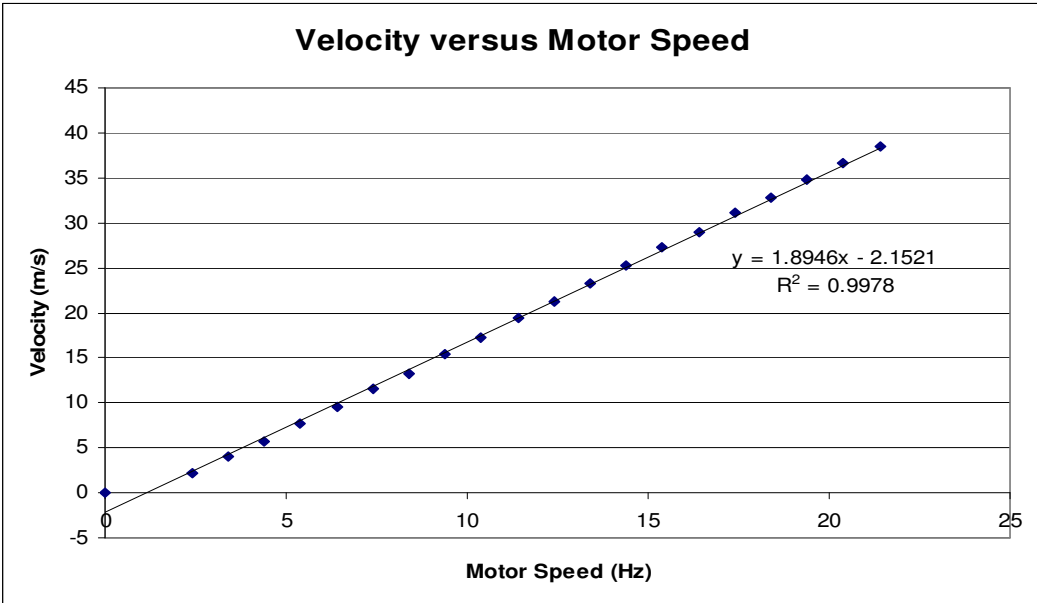
Figure 78. Calibration curve for Bill James wind tunnel.
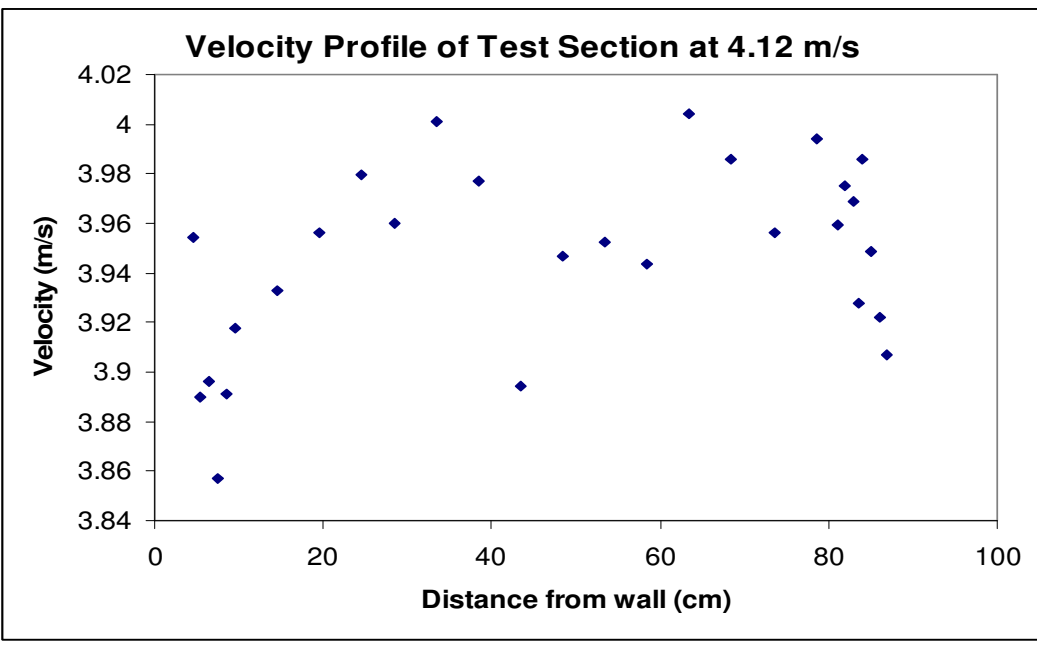
Figure 79. Horizontal velocity profile of test section for V = 4.12 m/s.

Velocity vs Turbulence Intensity
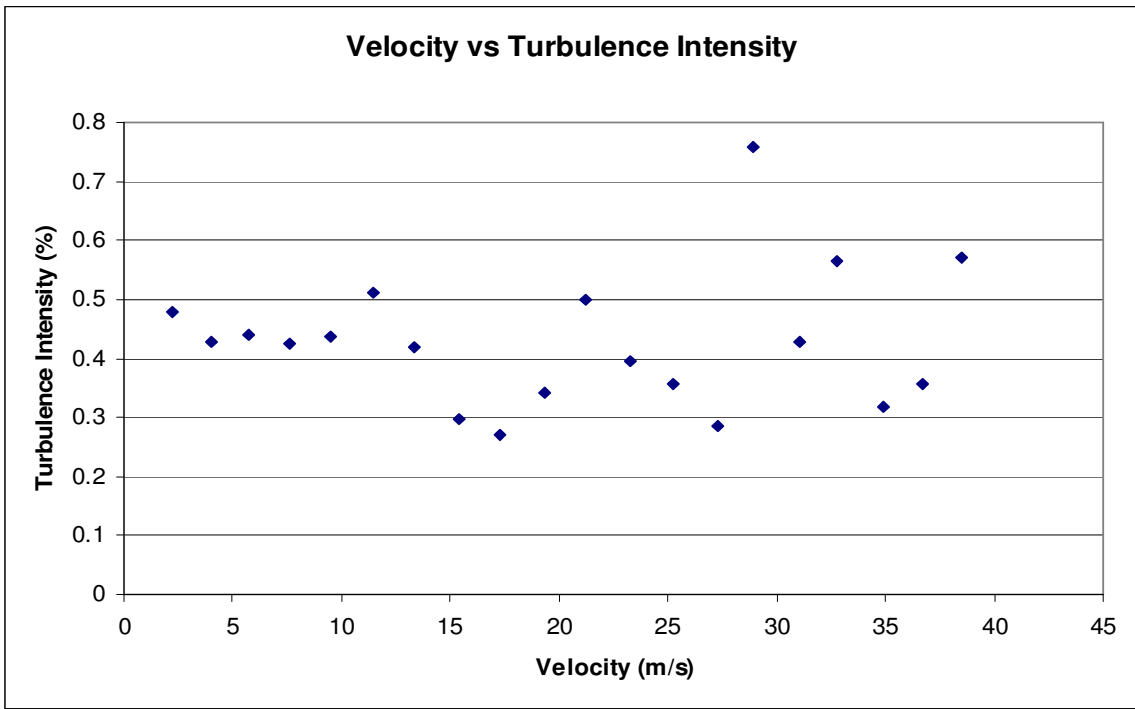
Figure 80. Velocity profile of turbulence intensity for the Bill James Wind Tunnel used in the current experiment.

Turbulence Intensity Cross Section Profile for V = 4.12 m/s
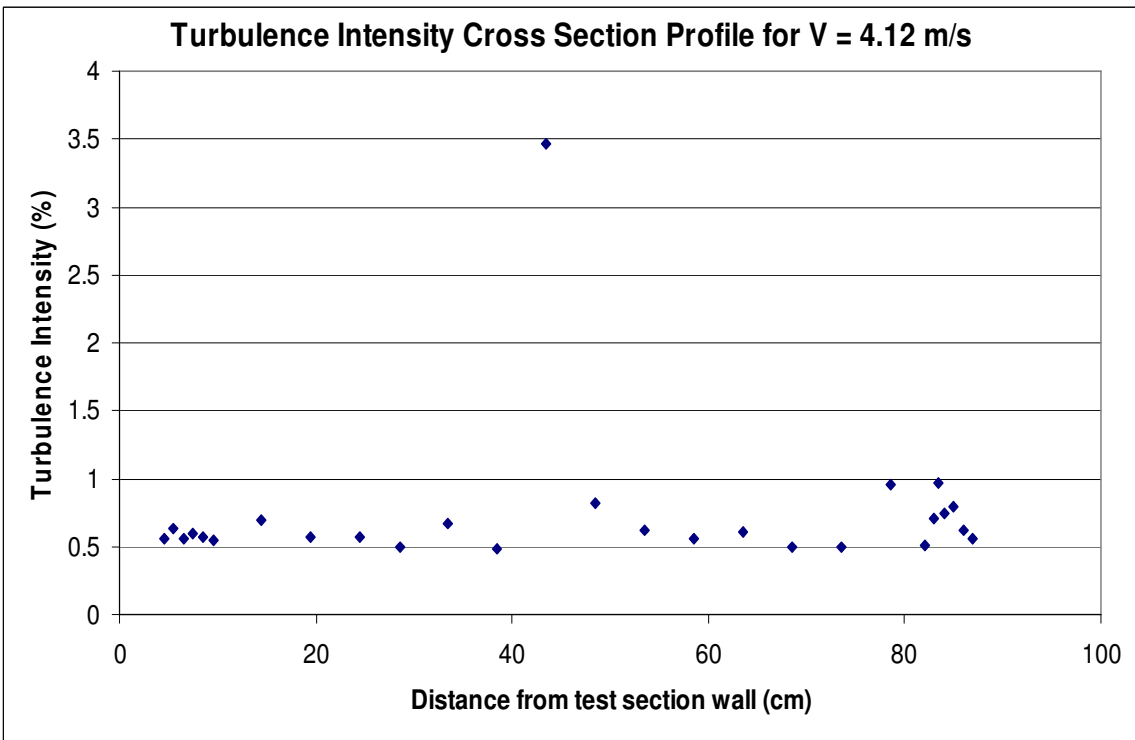
Figure 81. Cross section turbulence intensity profile for V = 4.12 m/s.
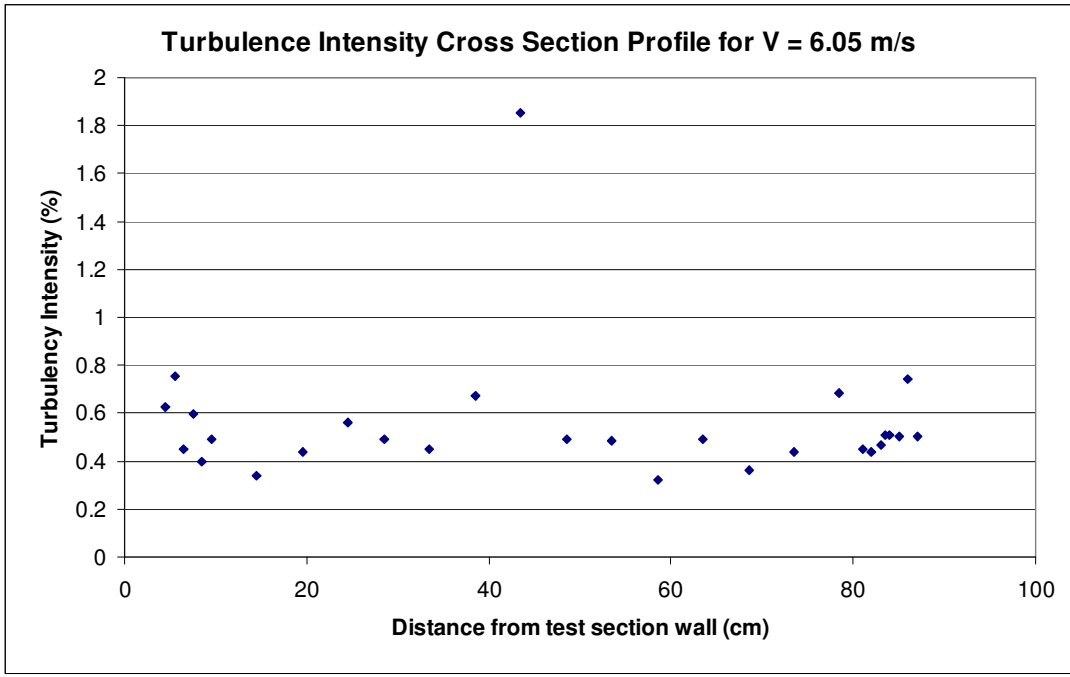
Figure 82. Cross section turbulence intensity profile for V = 6.05 m/s.
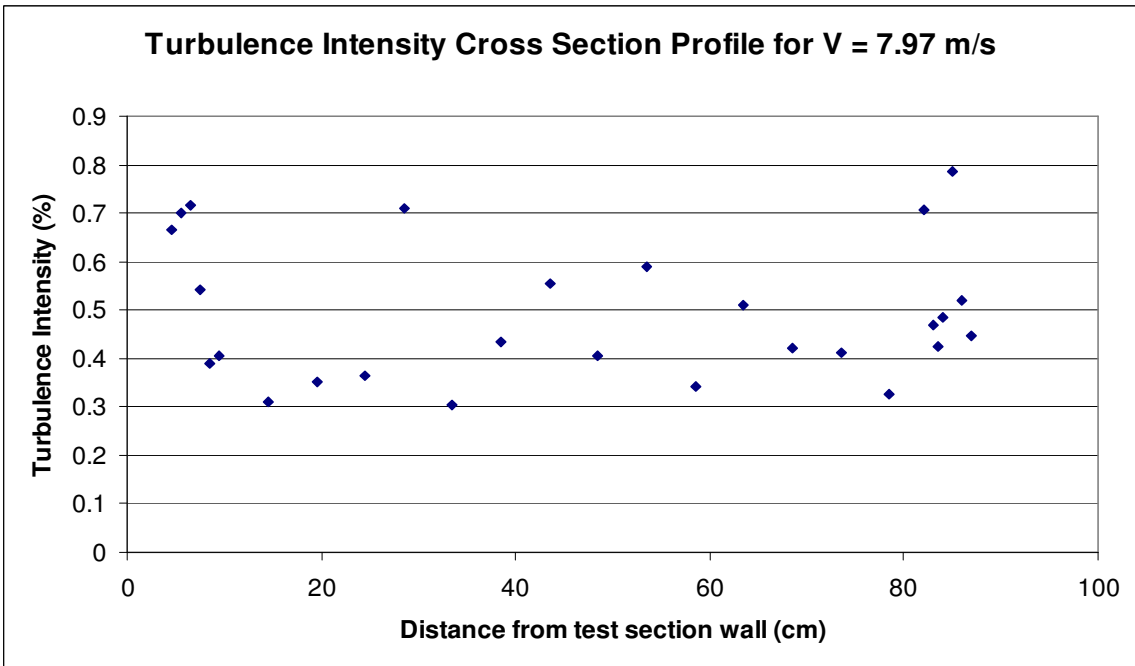
Figure 83. Cross section turbulence intensity profile for V = 7.97m/s.

3.3. Results and Discussion

3.3.1. Static and Dynamic Force Measurement Results

The total aerodynamic force was measured for the flapping wing configuration from -5 to 15 degrees angle of attack in increments of five degrees at four chord Reynolds numbers: $Re_c = 0$; $Re_c = 50,000$; $Re_c = 74,000$; and $Re_c = 98,000$. The chord Reynolds case corresponding to $Re_c = 0$ is considered to be the static case (i.e., there is no incoming freestream velocity). The remaining Reynolds numbers correspond to incoming flow velocities: 4.12, 6.05, and 7.97 m/s respectively. The measurements are the mean values from 15,000 samples acquired at 500 Hz. Each measurement was taken nine times and the results are the average values of these nine trials.

The applied voltage supplied to the motor was a constant 7.0 volts, it should be noted however that the wing beat frequency was not constant. The only control for adjusting the wing beat frequency was the DC voltage applied to the Cybird motor; however different loading conditions on the motor affected the wing beat frequency (i.e., each time the angle of attack or flow velocity was changed, the wing beat frequency was altered). Table 1 below shows how the flapping frequency changed with angle of attack and incoming flow velocity.

Applied Voltage 7.0 Volts		AOA				
		-5	0	5	10	15
m/s	0	8.48	8.45	8.79	8.52	8.42
	4.12	9.03	8.82	9.25	8.85	8.85
	6.05	9.19	9.03	9.28	9.10	9.06
	7.97	9.61	9.19	9.31	9.13	8.98

Table 1. Wing beat frequency changing with angle of attack and incoming flow velocity.

Trends shown in Table 1 show that as the incoming flow velocity increases, the flapping frequency also increases slightly – with the exception of one case for 15 degrees

AOA and 7.97 m/s incoming velocity in which it is believed the motor was overloaded and hence bogged down by the aerodynamic loading. The same feature of motor 'overloading' is also evident by the changing angle of attack, the flapping frequency increases as the AOA moves away from 0 degrees; however for the 10 and 15 degree cases, the wing is aligned increasingly parallel to the incoming flow and thus creates a large aerodynamic force opposing the motor (this is the same force responsible for the creation of lift at higher angles of attack). For the results presented in this section, the wing beat frequency is considered the average value of the frequencies for all cases. The wing beat frequency average of Table 1 is $\varphi = 8.97$ beats per second with standard deviation 0.32. The effects of varying frequency are discussed in the next section. The forces due to the inertial effects of the flapping wings was considered negligible as a direct result of assuming a symmetric pattern; the forces should theoretical cancel one another from the up and down strokes.

The results can be manipulated in several ways, each bringing an insightful look into the aerodynamic forces and how they relate to one another and each variable. Figure 84 shows the averaged mean lift forces measured by the JR3 in Newtons, and the effects of the increasing chord Reynolds number. It can be easily deduced from Figure 84 that as the chord Reynolds number increases, the lifting force also increases. Not surprisingly, the lifting force also increases with increasing angle of attack as a component of the thrust generated by the flapping motion is directed normal to the incoming flow direction. An interesting feature of the force measurements is the shifted lift curve for the $Re_c = 98,000$ case. This upward shift can be explained by the increase in Reynolds number, or more specifically the advance ratio described below.
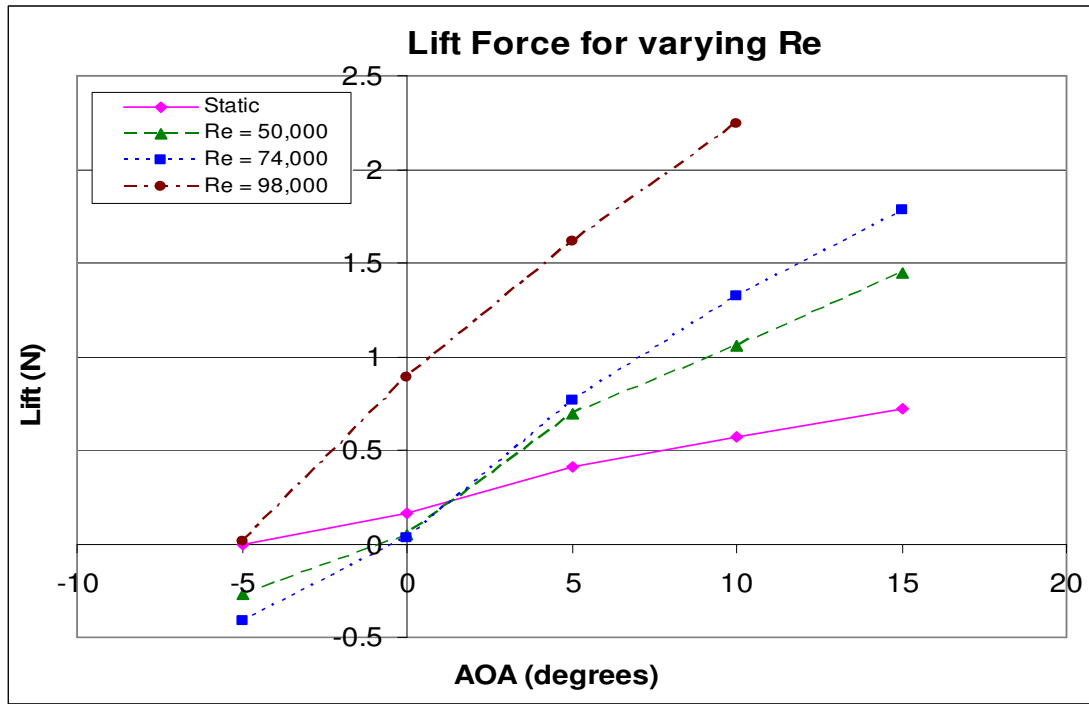
Figure 84. Lift force for varying Re_c at wing beat frequency $\varphi = 8.97$.

The advance ratio is a ratio of the incoming flow velocity to the velocity of the wing

tip, and is expressed in the following equation,

$$J = V/2*F*b*\theta$$
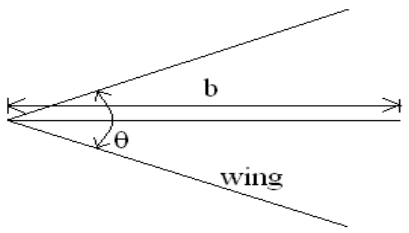
Figure 85. Angle θ and length b used in calculation of advance ratio.

V is the velocity of the incoming flow; F represents the wing beat frequency; b is the semi-

span of the wings; and θ is the amplitude of the angle of the wing flapping [16]. If this ratio

is greater than one, then the flapping wings will exhibit quasi-steady behavior. For advance

ratios less than one, the flapping wings are subject to unsteady behavior. If the flow is within

the quasi-steady region, the lift will react much like the static case as shown in Figure 84 for

the Re_c cases of 50,000 and 74,000 with corresponding advance ratios J = 0.66 and J = 0.96

respectively. In contrast, the advance ratio for the case Re_c = 98,000 is J = 1.27. The

direction from which the unsteady lift approaches the quasi-steady region is dependent upon

the spanwise flexibility of the wing as shown in Figure 86; the Cybird wing exhibits

spanwise rigidity and will therefore show this behavior in the lift coefficient presented in

Figure 89. Figure 86 also demonstrates the transitioning behavior of the lift coefficient as the

advance ratio passes through J = 1; for J > 1 the lift exhibits a constant quasi-steady quality,

but as the advance ratio decreases below J = 1 the lift coefficient increases exponentially.
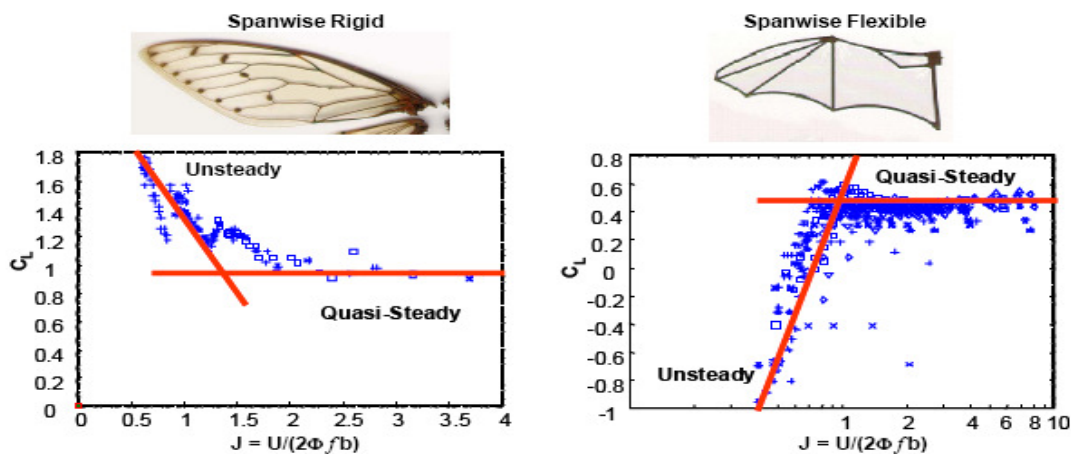
Figure 86. Advance ratio flow regimes for spanwise rigid and flexible wings [17].

Although there is insignificant data (shown in Figure 87) in which to define the exponential

curve of the advance ratio as the flow transitions from the unsteady to the quasi-steady

regime, it is evident that the data does directly correlate to this type of fit. Furthermore, upon

inspection of the lift coefficient (Figure 89), we see that the lift coefficients for the 5 and 10

degree AOA in the Re_c = 98,000 case lie in the quasi-steady region in Figure 87.
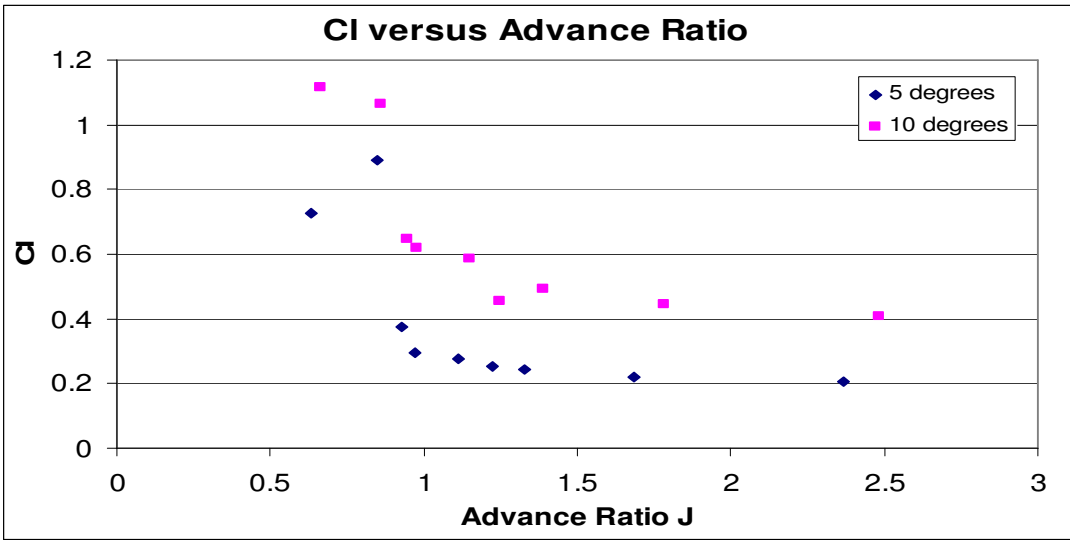
Figure 87. Coefficient of lift versus the advance ratio for the current study.

Figure 88 shows the averaged mean thrust force in Newtons for the flapping wing

configuration as measured by the JR3 for varying chord Reynolds number.
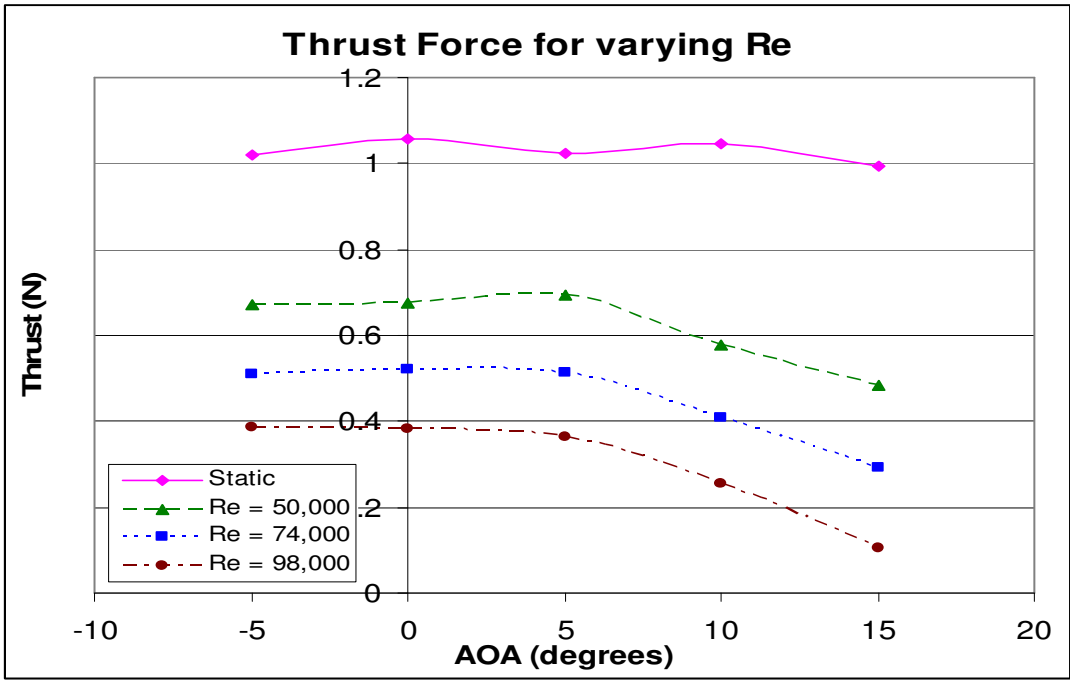
Figure 88. Thrust force for varying Re_c at wing beat frequency $\varphi = 8.97$

The results shown in Figure 88 are rather intuitive. As the freestream velocity

increases, the thrust in the wake of the flapping wings is reduced relative to the surrounding

flow. It is noted that there is no dramatic change in the static thrust case for increasing angle of attack; suggesting that the probable cause for the deteriorating thrust production with increasing angle of attack is due to an increased drag force acting on the wings. Also, as discussed earlier as a result of the lift force increasing with increasing angle of attack, the thrust is reduced as the angle of attack increases as the component of the thrust becomes more aligned perpendicular to the incoming flow.

A more typical plot of performance is lift and drag coefficient; or in the case of flapping wings the coefficient of thrust. The lift force was instrumental in showing the transition from unsteady to quasi-steady flow; however, as the plot of the lift coefficient in Figure 89 shows that the lift generated in the quasi-steady region is less efficient than that of the unsteady regime.
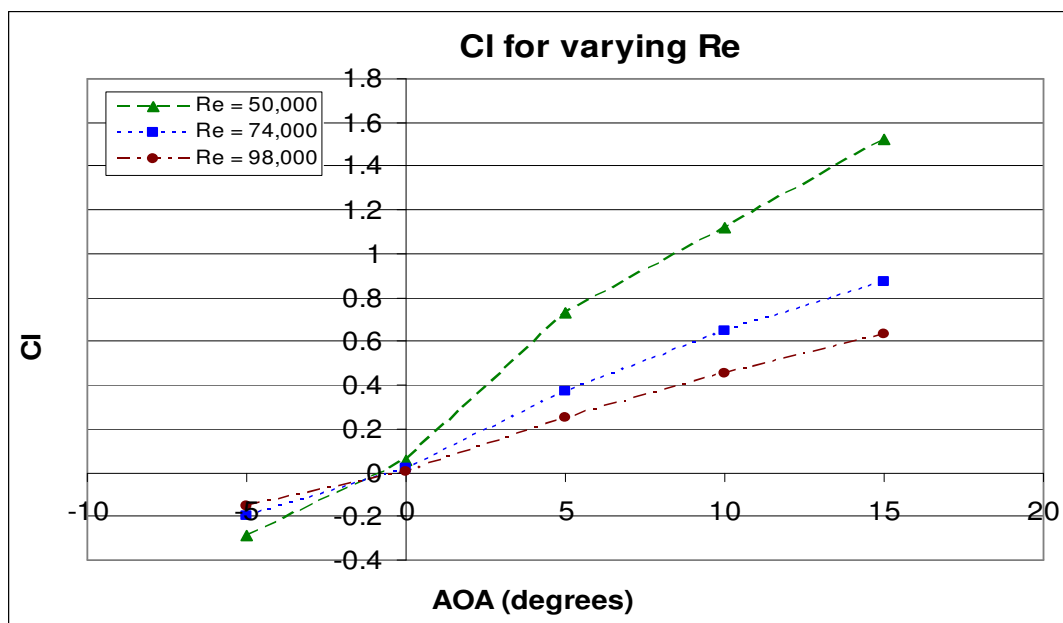
Figure 89. Lift coefficient for varying Re_c at wing beat frequency $\varphi = 8.97$.

The results in Figure 89 illustrate that the coefficient of lift is actually greatest for the chord Reynolds number case $Re_c = 50{,}000$. This should be expected from a wing with spanwise

rigidity; Figures 86 and 87 show that a lower advance ratio yields a higher coefficient of lift for spanwise rigid wings. The advance ratio for the case of Re_c = 74,000 is J = 0.96, making the results for this chord Reynolds number behave more closely like the quasi-steady case Re_c = 98,000.

The coefficient of thrust is shown for varying chord Reynolds number in Figure 90. The trend for the thrust coefficient is very similar to that of thrust force shown in Figure 88 shown on page 74. The results simply show that the thrust coefficient decreases with increasing chord Reynolds number as well as increasing angle of attack. Again the advance ratio serves to explain the shift in the Reynolds number Re_c = 50,000 case. Because the advance ratio for the case Re_c = 74,000 is nearly unity (J = 0.966), the thrust coefficient behaves much like that of the quasi-steady, higher Reynolds number counterpart; as in the lift coefficient.
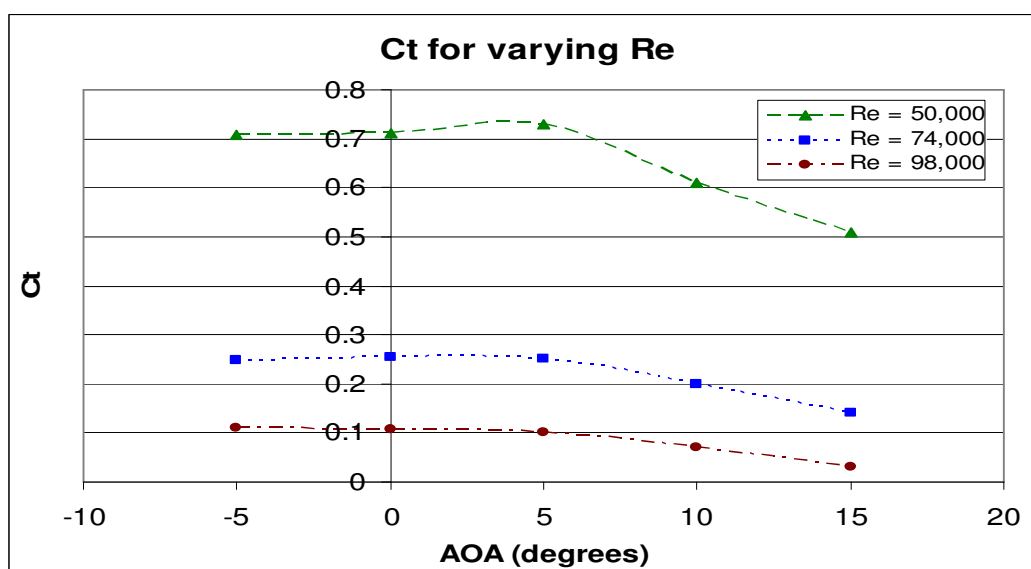
Figure 90. Thrust coefficient for varying Re_c at wing beat frequency φ = 8.97.

Figures 91 and 92 serve to show how the velocity is related to the averaged mean lift and thrust forces when plotted directly against one another. Figure 91 demonstrates the

linear relation between the lift force and the incoming freestream velocity. The plot also

reveals what is already known from the previous Figures 84 and 89 that the lift increases with

increasing angle of attack.
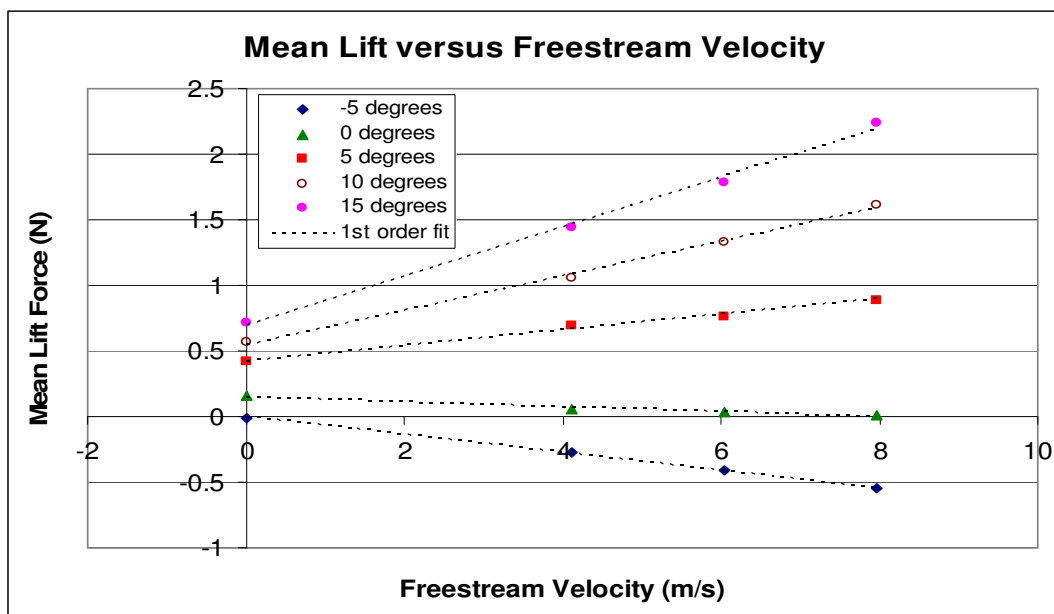
Figure 91. Mean lift force versus freestream velocity for various angles of attack.

Figure 91 also shows that lift and its sense are determined by the angle of attack. For

negative angles of attack, negative lift will be produced; very little lift is produced at 0

degrees angle of attack and remains fairly constant for increasing incoming flow velocity;

and positive angle of attack will produce positive lift, with higher angles yielding higher lift.
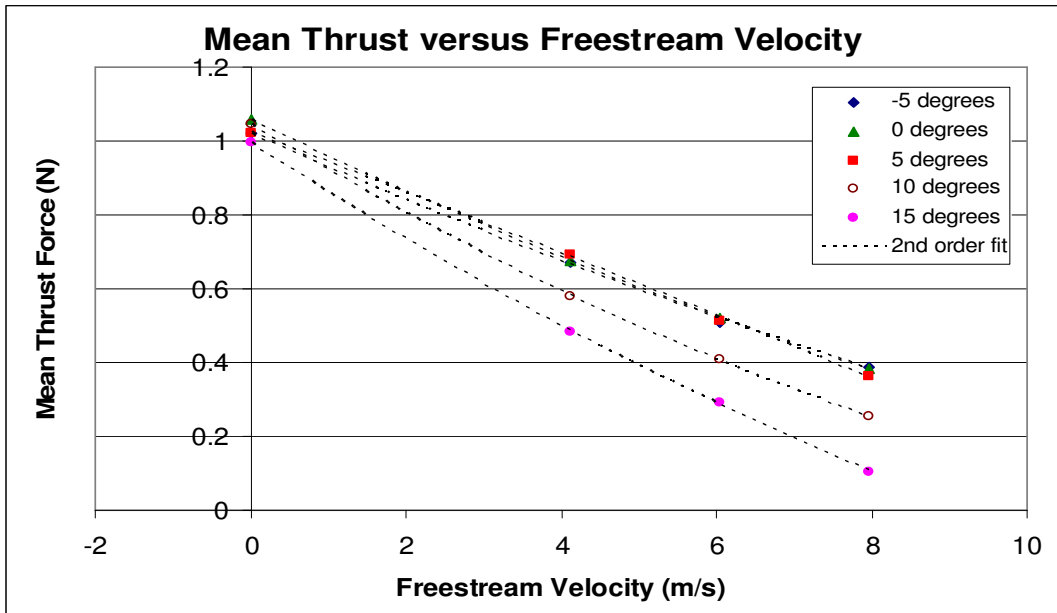
Figure 92. Mean thrust force versus freestream velocity for various angles of attack.

Figure 92 demonstrates the thrust fit by a second order curve to the incoming flow velocity. This rendering of the data shows an interesting feature in that the low angles of attack (i.e., -5 to 5 degrees) are virtually indistinguishable in thrust production. The figure also shows evidence for the reduction of thrust from increases in both incoming velocity and angle of attack.

3.3.2. Effects of Wing Beat Frequency

In this section the results of a study conducted to analyze the effects of wing beat frequency on the aerodynamic forces of the flapping wing configuration are presented. For this experiment, two angles of attack were selected 5 and 10 degrees as well as the incoming flow velocity of 6.05 m/s. The wing beat frequency was then varied by adjusting the voltage applied by the power supply to the Cybird motor. The voltage was increased in increments of 1.0 volt from 2.5 to 7.5 volts. The results from the earlier dynamic force study conducted at the applied voltage of 7.0 volts are also included. As in the previous experiment, 15,000 samples were acquired at a rate of 500 Hz.

One useful result from this study is shown in Figure 93. This figure shows a linear relationship between the wing beat frequency and corresponding applied voltage from the power supply. It is noted that the frequency does vary slightly for the 5 and 10 degree cases as alluded to in the previous section.
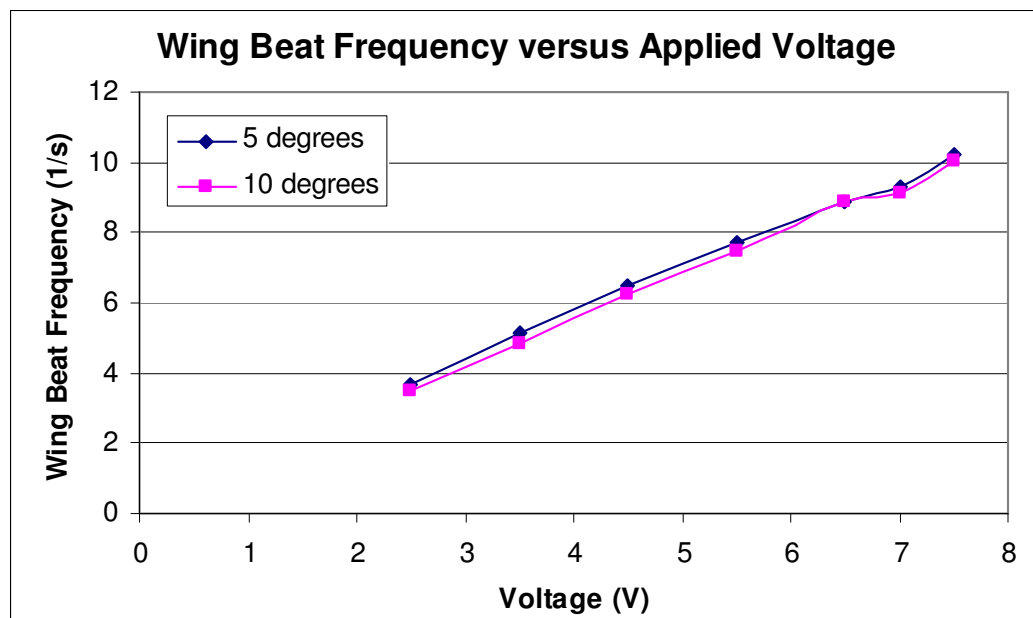
Figure 93. Wing beat frequency versus applied voltage for Cybird at 5 and 10 degrees AOA.
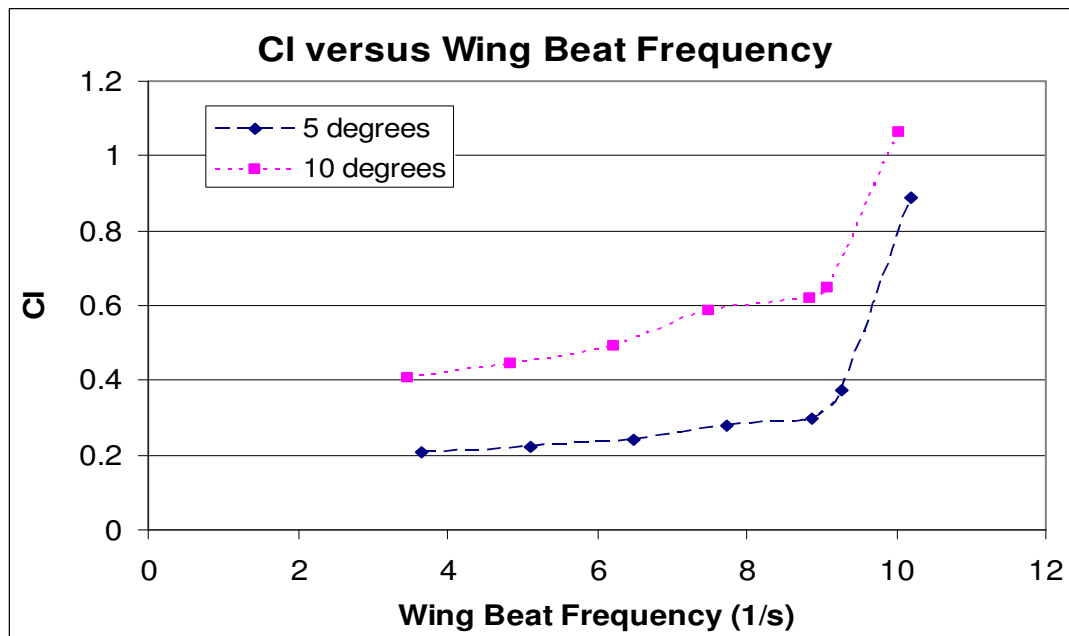
Figure 94. Coefficient of lift for varying wing beat frequency.

Figure 94, which shows the coefficient of lift versus the wing beat frequency is yet another good example of significance of the advance ratio. We see that as the flapping frequency of the mechanism increases, the lift coefficient is relatively constant through the quasi-steady region as the advance ratio approaches the value of 1; which corresponds to $\varphi =$ 8.604 for the current incoming velocity. After the flapping frequency crosses the J = 1 threshold the lift coefficient begins to increase exponentially in the unsteady region. This result is generalized to both angles of attack 5 and 10 degrees.

The obvious result for the thrust coefficient is shown in Figure 95 on the next page. It is very intuitive that as the flapping frequency increases, the thrust production will also increase. In the case of the thrust coefficient, the increase appears linear through the quasi-steady flow region and transitions into an exponential behavior similar to the lift coefficient in the unsteady region.
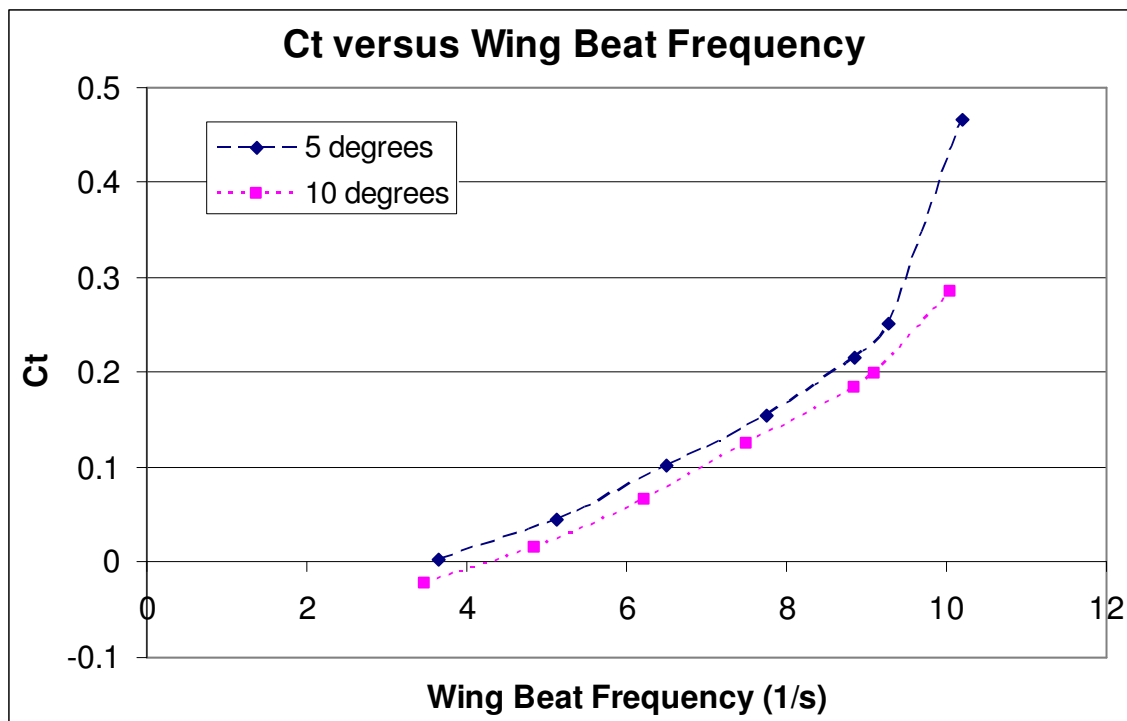
Figure 95. Coefficient of thrust for varying wing beat frequency.

3.3.2. Gliding Results for Flapping Wing Configuration

In this section, the results for the gliding flight of the flapping wing configuration are presented. This study is pertinent to MAVs as periods of gliding during flight can allow reduced power consumption for the vehicle and extend its endurance and range. Both structural and wing skin flexibility play an important role in the performance of the wings in gliding flight. Studies in wing skin flexibility, such as that by Tamai [12], have shown that flexible skin or membrane skin wings allow for incoming flow instabilities or gust suppression (referred to as adaptive washout in some literature [20]). This allows the wing to achieve stall delay by changing the effective angle of attack through passive camber deflection resulting from the aerodynamic loading on the wing. Structural flexibility on the other hand, reduces the effective angle of attack as well, except this mechanism simply changes the pitch of the chord. The result of structural flexibility is a decreased lift and drag coefficient for increasing chord Reynolds number.

For this study, the wings of the Cybird were set to be horizontal, parallel with the body y-axis. The same test chord Reynolds numbers as in the static and dynamic force measurements were investigated: $Re_c = 50,000$; $Re_c = 74,000$; and $Re_c = 98,000$. Consistent with the previous studies, 15,000 samples were acquired at 500 Hz.

The results for the lift coefficients are shown in Figure 96. It is noted that wing exhibits structural flexibility due to the decrease in lift coefficient with increasing chord Reynolds number. Also evident from Figure 96, is the onset of stall in the lower Reynolds number cases.
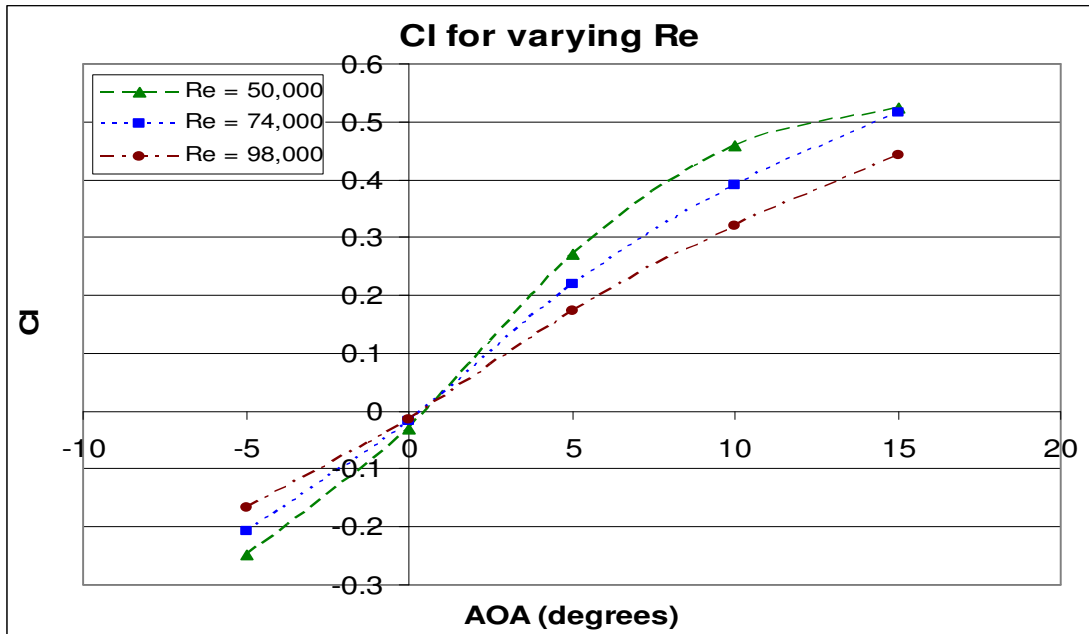
Figure 96. Coefficient of lift for varying Re_c for gliding.

Figure 97 shows the results for the coefficient of drag for the gliding wings. The separated flow over the surface of the wings in the low Reynolds number case, $Re_c = 50,000$, causes the drag coefficient to be higher.
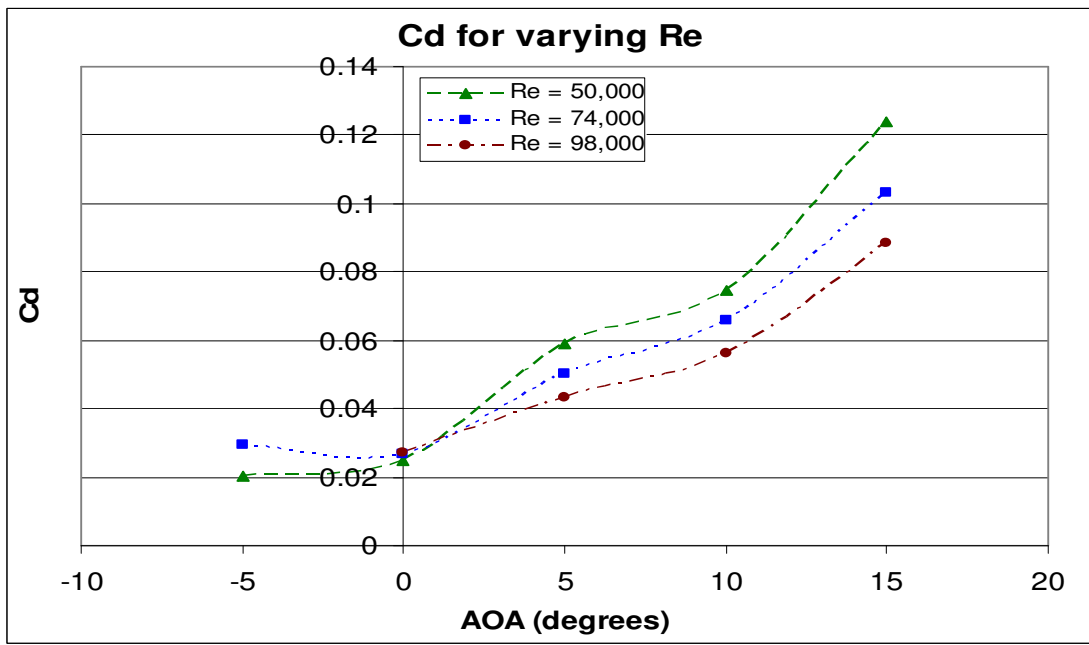
Figure 97. Coefficient of drag for varying Re_c for gliding.

3.4. Conclusion

An experiment designed to explore and elucidate fundamental concepts of a wing flapping configuration have been presented and discussed. The study tested the effects of changing angle of attack, incoming freestream flow velocity, varying wing beat frequency, and examined features of the vehicle in a gliding configuration through force measurements using a 6 DOF JR3 force transducer. The results showed that the lift force could be increased by increasing angle of attack, increasing incoming flow velocity, and increasing wing beat frequency. It is also noted however, that increasing angle of attack and increasing incoming flow velocity decreases the thrust produced by the flapping wing configuration. Only the wing beat frequency can increase both the lift and thrust forces simultaneously. Interestingly these factors hold a different relation with the lift and thrust (or drag) coefficients. It has been shown that although increasing the angle of attack and wing beat frequency increases the coefficient of lift, an increase in incoming freestream flow velocity decreases the lift coefficient. In this study, two flow regimes were found to account for this difference based on the ratio of the wing tip speed to the incoming flow velocity, i.e., the advance ratio. For an advance ratio greater than one, the quasi-steady flow behavior increased the lifting force but was less efficient than the case of unsteady flow behavior with advance ratio less than one; and thus the lift coefficient in the unsteady case was seen to be greater in magnitude than that of the quasi-steady case. In the gliding study, the structural flexure of the wings was shown to decrease the lift and drag coefficients of the wing with increasing chord Reynolds number by changing the effective angle of attack. It was also noted in the gliding study that the flow remained attached to the wings preventing stall as the chord Reynolds number increased.

These preliminary results lay out some of the most basic features of flapping flight and the effects of the tested parameters on the total aerodynamic force loading. This study can help to identify requirements for MAVs with specific design specifications; for instance, knowing the weight of the vehicle a proper wing beat frequency can be prescribed. Clearly flapping flight is a feasible method for both thrust and lift generation for MAVs; now is the time when continued study efforts need to provide understanding of the mechanisms of flapping flight such that they might be exploited to produce the MAV of the future.

Chapter 4. Concluding Remarks

Two experimental studies of non-traditional wing configurations have been studied to gain understanding into their performance in the light of low chord Reynolds flows associated with MAVs. A corrugated dragonfly inspired airfoil was compared with a more traditional smooth airfoil and a flat plate by means of total aerodynamic force measurements and PIV. The results showed that for the Reynolds regime $Re_c < 1.0 \times 10^5$, the corrugated dragonfly airfoil extends the lift curve by delaying stall. The PIV measurements provided insight into this achievement by showing the corrugation peaks acting as boundary layer trips to enhance the energy of the boundary layer before it separates from the airfoil profile. The valleys of the corrugation were found to harbor vortex structures which also help to pull high speed flow to near wall regions of the airfoil, aiding to suppress the airfoil stall. A flapping wing configuration was then studied to examine the effects of angle of attack, incoming flow velocity, and wing beat frequency on the aerodynamic forces. The results showed that to increase lift force, the angle of attack, wing beat frequency, or incoming flow velocity can be increased. However, the result of increasing the angle of attack and/or the incoming flow velocity will have an adverse affect on the thrust produced by the flapping wings. Insight was also gained into the efficiency for the flapping wing configuration by examining the behavior of the lift and thrust coefficients. To increase the efficiency, the advance ratio can be reduced into the unsteady region of flapping flight, i.e., advance ratio less than one. Although there is more work to be conducted in these areas, the author feels comfortable to say that these novel designs could provide great advantages over traditional wings and airfoils in the development and design of new MAVs.

Chapter 5. Recommendations for Future Work

Future work in the study of dragonfly airfoils should be focused to optimize the airfoil design that is most beneficial to a desired chord Reynolds regime. The author suggest to perhaps experiment by making corrugations on the upper surface of the airfoil and a smooth surface on the lower face in an attempt to reduce low angle of attack drag experienced by the current test airfoil. Also of interest in the dragonfly airfoil might be to try a cross section consisting entirely of peak valley structures found at the leading edge of the current test airfoil in order to explore the possibility of trapping more and stronger vortex structures downstream than the current airfoil exhibits.

As mentioned in the introduction of the flapping wing configuration of Chapter 3, the work conducted was only the tip of the iceberg in research for flapping wing topics. With the currently available tools, tests can be conducted to explore wing skin flexibility and tension. In the future, the development of wing joints, and active control of the joints as well as wing skin tension, will become key research points for MAV flapping wing configuration development. Aside from the hardware development of flapping wings, studies of quantitative flow field data for the flow around the flapping wings should be investigated to elucidate the underlying physics of the flow field.

References

[1]   Grant, R.G., "Flight 100 Years of Aviation," DK Publishing, Inc., New York, 2002.

[2]   Lazos, B.S., "Biologically Inspired Fixed-Wing Configuration Studies," *Journal of Aircraft*, Vol. 42, No.5, September-October 2005.

[3]   Chiappe, L.M., "The First 85 Million Years of Avian Evolution," *Nature*, Vol. 378, pp. 349-355, 23 Nov, 1995.

[4]   Olson, S.L., "The Fossil Record of Birds," *Avian Biology*, edited by D. Farner and J. King, Vol. 3, pp. 80-217, 1985.

[5]   McLendon, W.R., "Investigation into Dragonfly Wing Structure and Composite Fabrication," http://tiims.tamu.edu/2005summerREU/papers/McLendon.pdf.

[6]   Wakeling, J.M. and Ellington, C.P., "Dragonfly Flight I. Gliding Flight and Steady-State Aerodynamic Forces," *The Journal of Experimental Biology*, Vol. 200, pp. 543-556, 1997.

[7]   Rees, C.J.C., "Aerodynamic Properties of an Insect Wing Section and a Smooth Aerofoil Compared," *Nature*, Vol. 258, 13, pp. 141-142, Nov. 1975.

[8]   Newman, B.G., Savage, S.B., and Schouella, D., "Model Test on a Wing Section of an *Aeschna* Dragonfly," *Scale Effects in Animal Locomotion*, Edited by T.J. Pedley, London Academic Press, pp. 445-477, 1977.

[9]   Vargas, A. and Mittal, R., "Aerodynamic Performance of Biological Airfoils," AIAA 2004-2319, 2nd Flow Control Conference, Portland, Oregon, 2004.

[10]   Kwokand, M. and Mittal, R., "Experimental Investigation of the Aerodynamics of a Modeled Dragonfly Wing Section," AIAA region I-MA Student Conference, Charlottesville, Virginia, April 8-9, 2005.

[11]   Kesel, A.B., "Aerodynamic Characteristics of Dragonfly Wing Sections Compared with Technical Aerofoil," *Journal of Experimental Biology*, Vol. 203, pp. 3125-3135, 2000.

[12]   Tamai, M., "Experimental investigations on biologically inspired airfoils for MAV applications," Thesis, Iowa State University, 2007.

[13]   Rees, C.J.C., "Form and function in corrugated insect wings," *Nature*, Vol. 256, pp. 200-203, 1975

[14]   Okamoto, M., Yasuda, K., and Azuma, A., "Aerodynamic Characteristics of the
          Wings and Body of a Dragonfly," *Journal of Experimental Biology*, Vol.
          199, pp. 281-294, 1996.

[15]   Hamamoto, M., Ohta, Y., Hara, K., and Hisada, T., "Design of Flexible Wing for
          Flapping Flight by Fluid-Structure Interaction Analysis," 2005 IEEE,
          International Conference on Robotics and Automation, Barcelona, Spain,
          April 2005.

[16]   Kim, D.K., Kim, H.I., Han, J.H., and Kwon, K.J., "Experimental Investigation on
          the Aerodynamic Characteristics of a Bio-mimetic Flapping Wing with
          Macro-fiber Composites," *Journal of Intelligent Material Systems and
          Structures*, DOI: 10.1177/1045389X07083618, 2007.

[17]   Ho, S., Nassefa, H., Pornsinsirirakb, N., Taib, Y.C., and Ho, C.M., "Unsteady
          aerodynamics and flow control for flapping wing flyers," *Progress in
          Aerospace Sciences*,   Vol. 39, pp. 635–681, 2003.

[18]   Shyy, W., Lian, Y., Tang, J., Liu, H., Trizila, P., Stanford, B., Bernal, L., Cesnik,
          C., Friedmann, P., and Ifju, P., "Computational Aerodynamics of Low
          Reynolds Number Plunging, Pitching and Flexible Wings for MAV
          Applications," AIAA 2008-523, 46th Aerospace Sciences Meeting and
          Exhibit, Reno, Nevada, 2008.

[19]   Pederzani, J., and Haj-Harir, H., "Numerical Analysis of Heaving Flexible
          Airfoilsin a Viscous Flow," *AIAA Journal*, Vol. 44, No. 11, November
          2006.

[20]   Ifju, P.G., Jenkins, D.A., Ettinger, S., Lian, Y., Shyy, W., and Waszak, M.R.,
          "Flexible-Wing-Based Micro Air Vehicles," AIAA 2002-0705, 2002.

[21]   Tang, J., Viieru, D., and Shyy, W., "Effects of Reynolds Number and Flapping
          Kinematics on Hovering Aerodynamics," AIAA 2007-129, 45th
          Aerospace Sciences Meeting and Exhibit, Reno, Nevada, 2007.

[22]   Tsuyuki, K., Sudo, S., and Tani, J., "Morphology of Insect Wings and Airflow
          Produced by Flapping Insects," *Journal of Intelligent Material Systems
          and Structures*,DOI: 10.1177/1045389X06055767, 2006.

[23]   Isaac, K.M., Colozza, A., and Rolwes, J., "Force Measurements on a Flapping and
          Pitching Wing at Low Reynolds Numbers," AIAA 2006-450, 44th
          Aerospace Sciences Meeting and Exhibit, Reno, Nevada, 2006.

[24]   Mateescu, D., and Neculita, S., "Low Frequency Oscillations of Thin
          Airfoils in Subsonic Compressible Flows," AIAA 2006-243, 44th
          Aerospace Sciences Meeting and Exhibit, Reno, Nevada, 2006.

[25]   Jiménez, J.M., Buchholz, J.H.J., Staples, A.E., Allen, J.J., and Smits, A.J.,
        "Flapping Membranes for Thrust Production,"
        http://mechanical.rutgers.edu/iutam/m6.pdf.